

# **Extension of a Modular Particle-Continuum Method for Nonequilibrium, Hypersonic Flows**

by

Timothy R. Deschenes

A dissertation submitted in partial fulfillment  
of the requirements for the degree of  
Doctor of Philosophy  
(Aerospace Engineering)  
in The University of Michigan  
2011

Doctoral Committee:

Professor Iain D. Boyd, Chair  
Professor Kenneth G. Powell  
Research Professor Michael R. Combi  
Assistant Professor Thomas E. Schwartzenruber, University of Minnesota

*There are places I remember  
All my life, though some have changed  
    Some forever not for better  
    Some have gone and some remain  
    All these places have their moments  
With lovers and friends, I still can recall  
    Some are dead and some are living  
    In my life, I've loved them all*

Lennon–McCartney, 1965

*Swing and a ground ball, stabbed by Foulke.  
He has it. He underhands to first,  
and the Boston Red Sox are the world champions!  
    For the first time in 86 years,  
the Red Sox have won baseball's world championship!  
    Can YOU believe it?*

Castiglione, 2004

© Timothy R. Deschenes 2011  
All Rights Reserved

This work is dedicated,  
in its entirety,  
to Emily

## ACKNOWLEDGEMENTS

The work contained in this document (and even the work that didn't get included in here) is a result of many years of hard work and study of not only me, but many others that have helped me along the way. Unfortunately I will miss some in this acknowledgment section. If I missed you, sorry about that. Just come find me and I will try to make it up to you, somehow.

First, I would like to thank my advisor, Professor Iain Boyd. On countless occasions, I have told myself how lucky I was to choose you as an advisor and boss. You have always been there to talk about ideas or answer any question that I may have and provide feedback throughout my entire graduate school experience. I also really appreciate you being reasonable on document generation choices even when it is obvious you would prefer not to have to deal with L<sup>A</sup>T<sub>E</sub>X. I also appreciate you having to deal with my horrible grammar and my forgetfulness of running spell check.

I thank Professor Ken Powell, Professor Mike Combi, and Professor Tom Schwartzen-truber for making time to serve on my committee and provide helpful feedback on my graduate research over the past few years. A special thanks goes out to Tom for helping me with the hybrid code (even after he left!). I also thank him for being such a great student that "that's what Tom did" is a good justification for many things that I have done. I would also like to thank David Hash and Michael Wright of NASA Ames Research Center and Eswar Josyula of AFRL Air Vehicles Directorate

for helpful comments on research from the eyes of funding agencies. I would also like to thank the entire aerospace staff and especially our graduate coordinator, Denise Phelps. Not only can she solve any logistical issue that a graduate student faces, but she lets us know about free food (including venison!).

I also thank the current and past members of the Nonequilibrium Gas and Plasma Dynamics Laboratory. It was great to be part of a lab where there was always someone excited to help answer my questions and has evolved in lasting friendships with many of you that transcends just work. I also thank all of my friends in the aerospace department. I will miss walks to Pierpont and “aerosocial” (or “aerodrunks” for the cooler people) events.

There are a few other people that I would like to give a special thanks to. Thanks to Jon Burt for always being excited (and able!) to answer my question about DSMC without a blink. Thanks to Alexandre Martin for helping me with any question about LeMANS, L<sup>A</sup>T<sub>E</sub>X, svn, or anything else. Thanks also for teaching me the rule of assuming Leo is right even when you think he’s wrong. A big thanks to Erin Farbar for taking part in many conversations (and as she categorizes some, arguments) about hypersonic flows, DSMC, and Canada. A big thanks to Tim “classic” Holman for answering questions, talking about sports, and staying classy. I also thank Hicham for always being there to bounce ideas off of and to answer my grid generation questions and Ashley for being the second person to read this dissertation and to share her grammar skills.

I also especially thank my office mates of the past (Tom and Andy) and present (Matt and Marco) for helping me when I had a quick question about pretty much anything. I’m sorry you had to deal with someone with such a cluttered desk and me interrupting you to show you something cool.

Family has always played a big part of my life. Even when I'm busy, I appreciated talking (and talking and talking) to my Mom and P  p  re on the phone. Thank you all for stressing eduction as the number one priority. Thanks to all that have been able to come visit us in Michigan, especially Crystal, Nicole, Gordon, and Jay!

Most importantly, I want to thank my wife, Emily. She has always been there when I have needed her and provides wisdom at the most important times like when she said "she's perfect" while we walked Mollie for the FIRST time at the Humane Society. She has had to work just as hard as I have, including getting people to understand what I actually do, over the past five years AND has to deal with me every night! Having such a great wife to remind me that there's more than engineering, science, and computers, while still giving me time to do work is the best.

## TABLE OF CONTENTS

<b>DEDICATION</b> . . . . .	ii
<b>ACKNOWLEDGEMENTS</b> . . . . .	iii
<b>LIST OF FIGURES</b> . . . . .	ix
<b>LIST OF TABLES</b> . . . . .	xiv
<b>LIST OF APPENDICES</b> . . . . .	xv
<b>LIST OF NOMENCLATURE</b> . . . . .	xvi
<b>CHAPTER</b>	
<b>I. Introduction</b> . . . . .	1
1.1 Motivation . . . . .	2
1.2 Hypersonic Nonequilibrium Flows . . . . .	7
1.2.1 Translational Nonequilibrium . . . . .	9
1.2.2 Internal Energy and Chemical Nonequilibrium . . . . .	10
1.3 Scope of Dissertation . . . . .	12
1.3.1 Dissertation Outline . . . . .	13
<b>II. Mathematical and Numerical Modeling of Dilute Gases</b> . . . . .	16
2.1 Kinetic Description . . . . .	16
2.1.1 Boltzmann Equation . . . . .	17
2.1.2 Simplified Collision Integrals . . . . .	19
2.2 Continuum Description . . . . .	20
2.2.1 Moments of the Boltzmann Equation . . . . .	20
2.2.2 Chapman-Enskog Expansion and Navier-Stokes Equations . . . . .	21
2.2.3 Higher Moment Equations . . . . .	26
2.3 Numerical Methods . . . . .	27
2.3.1 Deterministic Numerical Methods of Rarefied Flows	27
2.3.2 The Direct Simulation Monte Carlo Method . . . . .	28
2.3.3 Computational Fluid Dynamics . . . . .	30

2.3.4	Hybrid Numerical Methods for Partially-Rarefied Flow	31
<b>III.</b>	<b>A Modular Particle-Continuum Method</b>	41
3.1	Flow Modules	42
3.1.1	DSMC Module	42
3.1.2	CFD Module	42
3.2	Overview of Existing Modular Particle-Continuum Method	43
3.2.1	Interface Location and Continuum Breakdown	43
3.2.2	Mesh Refinement	52
3.2.3	Information Transfer	57
3.2.4	Hybrid Data and Algorithm Structure	62
3.3	Extension of a Modular Particle-Continuum Method	66
3.3.1	Rotational Nonequilibrium	66
3.3.2	Vibrational Nonequilibrium	67
3.3.3	Parallelization	68
3.4	Summary	69
<b>IV.</b>	<b>Effects of Rotational Energy Nonequilibrium</b>	70
4.1	Extension of Physical Models	71
4.1.1	Extension of the Boltzmann Equation	71
4.1.2	Rotational Relaxation in DSMC Methods	73
4.1.3	Rotational Relaxation in Continuum Methods	75
4.1.4	Comparison of Rotational Relaxation Models	77
4.2	Modifications to the MPC Method	78
4.2.1	Continuum Breakdown and Interface Location	78
4.2.2	Information Transfer	85
4.3	Verification and Validation of the MPC Method	85
4.3.1	Flows Over a 2D Cylinder	86
4.3.2	Flow Over an Axi-Symmetric Planetary-Probe	100
4.4	Summary and Conclusions from Effects of Rotational Energy Nonequilibrium	108
<b>V.</b>	<b>Effects of Vibrational Energy Nonequilibrium</b>	111
5.1	Extension of Physical Models	112
5.1.1	Extension of the Boltzmann Equation	112
5.1.2	Vibrational Relaxation in the DSMC Method	114
5.1.3	Vibrational Relaxation in Continuum Methods	117
5.1.4	Comparison of Vibrational Relaxation Models	120
5.2	Modifications to the MPC Method	121
5.2.1	Continuum Breakdown and Interface Location	121
5.2.2	Information Transfer	122

5.3	Verification of the MPC Method . . . . .	128
5.3.1	Flow Over a 2D Cylinder . . . . .	129
5.4	Summary and Conclusions from Effects of Vibrational Nonequilibrium . . . . .	140
<b>VI. Extension of Computational Capabilities</b>	. . . . .	143
6.1	Modifications to the MPC Method . . . . .	144
6.2	Verification . . . . .	157
6.3	Parallel Performance . . . . .	157
6.4	Three-Dimensional Implementation . . . . .	165
6.5	Summary and Conclusions from Extension of Computational Capabilities . . . . .	166
<b>VII. Conclusion</b>	. . . . .	168
7.1	Summary . . . . .	168
7.2	Contributions . . . . .	173
7.3	Future Work . . . . .	176
7.3.1	Extension for Simulation of Three-Dimensional Flows	177
7.3.2	Chemistry . . . . .	177
7.3.3	Mesh Type and Refinement . . . . .	178
7.3.4	Continuum Breakdown Parameter . . . . .	179
7.3.5	Investigation of Rarefied Effects in Near-Equilibrium Hypersonic Flows . . . . .	179
<b>APPENDICES</b>	. . . . .	181
<b>BIBLIOGRAPHY</b>	. . . . .	188

## LIST OF FIGURES

### Figure

1.1	Comparison of typical skip and direct entry trajectories for lunar return [1] . . . . .	4
1.2	Variation of Knudsen number throughout the Earth's atmosphere for Orion and Apollo capsules . . . . .	4
1.3	Heat transfer predictions made by macroscopic methods (CFD) on the after-body of the AS-202 flight capsule with experimental flight data [2] . . . . .	6
1.4	Reconstruction of the AS-202 flight trajectory [2] . . . . .	6
1.5	Hypersonic flow over a blunt body . . . . .	11
2.1	Schematic of typical hybrid coupling procedures . . . . .	35
3.1	Degree of breakdown of collisional equilibrium predicted using $Kn_{GL-MAX}$ based on the CFD and DSMC simulation results for Mach 12 flow over a cylinder with a global Knudsen of 0.01 . . . . .	47
3.2	Degree of breakdown of collisional equilibrium predicted using $Kn_{GL-MAX}$ based on the CFD and DSMC simulation results for Mach 12 flow over a cylinder with a global Knudsen of 0.002 . . . . .	48
3.3	Degree of breakdown of collisional equilibrium, using $Kn_{GL-MAX}$ , and heat transfer to the surface predicted by DSMC and CFD methods for flow over a sphere with a free stream Mach number of 10 and a global Knudsen number of 0.01 [3] . . . . .	48
3.4	Degree of breakdown of collisional equilibrium, using $Kn_{GL-MAX}$ , and heat transfer to the surface predicted by DSMC and CFD methods for flow over a sphere with a free stream Mach number of 10 and a global Knudsen number of 0.002 [3] . . . . .	49

3.5	Final interface location and breakdown parameter, as defined by Eq. 3.8, for Mach 12 flow over a cylinder with a global Knudsen number of 0.01. . . . .	51
3.6	Variation of mean free path for Mach 12. flow over a cylinder with a global Knudsen number of 0.002. . . . .	53
3.7	Comparison of DSMC and CFD mesh densities in the shock layer for Mach 12. flow over a two-dimensional cylinder with a global Knudsen number of 0.002 . . . . .	54
3.8	Schematic of mesh refinement calculation on continuum cell [4] . . . . .	55
3.9	Schematic of the refinement limiter as a function of the local breakdown parameter . . . . .	56
3.10	Hybrid particle-continuum coupling procedure [4] . . . . .	58
3.11	Organization of the data structures used by the flow modules and MPC method [4] . . . . .	63
3.12	Schematic of CFD and DSMC meshes with overlap regions around a nonequilibrium shock . . . . .	65
4.1	Comparison of an adiabatic rotational-translational relaxation process predicted by DSMC and CFD . . . . .	78
4.2	Comparison of translational temperatures predicted by the MPC method with (top) and without (bottom) the rotational nonequilibrium breakdown parameter compared with full DSMC computation of Mach 12 flow over a cylinder with a global Knudsen number of 0.01 . . . . .	81
4.3	Comparison of probability density functions predicted by DSMC and equilibrium theory at point <b>A</b> shown in Figure 4.2. . . . .	82
4.4	Comparison of probability density functions predicted by DSMC and equilibrium theory at point <b>B</b> shown in Figure 4.2. . . . .	84
4.5	Comparison of the final continuum-rarefied interface locations for Mach 12 flow over a cylinder at global Knudsen numbers of 0.002 and 0.01. . . . .	87
4.6	Comparison of translational temperature contours predicted by DSMC, CFD, and the MPC method for case <b>CM12K01</b> . . . . .	88

4.7	Comparison of rotational temperature contours predicted by DSMC, CFD, and the MPC method for case <b>CM12K01</b> . . . . .	89
4.8	Comparison of translational temperature contours predicted by DSMC, CFD, and the MPC for case <b>CM12K002</b> . . . . .	91
4.9	Comparison of rotational temperature contours predicted by DSMC, CFD, and the MPC for case <b>CM12K002</b> . . . . .	92
4.10	Comparison of temperatures and density along a 45° extraction line for case <b>CM12K01</b> . . . . .	92
4.11	Comparison of temperatures and density along a 135° extraction line for case <b>CM12K01</b> . . . . .	93
4.12	Comparison of temperatures and density along a 45° extraction line for case <b>CM12K002</b> . . . . .	93
4.13	Comparison of temperatures and density along a 135° extraction line for case <b>CM12K002</b> . . . . .	94
4.14	Comparison of surface quantities about the cylinder predicted by DSMC, CFD, and the MPC method for case <b>CM12K01</b> . . . . .	95
4.15	Comparison of surface quantities about the cylinder predicted by DSMC, CFD, and the MPC method for case <b>CM12K01</b> . . . . .	96
4.16	Comparison of surface quantities about the cylinder predicted by DSMC, CFD, and the MPC method for case <b>CM12K002</b> . . . . .	96
4.17	Comparison of surface quantities about the cylinder predicted by DSMC, CFD, and the MPC method for case <b>CM12K002</b> . . . . .	97
4.18	Interface location and variation of mean free path for Mach 20 flow around a sting-mounted, planetary probe with a global Knudsen number of 0.01 . . . . .	101
4.19	Comparison of translational temperature by DSMC, CFD, and the MPC method . . . . .	102
4.20	Comparison of translational temperature by DSMC, CFD, and the MPC method . . . . .	102

4.21	Temperature and density predicted by DSMC, CFD, MPC (Rot. Neq.), and the MPC method (Rot. Eq.) along C1 . . . . .	103
4.22	Temperature and density predicted by DSMC, CFD, MPC (Rot. Neq.), and the MPC method (Rot. Eq.) along C2 . . . . .	104
4.23	Comparison of velocity distribution functions predicted by DSMC, CFD, and the MPC method within the bow shock . . . . .	105
4.24	Comparison of rotational energy distribution functions predicted by DSMC, CFD, and the MPC method within the bow shock . . . . .	106
4.25	Surface heat transfer along planetary probe . . . . .	107
5.1	Comparison of adiabatic vibrational-translational relaxation process predicted by DSMC and CFD . . . . .	121
5.2	Probability of a particle with any vibrationally excited state as a function of macroscopic vibrational temperature . . . . .	123
5.3	Comparison of the level of statistical scatter of subrelaxation averages of internal temperatures at various levels . . . . .	127
5.4	Vibrational temperature as a function of specific vibrational energy	128
5.5	Comparison of initial and final rarefied-continuum interface locations used by the MPC method for the <b>CM15K01<sub>CB</sub></b> case . . . . .	130
5.6	Comparison of temperature contours predicted by full DSMC, full CFD, and the MPC method for the <b>CM15K01<sub>VP</sub></b> case . . . . .	131
5.7	Comparison of temperature contours predicted by full DSMC, full CFD, and the MPC method for the <b>CM15K01<sub>VP</sub></b> case . . . . .	132
5.8	Comparison of temperature contours predicted by full DSMC, full CFD, and the MPC method for the <b>CM15K01<sub>CB</sub></b> case . . . . .	133
5.9	Comparison of temperature contours predicted by the DSMC, the CFD, and the MPC method for the <b>CM15K01<sub>CB</sub></b> case . . . . .	133
5.10	Comparison of temperatures predictions by full DSMC, full CFD, and the MPC method along the 45° extraction line for the <b>CM15K01<sub>VP</sub></b> and <b>CM15K01<sub>CB</sub></b> cases. . . . .	134

5.11	Comparison of vibrational temperature predicted by full DSMC, full CFD, and the MPC method along the 135° extraction line using different vibration-translation relaxation models in the DSMC method	136
5.12	Comparison of heat transfer to the cylinder surface predicted by full DSMC, full CFD, and the MPC method for the <b>CM15K01<sub>VP</sub></b> case.	137
5.13	Comparison heat transfer to the cylinder surface predicted by full DSMC, full CFD, and the MPC method for the <b>CM15K01<sub>CB</sub></b> case.	138
6.1	Schematic of cell load estimation supplied to METIS depending on the proceeding module call . . . . .	153
6.2	Temperature contours and processor domain boundaries for a DSMC module call during steady state . . . . .	158
6.3	Normalized number of DSMC particles per processor for parallel implementation of the MPC method on 16 processors . . . . .	159
6.4	Parallel speedup (fixed problem size) . . . . .	160
6.5	Scaled efficiency of the MPC method (problem size scaled with number of processors) . . . . .	163
6.6	Parallel speedup and scaled efficiency of the MPC method when applied to a problem with comparable computational cost of a three-dimensional simulation . . . . .	165
A.1	Variation in vibrational relaxation time for N <sub>2</sub> . . . . .	184
B.1	Example of the variable bin width histogram technique to construct a rotational energy probability density function from data sampled in the shock interior from the DSMC method . . . . .	187

## LIST OF TABLES

### Table

4.1	Computational performance and memory requirements for the MPC method . . . . .	98
4.2	Computational performance and memory requirements for the MPC method. . . . .	107
5.1	Computational performance and memory requirements for the MPC method. . . . .	140
A.1	Species data for VHS collision model . . . . .	182
A.2	Species data for rotational relaxation model . . . . .	183
A.3	Species data for vibrational relaxation models . . . . .	183

## LIST OF APPENDICES

### Appendix

A.	Species Data . . . . .	182
A.1	Variable Hard Sphere Coefficients . . . . .	182
A.2	Rotational Relaxation Coefficients . . . . .	182
A.3	Vibrational Relaxation Coefficients . . . . .	183
B.	Estimation of a Probability Density Function . . . . .	185

## LIST OF NOMENCLATURE

### Constants

$k$	Boltzmann Constant [ $1.38 \times 10^{-23}$ J/K]
$N_A$	Avogadro's Number [ $6.022 \times 10^{26}$ mol $^{-1}$ ]
$R$	Universal Gas Constant [8.314 J/K·mol]

### Acronyms

<b>AMAR</b>	Adaptive Mesh Algorithm Refinement
<b>ADV</b>	Adaptive Discrete Velocity
<b>CFD</b>	Computational Fluid Dynamics
<b>DSMC</b>	direct simulation Monte Carlo
<b>IP</b>	Information Preservation
<b>LD</b>	Low Diffusion
<b>MPC</b>	Modular Particle-Continuum
<b>VHS</b>	Variable Hard Sphere
<b>UFS</b>	Unified Flow Solver

### Latin Symbols

$Br$	Breakdown Parameter
$\bar{c}$	Mean Speed [m/s]
$\mathbf{c}$	Particle Velocity Vector $\mathbf{c}(c_x, c_y, c_z)$ [m/s]
$\mathbf{C}$	Thermal Velocity Vector $\mathbf{C}(C_x, C_y, C_z)$ [m/s]
$c_{v,p}$	Specific Heat [J/kg·s]
$C_p$	Pressure Coefficient
$C_\tau$	Shear Coefficient
$C_q$	Heat Flux Coefficient
$Da$	Dahmköhler
$d$	Molecular Diameter [m]
$E$	Energy per Unit Volume [J/m <sup>3</sup> ]
$\mathbf{E}$	x-direction Flux Vector
$e$	Specific Energy per Unit Volume [J/m <sup>3</sup> kg]
$F$	Refinement Factor

<b>F</b>	External force vector [N], y-direction Flux Vector
$f$	Velocity Distribution Function $f(\mathbf{x}, \mathbf{C}, t)$
$f_{\text{MB}}$	Maxwellian (or equilibrium) Velocity Distribution Function
$f_G$	Anisotropic Gaussian Distribution Function
<b>G</b>	z-direction Flux Vector
<b>g</b>	Relative Velocity Vector [ $\text{m}/\text{s}$ ]
$h$	Enthalpy [ $\text{J}/\text{kg}$ ]
$Kn$	Knudsen Number
$l_f$	Length of Face
$L$	Characteristic Length [m]
$m$	Mass [kg]
$M$	Mach Number, Molecular Mass [ $\text{kg}/\text{kmol}$ ]
$N_x$	Number of quantity $x$
$N_F$	Number of Faces
$\hat{n}_f$	Face Unit Normal
$n$	Number Density [ $\text{m}^{-3}$ ]
$V$	Volume [ $\text{m}^3$ ]
<b>V</b>	Bulk (Average) Velocity Vector $\mathbf{V}(u, v, w)$ [ $\text{m}/\text{s}$ ]
<b>U</b>	Conserved Variable Vector
<b>q</b>	Heat Transfer Rate $\mathbf{q}(q_x, q_y, q_z)$ [ $\text{W}/\text{m}^2$ ]
$Q$	Macroscopic Quantity
$p$	Pressure [Pa]
$\langle P \rangle$	Average Probability
$r_f$	Cell Refinement Factor
$R_{\text{gas}}$	Specific Gas Constant [ $\text{J}/\text{K}\cdot\text{kg}$ ]
$s$	Distance Along Surface, Number of Samples, Standard Deviation
$S$	Source Term Vector
$S_{np}$	Parallel Speedup
$t$	Time [s]
$T$	Temperature [K]
$T_s$	Wall Time for Serial Computation
$T_{np}$	Wall Time for Parallel Computation on $np$ processors
$V$	Volume [ $\text{m}^3$ ]
$W$	Numerical Particle Weight
$\mathbf{x}$	Physical Position $\mathbf{x}(x, y, z)$ [m]
X	Mole Fraction
Y	Mass Fraction
Z	Collision Number

## Greek Symbols

$\gamma$	Ratio of Specific Heats
$\Gamma$	Chapman-Enskog Expansion, Gamma Function
$\epsilon$	Particle energy [J]

$\varepsilon$	Energy per unit volum [ $J/m^3$ ]
$\zeta$	Number of Degrees of Freedom
$\eta_s$	Scaled (Weak) Parallel Efficiency
$\theta$	Characteristic Temperature
$\kappa$	Thermal Conductivity [ $W/m \cdot K$ ]
$\lambda$	Mean Free Path [m]
$\mu$	Viscosity [ $Pa \cdot s$ ], Reduced mass [kg]
$\nu$	Mean Collision Rate [ $1/s$ ], BGK Characteristic Relaxation Time [s]
$\xi$	Chapman-Enskog Parameter
$\rho$	Density [ $kg/m^3$ ]
$\sigma$	Collision Cross Section [ $m^2$ ]
$\tau_{i,j}$	Shear Stress Tensor[Pa]
$\tau$	Characteristic Time [s]
$\phi$	Instantaneous Probability
$\varphi$	Perturbation Coefficient
$\Phi$	Subrelaxation Parameter
$\omega$	VHS Temperature Exponent
$\dot{\omega}$	Navier-Stokes Source Terms
$\Omega$	Solid Angle [sr]

## Subscripts

$(.)_{BGK}$	Bhatnagar-Gross-Krook
$(.)_{cc}$	Continuum Cell
$(.)_{CHAR}$	Characteristic
$(.)_{CHEM}$	Chemical
$(.)_{COL}$	Collision
$(.)_{cutoff}$	Cutoff Value
$(.)_{EL}$	Electronic
$(.)_{FLUID}$	Fluid
$(.)_{GL}$	Gradient-Length
$(.)_{L-T}$	Landaу-Teller
$(.)_{MAX}$	Maximum
$(.)_{MW}$	Millikan and White
$(.)_{P_{rc}}$	Particles in Rarefied Cell
$(.)_{Park}$	Park
$(.)_s$	Species
$(.)_{Real}$	Real
$(.)_{rc}$	Rarefied Cell
$(.)_{ROT}$	Rotation
$(.)_{ROT-NEQ}$	Rotation Nonequilibrium
$(.)_{ref}$	Reference Value
$(.)_{TRA}$	Translation
$(.)_{VIB}$	Vibration

$(.)_w$	Wall Value
$(.)_\infty$	Free Stream
$(.)_0$	Stagnation

## CHAPTER I

### Introduction

The objective of this dissertation is to improve the tools available to simulate hypersonic, nonequilibrium flows by increasing the physical accuracy and computational capabilities of a multi-scale, numerical method. Accurate prediction of these hypersonic flows must include models that describe important physical phenomena, some of which are microscopic in nature. Ideally, all processes are entirely described with a microscopic description. However, due to the large discrepancies in characteristic time- and length-scales, this would make even the simplest flow prediction unnecessarily computationally intensive. To increase the computational efficiency, it is required to describe each flow phenomenon using the simplest possible model, which typically occurs at the largest possible time- and length-scales, while still maintaining the required physical accuracy. However, for many flows, the range of scales that occur about the vehicle is large enough that some regions require a microscopic description of the flow, while a macroscopic description is sufficiently accurate enough for the rest of the flow field.

This is the case over a significant portion of a hypersonic vehicle's flight trajectory, where most of the flow can be considered continuum and a macroscopic description is valid, but some localized regions require a microscopic description. In addition,

description of the important physical processes such as rotational and vibrational excitation must be modeled across the entire flow field regardless of the flow description. Furthermore, the numerical method must run efficiently on parallel computers to solve very large problems with a high level of numerical accuracy over arbitrary three-dimensional bodies. This dissertation expands a multi-scale method to extend its capabilities by increasing the physical accuracy and computational capabilities to simulate the aerothermodynamic nature of flow over hypersonic vehicles.

## 1.1 Motivation

Development of new hypersonic flight vehicles is a current topic of interest for scientific, military, and commercial applications. As the aged Space Shuttle program nears retirement, significant research and development towards new spacecraft are being performed to ensure reliable and cost-effective means to ferry cargo and humans to space and back. These new vehicles will leverage technological advancements to increase safety and reliability standards over the previous generation of vehicles.

The design of hypersonic vehicles requires accurate prediction of near field and surface properties, such as heat flux, shear stress, and pressure, along the entire vehicle surface and throughout all possible flight trajectories. These quantities determine both the aerodynamic performance of each vehicle which is necessary for guidance, navigation, and control, and the thermodynamic performance which determines the type and sizing of the thermal protection system (TPS) that is required to guarantee that the vehicle survives the intense heat transfer from the surrounding flow.

Many of these new mission profiles require accurate and precise land recovery of the vehicle. For example, precise lunar reentry landings during the entire lunar month require downrange capabilities of the vehicle to be at least 10,000 km [1].

Direct entry trajectories can not achieve such large downrange capabilities, but by using a lifting body with a skip trajectory, the downrange requirement is possible. An example of a direct entry and skip trajectory is shown in Fig. 1.1. In contrast to the direct entry trajectory, where the vehicle falls directly to the planet surface, the skip trajectory includes one or more “skips” where the vehicle increases altitude after the initial entry. This has the effect of dissipating more of the energy of the vehicle in the low density, upper atmosphere which decreases the peak heat flux to the vehicle. It also increases the total time spent in the atmosphere, the total heat load to the vehicle, and its downrange capabilities. However, with the use of a skip trajectory, the amount of time spent at high altitude, where the effects of rarefaction and thermochemical nonequilibrium are important, has increased significantly. For example, Fig. 1.2 shows the variation of Knudsen number, which is one measure of the degree of nonequilibrium in the flow that may require a microscopic description and will be described in the proceeding subsection, throughout the atmosphere for Apollo and Orion capsules. Typically, it is accepted that the macroscopic gas dynamics formulation, using the Navier-Stokes equations, is only valid for Knudsen numbers less than  $10^{-2}$ , while portions of the flow may require a microscopic description for Knudsen numbers as low as  $10^{-4}$  [5, 2, 6]. As seen in Fig. 1.1, the change from direct entry to skip trajectory has increased the time spent in the nonequilibrium regime (when the altitude exceeds  $\sim 70$  km) from less than 10% to over 50% of the total trajectory time. This has the effect of increasing the contribution to the total heat load from the nonequilibrium flow regime and requires increased accuracy in the prediction tools for hypersonic flow at these high altitudes to reduce vehicle cost and increase vehicle reliability.

The AS-202 test flight from the Apollo program is one of the few flight tests that

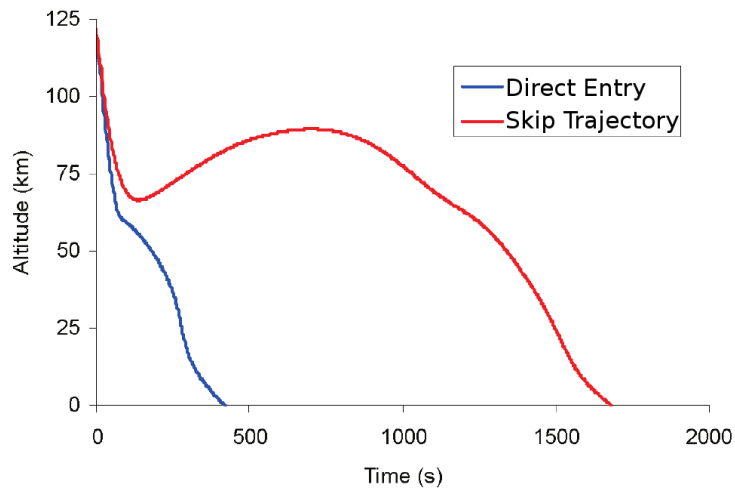


Figure 1.1: Comparison of typical skip and direct entry trajectories for lunar return [1]

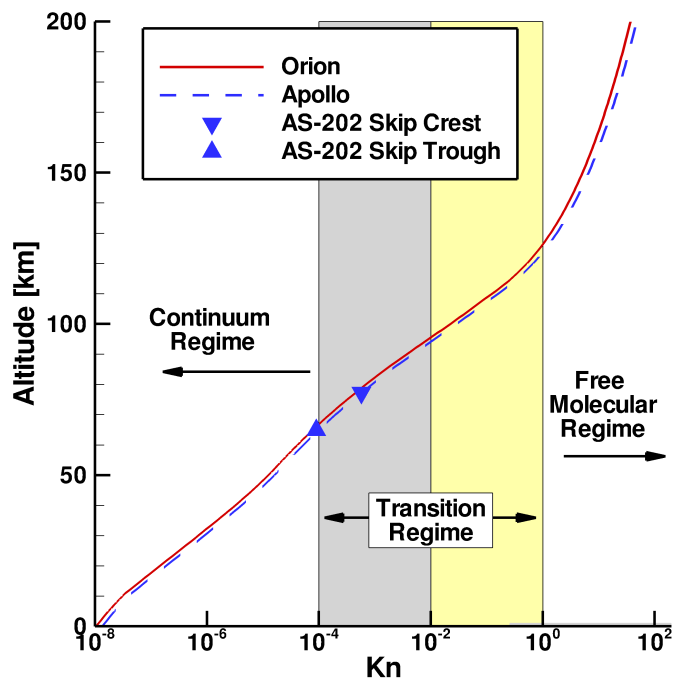


Figure 1.2: Variation of Knudsen number throughout the Earth's atmosphere for Orion and Apollo capsules

used a skip trajectory. Recently, Wright et al. [2] performed detailed simulations of the entire AS-202 flight trajectory using a macroscopic description of the flow. In general, they found that agreement between available experimental heat transfer measurements and current numerical predictions was good over most of the trajectory. However, at the top of the skip portion of the trajectory, the simulation results over-predicted the measured data across most of the lee side of the aft-body. For example, Fig. 1.3 compares heat transfer prediction and flight measurements from a calorimeter located on the top of the lee side. During the skip portion, the CFD simulation method over-predicts the measured data by over a factor of two. Based on the reconstructed data shown in Fig. 1.4 and the corresponding Knudsen number at this altitude shown in Fig. 1.2, it is clear that the vehicle has transitioned from being fully continuum to partially rarefied as it passes from the trough to the crest of the skip portion of the trajectory. Because of this, Wright et al. concluded that the over-prediction of heat transfer may be due to the inability to capture the important microscopic effects in the macroscopic methods used in that work. However, for this particular flow, application of a microscopic method to the entire flow would be computationally expensive. Instead, a multi-scale approach that only uses the expensive, microscopic description in required regions, while using the macroscopic description throughout the rest of the flow field, is more suitable to examine any rarefied flow effects.

Simulation of other multi-scale, hypersonic flows are of particular importance for developing technologies that will enable potential high-mass, Mars missions. Compared to the Earth's atmosphere, Mars' relatively thin atmosphere causes entry vehicles to decelerate at much lower altitudes. Depending on the mass, size, and shape of a vehicle, it may never reach a subsonic terminal velocity. This necessitates ad-

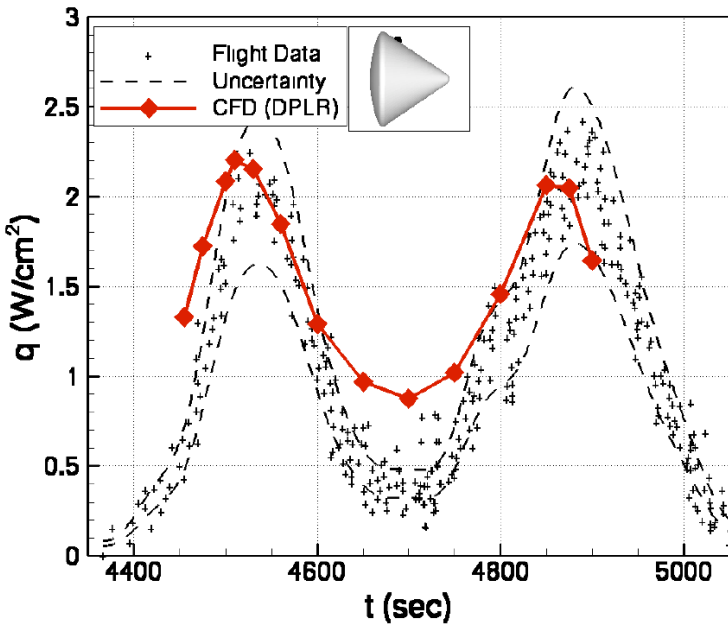


Figure 1.3: Heat transfer predictions made by macroscopic methods (CFD) on the after-body of the AS-202 flight capsule with experimental flight data [2]

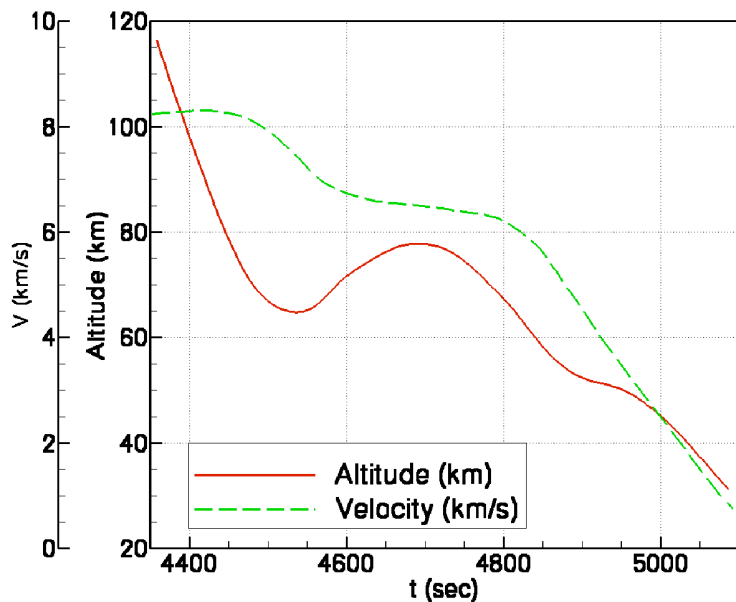


Figure 1.4: Reconstruction of the AS-202 flight trajectory [2]

ditional technology to slow the vehicle so that it can reach subsonic speeds with sufficient time to prepare for landing. Many of these new technologies require successful prediction of multi-scale interaction flows to ensure reliability. In order to increase the frontal area of the vehicle, an inflatable aerodynamic decelerator, often called a ballute, may be used to slow the vehicle down at higher altitudes [7]. The dynamic fluid structure interaction at deployment will most certainly occur in the rarefied regime [8] and will involve a detailed fluid structure interaction requiring accurate prediction of surface properties throughout the entire trajectory. In addition, the flow field around the deployed ballute in the upper atmosphere will include both large regions of continuum flow, due to the very large body, and small nonequilibrium interactions around tethers, connections, and the low density wake which may require a microscopic analysis. Another possible option that will enable high-mass, Mars missions is supersonic retro-propulsion [9], where a jet is expelled out the front of the aeroshell displacing the shock and increasing the total axial force on the vehicle. At high altitudes, these flows may include a very dense, continuum region within the core of the jet, while much of the flow may be rarefied. Multi-scale methods that can accurately simulate these flow fields will be a vital tool in development of these new technologies that enable future scientific and exploration missions [7].

## 1.2 Hypersonic Nonequilibrium Flows

Due to the high free stream enthalpies and abrupt changes in flow quantities, hypersonic flows demonstrate many forms of nonequilibrium processes. The selection of a model description for each these nonequilibrium effects typically depends on two quantities: the characteristic energy,  $\varepsilon_{\text{CHAR}}$ , and the characteristic time scale,  $\tau_{\text{CHAR}}$ .

The characteristic energy of a flow process determines whether the flow phe-

nomenon is sufficiently activated in the flow. The Arrhenius number,  $Ar$ , shown in Eq. 1.1 where  $\varepsilon_{\text{CHAR}}$  and  $\theta_{\text{CHAR}}$  are the characteristic energy and temperature of the process, respectively,  $k$  is the Boltzmann constant, and  $T$  is the temperature, can be used to compare the required activation energy to a measure of the available energy content in the flow.

$$Ar = \frac{\varepsilon_{\text{CHAR}}}{kT} = \frac{\theta_{\text{CHAR}}}{T} \quad (1.1)$$

As  $Ar \rightarrow 0$ , the energy of each particle collision is much higher than the activation energy of the physical process, and the process will occur. In contrast, as  $Ar \rightarrow \infty$  the energy in each particle collision is much smaller than the activation energy, the process is not activated and can be neglected with little loss of physical accuracy.

The characteristic time scale of a flow process determines the time scale needed for the process to return to thermodynamic equilibrium after an abrupt change. The abrupt change may be due to a strong shock, strong expansion, or large heat or momentum transfer. The characteristic time can be compared to a characteristic fluid time-scale,  $\tau_{\text{FLUID}}$ , to construct the Dahmköhler number,  $Da$ , as shown in Eq. 1.2.

$$Da = \frac{\tau_{\text{FLUID}}}{\tau_{\text{CHAR}}} \quad (1.2)$$

As  $Da \rightarrow \infty$ , the physical process can react very quickly compared to the flow transient time, and the process can be considered in equilibrium. If the Dahmköhler number for all physical processes approach infinity, the flow can be considered in local thermodynamic equilibrium everywhere around the hypersonic vehicle. In contrast, as  $Da \rightarrow 0$ , the physical process time scale is much larger than the flow transient time and the process can be considered frozen and remains the same everywhere in the flow field of interest. Often, when the Dahmköhler number is small, the Arrhenius number is also small. For flows with  $Da$  on the order of unity, detailed description of

the nonequilibrium process may be required to achieve sufficient physical accuracy.

### 1.2.1 Translational Nonequilibrium

Translational (or collisional) nonequilibrium occurs in any region of the flow where a gradient exists. For this process, the Arrhenius number is always on the order of unity, such that translational processes are always activated in a gas. The molecular collisions in the gas ultimately change the macroscopic quantities such as velocity, temperature, or chemical composition and push the flow toward local equilibrium. If many collisions occur over a change of macroscopic flow variables, then the degree of collisional nonequilibrium is quite small. However, if very few collisions occur over this change, the translational nonequilibrium can be significant such that the flow is rarefied and must be modeled in a microscopic manner. The characteristic time scale for this process is the mean free time,  $\tau_{\text{COL}}$ , which is the average time between each collision that a particle experiences. Instead of directly using the Dahmköhler number, the Knudsen number, shown in Eq. 1.3, is typically used to determine the degree of collisional nonequilibrium. This parameter is inversely proportional to the product of the Dahmköhler number and the Mach number,  $M$ , which is the ratio of the bulk velocity to the speed of sound. Here,  $\lambda$  is the average distance a gas particle travels between collisions, or mean free path, and  $L$  is a characteristic length scale of a flow feature or a vehicle.

$$Kn = \frac{\lambda}{L} \sim \frac{1}{Da M} \quad (1.3)$$

As  $Kn \rightarrow 0$ , many molecular collisions occur around the vehicle that can maintain local translational equilibrium such that the velocity and energy probability density functions remain very near normal, or Gaussian, throughout the perturbation (due to the vehicle) of the flow. For these flows, a description using mean values and

lower order moments of the velocity and energy distribution functions is acceptable for sufficient physical accuracy. In contrast, as  $Kn \rightarrow \infty$ , the number of collisions that occur around the vehicle is very small, and the gas particles that are perturbed by the presence of the vehicle experience very few collisions such that local equilibrium is not maintained. Now, the distribution functions of particle velocities and energies are very far from normal and description of these flows with only low order moments is insufficient. Instead, a microscopic approach must be employed to describe a rarefied flow, where the collisional nonequilibrium effects are important. The direct simulation Monte Carlo (DSMC) method, that was first developed by Bird [10] and is described in Sec. 2.3.2, is the most popular numerical method for simulating hypersonic, rarefied flows.

### 1.2.2 Internal Energy and Chemical Nonequilibrium

When a vehicle is traveling at a hypersonic speed through the atmosphere, a strong shock is formed over the front of the vehicle and converts much of the free stream kinetic energy to thermal energy. Figure 1.5 shows translational temperature contours in the fore-body region for flow over a typical re-entry capsule. The temperature in the shock layer, which is defined as the flow region between the strong shock and the vehicle surface, has increased to over  $5 \times 10^4$  K. In addition to excitation of rotational energy ( $\theta_{\text{CHAR-ROT}} \sim 10^1$  K and whose Arrhenius number is much less than unity for nearly all gas flows), this high thermal energy content can cause the Arrhenius numbers for vibration excitation ( $\theta_{\text{CHAR-VIB}} \sim 10^3$  K), electronic excitation ( $\theta_{\text{CHAR-EL}} \sim 10^4$  K), and chemical reactions ( $\theta_{\text{CHAR-CHEM}} \sim 10^5$  K) to be on the order of or less than unity.

Since each of these flow processes progress through molecular collisions, the char-

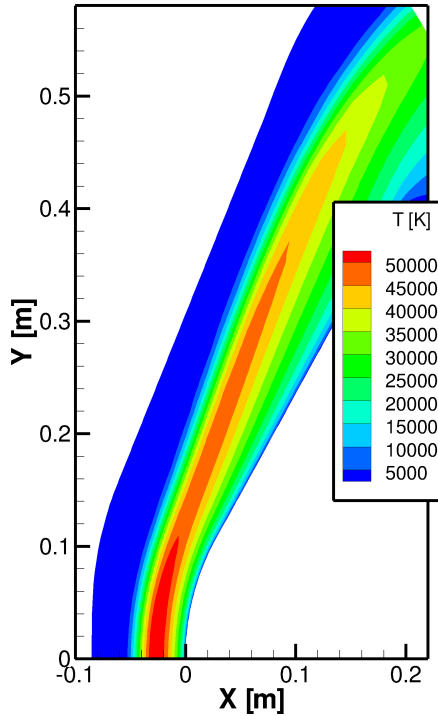


Figure 1.5: Hypersonic flow over a blunt body

acteristic time for each process can be formulated as a multiple of the mean collision time and are typically ordered as shown in Eq. 1.4.

$$\tau_{\text{COL}} \sim \tau_{\text{TRA}} < \tau_{\text{ROT}} \ll \tau_{\text{VIB}} \sim \tau_{\text{EL}} \sim \tau_{\text{CHEM}} \quad (1.4)$$

Therefore in a rarefied flow, that contains translational nonequilibrium, the Dahmköhler number of any activated process may be on the order of or less than unity and these nonequilibrium effects should be considered. For example, the internal energies are in equilibrium with the translational energy mode in the free stream throughout an entry trajectory. After particles pass through the bow shock, the random translational energy of the particle reaches near equilibrium, such that the translational energy distribution function is near normal, after five to ten collisions. However, the rotational energy does not reach equilibrium with the translational energy mode until after an additional ten collisions, while the vibrational energy mode requires

about one thousand collisions. In higher energy flows, electronic energy excitation and chemical reaction processes will relax at about the same time as the vibrational energy mode. All of these will be on the order of or larger than the flow transit time in rarefied flows, so accurate prediction of the evolution of these nonequilibrium processes is vital to achieve sufficient physical accuracy in the simulation methods.

### 1.3 Scope of Dissertation

The purpose of this dissertation is to improve the predictive capabilities of simulation tools applied to hypersonic aerothermodynamic flows that include small regions of flow that are in collisional nonequilibrium. The work performed by Schwartzentruer [11] began this effort by developing a serial implementation of a hybrid particle-continuum method that couples existing microscopic and macroscopic solvers in a modular fashion and applied the method to one- and two-dimensional flows that contained translational nonequilibrium, but accounted for only rotational nonequilibrium in the microscopic solver. The first part of this study extends the previous work by including rotational nonequilibrium modeling capabilities in both flow solvers and outlining the changes required to the hybrid framework that takes into account these added capabilities. Next, this study will outline the extension of the method to include the models required to take into account vibrational nonequilibrium in each module of the hybrid method and any changes required in the hybrid framework. Then, the study outlines the parallelization of the method for distributed memory systems to decrease the processor memory requirements and wall clock time for the simulation of complex flows that require many numerical grid points and simulator particles. The parallelization method described in this dissertation will enable future expansions of the hybrid method to simulate three-dimensional flows.

### 1.3.1 Dissertation Outline

This chapter has introduced the nature of low density, hypersonic flows and shown that a microscopic description may be necessary to maintain the physical accuracy of predictive simulations. Description of these hypersonic flows also requires additional models to take into account various thermochemical nonequilibrium effects. These simulation capabilities are vital to the success of future missions by providing an accurate description of the environment around a hypersonic vehicle.

Chapter II details the various mathematical descriptions available for gas flows, which range from fully kinetic to entirely continuum. These descriptions start with the fundamental Boltzmann equation. Simplification of the flow description is introduced to develop the continuum Navier-Stokes and Euler equations. The validity of each simplifying assumption is discussed. The chapter also describes numerical procedures used for each description of the flow. An outline of the direct simulation Monte Carlo method, which is a particle method that statistically simulates the Boltzmann equation [10], is provided. Particle movement and collision routines are described and numerical limitations of the simulation method are outlined. Finally, an outline of previous hybrid numerical techniques that have been developed to describe mixed continuum and rarefied flows is presented.

Chapter III details the hybrid, Modular Particle-Continuum (MPC) method that is used in this work. First, descriptions of the numerical continuum, LeMANS, and rarefied, MONACO, flow modules are provided. Next, the existing capabilities of the MPC method, which include calculation of the interface location, geometric mesh construction, and the transfer of information between each flow module, are outlined. Then, overviews of each extension of the MPC method are provided, which consist of inclusion of rotational and vibrational nonequilibrium models in each flow

module and parallelization of the numerical method.

Chapter IV provides a detailed description of inclusion of rotational nonequilibrium models in the MPC method. The chapter begins with a summary of the mathematical description of rotational relaxation processes and the implementation of these descriptions in each flow module. Next, an outline of the changes required in the MPC method for inclusion of rotational relaxation is described. Finally, verification and validation of the method are performed through the comparison of predictions made by the MPC method to those made with full DSMC and full CFD simulations and all three predictions are compared to available experimental measurements. Computational performance of the MPC method, compared to full DSMC, is discussed for each simulation.

Chapter V outlines the necessary changes in the MPC method for inclusion of vibrational nonequilibrium models. First, the mathematical description of vibrational relaxation processes is outlined. Then the chapter describes the implementation of vibrational nonequilibrium models in the two flow modules. Next, a detailed description is provided of the required changes to the MPC routines to take into account the transfer of vibrational energy. Finally, verification of the implementation of vibrational nonequilibrium models is performed through comparison with fully kinetic and continuum simulation methods.

Chapter VI outlines the extension of the MPC simulation capabilities to distributed memory systems that are required to simulate three-dimensional and complex two-dimensional flows. First, modifications to the MPC method are outlined and characterization of computational load parameters required for efficient distribution of the numerical domain across processors in a distributed memory system are described. A complete description of the algorithms necessary to parallelize

the MPC method within the provided modular framework are provided. Then, the parallel performance of the MPC method is described and compared with similar simulation techniques. In addition, verification of the implementation of the parallel routines is performed.

Finally, chapter VII summarizes all conclusions drawn from each chapter and highlights the major contributions of this dissertation to the simulation of hypersonic, nonequilibrium gas flows. The chapter concludes with discussion and recommendation of future directions of this topic of research.

## CHAPTER II

# Mathematical and Numerical Modeling of Dilute Gases

This chapter provides details of the basic governing equations that are utilized to simulate gas flows that may require descriptions ranging from entirely kinetic to fully continuum. Starting with the Boltzmann equation, a description of assumptions needed to develop lower order models that are sufficient for near equilibrium flows are outlined. Analytic solutions to the mathematical models are difficult to obtain and often require many assumptions. In contrast, the mathematical models can be solved numerically on current computer architectures. An outline is provided of numerical methods used to solve gas flows of interest that are fully rarefied, fully continuum, or mixed rarefied-continuum.

### 2.1 Kinetic Description

Ideally, given the particular nature of gas dynamics, computer simulation of molecular flows would be entirely deterministic and depend directly on first principle physics. This would require modeling each and every particle and the molecular interactions between them. This can be done using molecular dynamics, but is limited to simulation of a very small number of real particles on the order of tens to hundreds

of thousand. At standard temperature and pressure, a cubic meter of air contains over  $1 \times 10^{25}$  particles which makes a full deterministic simulation with molecular dynamics infeasible for all but the smallest scale or lowest density problems.

### 2.1.1 Boltzmann Equation

Although there are a large number of molecules in a typical volume, for all but very high density gas dynamic flows, the gas can still be considered dilute and collisions can be limited to binary interactions between two molecules. Along with the assumption of molecular chaos, the integro-differential Boltzmann equation, which is shown in Eq. 2.1, is applicable. The Boltzmann equation follows the evolution of the probability density function,  $f(\mathbf{x}, \mathbf{C}, t)$ , through the 6 total combination dimensions of physical and velocity, or phase, space. Here,  $n$  is the number density and  $\mathbf{F}$  is the force vector. For all flows considered in this work, the force field is considered to be zero everywhere in phase space.

$$\frac{\partial}{\partial t} [nf] + c_i \frac{\partial}{\partial x_i} [nf] + \frac{\partial}{\partial c_i} [F_i n f] = \left\{ \frac{\partial}{\partial t} [nf] \right\}_{\text{col}} \quad (2.1)$$

The right hand side of the Boltzmann equation tracks the change of the probability density function due to molecular collisions. Limiting consideration to binary collisions, the collision integral for a monatomic gas can be modeled using the form shown in Eq. 2.2 where  $g$  is the relative velocity between the colliding particles,  $\sigma$  is the collision cross section between the particles,  $f_j$  is the probability density function of the collision partner with  $f$ , and the post collision probability density functions are given by  $f'_j$  and  $f'$ . Using the conservation of momentum, the post collision velocities,  $\mathbf{C}'$  and  $\mathbf{C}'_j$ , can be directly related to the original velocities,  $\mathbf{C}$  and  $\mathbf{C}_j$ .

$$\left\{ \frac{\partial}{\partial t} [nf] \right\}_{\text{col}} = \int_{-\infty}^{\infty} \int_0^{4\pi} (n'_j f'_j n' f' - n_j f_j n f) g \sigma d\Omega d\mathbf{C}_j \quad (2.2)$$

Due to the highly complex, integro-differential form of the Boltzmann equation, analytic solutions are possible only for very simple flows with many assumptions. In addition, a detailed form of the collision cross section which is a function of many quantities may be necessary and this further complicates any analysis.

At the cost of a high level of mathematical complexity associated with an integro-differential equation, the Boltzmann equation can be applied to almost any gas flow system due to the very small number of assumptions (molecular chaos, monatomic, and binary collisions) to arrive at the form of the equation and collision integral shown here. Modeling of molecular gases with the Boltzmann equation is possible with the addition of more dimensions for internal energy states and will be extended in Chapters IV and V.

The collision integral also tells us something about the form of the velocity distribution function at equilibrium conditions. Regardless of the initial velocity distribution function, after a sufficient number of collisions, the velocity distribution function will approach an equilibrium form and additional collisions will not further change it. Therefore, the form of the equilibrium velocity distribution function is determined by finding  $f$  such that the collision integral is zero. The equilibrium form, which is known as the Maxwell-Boltzmann velocity distribution function, is given by Eq. 2.3 where  $k$  is the Boltzmann constant,  $T_{\text{TRA}}$  is the translational temperature,  $m$  is the particle mass,  $\mathbf{c}$  is the particle velocity vector, and  $\langle \mathbf{c} \rangle$  is the average particle velocity vector.

$$f_{\text{MB}}(\mathbf{c}) d\mathbf{c} = \left( \frac{m}{2\pi k T_{\text{TRA}}} \right)^{3/2} \exp \left( \frac{-m(\mathbf{c} - \langle \mathbf{c} \rangle)^2}{2kT_{\text{TRA}}} \right) d\mathbf{c} \quad (2.3)$$

### 2.1.2 Simplified Collision Integrals

Much of the complexity of finding solutions to the Boltzmann equation lies in evaluating the collision integral. Because of this, many simplified models for the collision integral have been proposed. An algebraic expression utilizing the Bhatnagar-Gross-Krook (BGK) method [12] is shown in Eq. 2.4, where  $n$  is the number density,  $f_{\text{MB}}$  is the Maxwell-Boltzmann velocity distribution function, and  $\tau_{\text{BGK}}$  is a relaxation time.

$$\left\{ \frac{\partial}{\partial t} [nf] \right\}_{\text{col}} = \frac{n(f_{\text{MB}} - f)}{\tau_{\text{BGK}}} \quad (2.4)$$

This allows the governing equation to continue to describe the evolution through six-dimensional space, but linearizes the collision integral which greatly reduces the number of computations required for evaluation at the expense of ignoring most of the physics that occurs between colliding particles. One physical inconsistency that arises from this greatly simplified collision model is the evaluation of the Prandtl number as unity. Holway [13] proposed the ellipsoidal statistical BGK (ES-BGK) method to obtain better agreement with the Boltzmann equation. Now the collision integral becomes Eq. 2.5 where the equilibrium distribution function is replaced with  $f_G$ , an anisotropic Gaussian distribution function.

$$\left\{ \frac{\partial}{\partial t} [nf] \right\}_{\text{col}} = \frac{n(f_G - f)}{\tau_{\text{ES-BGK}}} \quad (2.5)$$

This model allows for a correction of the unphysical constraint of having a Prandtl number of unity by allowing an added degree of freedom in the equilibrium distribution function.

Although both BGK models greatly simplify the evaluation of the collision integral, they still require modeling the evolution of the probability density function through a minimum of 6 dimensions for a monatomic gas with an additional di-

mension added for each additional internal energy mode of interest for molecular gases.

## 2.2 Continuum Description

One way to reduce the mathematical complexity of the Boltzmann equation is to track macroscopic properties, such as density, velocity, and temperature, rather than each entire probability density function. This can be done through approximating the evolution of the probability density function by the evolution of a select number of moments. Though this increases the number of assumptions made about a gas flow, it still allows accurate evaluation of many flows of interest with a significant reduction of the mathematical complexity.

### 2.2.1 Moments of the Boltzmann Equation

In order to reduce the dimensionality of the governing equation, the evolution of velocity-averaged quantities can be tracked instead. The goal is to track quantities that reduce the mathematical complexity, but maintain sufficient physical accuracy to model realistic gas flows. An average quantity is found by evaluating Eq. 2.6 where  $Q$  is some quantity of interest,  $f$  is the probability density function, and  $\mathbf{c}$  is the particle velocity vector.

$$\langle Q \rangle = \iiint_{-\infty}^{\infty} Q(\mathbf{c}) f(\mathbf{c}) d\mathbf{c} \quad (2.6)$$

If  $Q$  is of the form  $\mathbf{c}^n$ , this is known as taking the  $n$ th moment of the velocity distribution function. Equation 2.7 shows Maxwell's equation of change which is found by taking a moment of the Boltzmann equation.

$$\frac{\partial}{\partial t} [n \langle Q \rangle] + c_m \frac{\partial}{\partial \mathbf{x}} [n \langle \mathbf{c} Q \rangle] = \Delta [Q]_{\text{COL}} \quad (2.7)$$

The collision term,  $\Delta [Q]_{\text{COL}}$ , is zero when  $Q(\mathbf{c})$  is equal to a linear combination of the collision invariants  $Q(\mathbf{c}) = \{m, m\mathbf{c}, mc^2/2 + \epsilon_{int}\}$  where  $\epsilon_{int}$  is the total particle internal energy [14]. These five collision invariants represent the conservation of mass, linear momentum, and energy within the collision process.

Using these collision invariant particle properties in Maxwell's equation of change allows us to write the conservation of mass, linear momentum, and energy as Eqs. 2.8, 2.9, and 2.10, respectively where the specific internal energy is  $e_{int} = \epsilon_{int}/m$ .

$$\frac{\partial \rho}{\partial t} + \frac{\partial}{\partial x_k} (\rho \langle c_k \rangle) = 0 \quad (2.8)$$

$$\frac{\partial}{\partial t} (\rho \langle c_k \rangle) + \frac{\partial}{\partial x_k} (\rho \langle c_k c_i \rangle) = 0 \quad (2.9)$$

$$\frac{\partial}{\partial t} (\rho \langle c^2/2 + e_{int} \rangle) + \frac{\partial}{\partial x_k} (\rho \langle c_k (c^2/2 + e_{int}) \rangle) = 0 \quad (2.10)$$

Using the Maxwell-Boltzmann velocity distribution function to evaluate the moments, these conservation equations become the well known Euler equations. The Euler equations are valid for equilibrium flow simulations at the limit that the Knudsen number approaches zero. For flows where the molecular collisions are too infrequent for the velocity distribution function to be at equilibrium, a set of equations that includes more detail about the degree of nonequilibrium must be used to provide sufficient physical accuracy.

### 2.2.2 Chapman-Enskog Expansion and Navier-Stokes Equations

Instead of modeling the velocity distribution as remaining everywhere in local thermodynamic equilibrium, a higher order perturbation can be used to evaluate the average quantities in Maxwell's equation of change. A perturbation of the velocity distribution function can be written as Eq. 2.11 where  $f_{\text{MB}}(\mathbf{c})$  is the Maxwell-Boltzmann velocity distribution function,  $\xi$  is the perturbation variable and  $\varphi$  are the coefficients.

$$f(\mathbf{c}) d\mathbf{c} = f_{MB}(\mathbf{c}) [1 + \xi \varphi_1(\mathbf{c}) + \xi^2 \varphi_2(\mathbf{c}) + \dots] d\mathbf{c} \quad (2.11)$$

By ignoring any perturbation, the velocity distribution function remains Maxwellian and we arrive at the Euler equations as explained in the previous subsection. Keeping only the first two terms and requiring that the evaluation of the collision integrals remain identically zero for the collision invariant terms results in the unique expansion coefficient shown in Eq. 2.12 where  $T_{TOT}$  is the temperature averaged over translational and internal modes, and  $A_{TOT,i}$  and  $B_{i,j}$  are coefficients [15, 14].

$$\varphi_1 = -\frac{1}{n} \left[ \sqrt{\frac{2kT_{TOT}}{m}} A_{TOT,i} \frac{\partial \ln T_{TOT}}{\partial x_i} - B_{i,j} \frac{\partial c_i}{\partial x_j} \right] \quad (2.12)$$

Using the method of Sonine Polynomial Expansion [14], the coefficients,  $A_{TOT,i}$  and  $B_{i,j}$  can be rewritten in terms of transport coefficients allowing the first perturbation coefficient, shown in Eq. 2.13 [16], to be written in terms of molecular transport quantities, assuming a Newtonian Fluid and Fourier's Law for heat conduction, where  $\mathcal{C}_i$  is the normalized random velocity given by Eq. 2.14,  $q_i^*$  is the normalized heat stress vector given by Eq. 2.15, and  $\tau_{i,j}^*$  is the normalized shear stress tensor given by Eq. 2.16.

$$\varphi_1 = \varphi_1 q_i^* \mathcal{C}_i \left( \frac{2}{5} \mathcal{C}_i \mathcal{C}_i - 1 \right) - \tau_{i,j}^* \left( \mathcal{C}_i \mathcal{C}_j - \frac{1}{3} \mathcal{C}_i \mathcal{C}_j \delta_{i,j} \right) \quad (2.13)$$

$$\mathcal{C}_i = c_i \sqrt{\frac{m}{2kT_{TOT}}} \quad (2.14)$$

$$q_i^* = -\frac{\kappa_{TOT}}{p} \sqrt{\frac{2m}{kT_{TOT}}} \frac{\partial T_{TOT}}{\partial x_i} = \frac{q_i}{p} \sqrt{\frac{2m}{kT_{TOT}}} \quad (2.15)$$

$$\tau_{i,j}^* = \frac{\mu}{p} \left( \frac{\partial u_i}{\partial x_j} + \frac{\partial u_j}{\partial x_i} - \frac{2}{3} \frac{\partial u_k}{\partial x_k} \delta_{i,j} \right) = \frac{\tau_{i,j}}{p} \quad (2.16)$$

The molecular transport quantities,  $\tau_{i,j}$  and  $q_i$ , are directly related to higher order moments of the velocity distribution function which are shown in Eqs. 2.17 and 2.18,

respectively, where  $c$  is a particle velocity,  $\rho$  is the mass density,  $n$  is the number density, and  $\varepsilon_m$  is the energy contained in the energy mode of interest. For the transport of translational energy,  $\varepsilon_m$  can be replaced by  $(mc^2)/2$ .

$$\tau_{i,j} = \rho \langle c_i c_j \rangle - \frac{\rho}{3} \langle c_k c_k \rangle \delta_{i,j} \quad (2.17)$$

$$q_{i,m} = n \langle c_i \varepsilon_m \rangle \quad (2.18)$$

As the Maxwellian velocity distribution function is completely defined by the bulk velocity and temperature, the Chapman-Enskog velocity distribution requires higher order moments related to the shear stress and heat flux which can be estimated from gradients of macroscopic quantities. Now by using the Chapman-Enskog expansion of the equilibrium velocity distribution function in Maxwell's equation of change, the Navier-Stokes equations are found for three-dimensional Cartesian flows where the internal energy modes are described as being in equilibrium with the translational energy mode, shown in Eq. 2.19. Here the conservative vector is given by  $\mathbf{U} = [\rho, \rho u, \rho v, \rho w, E_{tot}]^T$  and  $\mathbf{E}$ ,  $\mathbf{F}$ , and  $\mathbf{G}$  are given by Eqs. 2.20 - 2.22, respectively while  $E_{tot}$  is defined by Eq. 2.23. The specific energy of the  $m$ th energy mode,  $e_m$ , can be written as Eq. 2.24 where  $\zeta$  is the number of degrees of freedom,  $R$  is the gas constant, and  $T_m$  is the temperature associated with the energy mode.

$$\frac{\partial}{\partial t} \mathbf{U} + \frac{\partial}{\partial x} \mathbf{E} + \frac{\partial}{\partial y} \mathbf{F} + \frac{\partial}{\partial z} \mathbf{G} = 0 \quad (2.19)$$

$$\mathbf{E} = \left\{ \begin{array}{c} \rho u \\ \rho u^2 + p - \tau_{xx} \\ \rho uv - \tau_{xy} \\ \rho uw - \tau_{xz} \\ (E_{tot} + p) u - \tau_{xx}u - \tau_{xy}v - \tau_{xz}w + q_{tr,x} + q_{int,x} \end{array} \right\} \quad (2.20)$$

$$\mathbf{F} = \left\{ \begin{array}{c} \rho v \\ \rho uv - \tau_{xy} \\ \rho v^2 + p - \tau_{yy} \\ \rho vw - \tau_{yz} \\ (E_{tot} + p) v - \tau_{xy}u - \tau_{yy}v - \tau_{yz}w + q_{tr,y} + q_{int,y} \end{array} \right\} \quad (2.21)$$

$$\mathbf{G} = \left\{ \begin{array}{c} \rho w \\ \rho uw - \tau_{xz} \\ \rho vw - \tau_{yz} \\ \rho w^2 + p - \tau_{zz} \\ (E_{tot} + p) w - \tau_{xz}u - \tau_{yz}v - \tau_{zz}w + q_{tr,z} + q_{int,z} \end{array} \right\} \quad (2.22)$$

$$E_{tot} = \rho e_{TRA} + \frac{1}{2}\rho(u^2 + v^2 + w^2) + \rho e_{int} \quad (2.23)$$

$$e_m = \frac{\zeta_m}{2}RT_m \quad (2.24)$$

Assuming a Newtonian fluid and Stokes' hypothesis, the shear stress matrix,  $\tau_{ij}$ ,

is given by Eq. 2.25 where  $\mu$  is the coefficient of viscosity.

$$\tau_{ij} = \mu \left( \frac{\partial u_j}{\partial x_i} + \frac{\partial u_i}{\partial x_j} \right) - \mu \frac{2}{3} \frac{\partial u_k}{\partial x_k} \delta_{ij} \quad (2.25)$$

The heat flux terms, shown in Eq. 2.26, are modeled using Fourier's law where  $\kappa_m$  is the coefficient of heat flux for the  $m$ th energy mode and  $T_m$  is the temperature of the  $m$ th energy mode.

$$q_{m,i} = -\kappa_m \frac{\partial T_m}{\partial x_i} \quad (2.26)$$

With the addition of an equation of state, such as Eq. 2.27, the Navier-Stokes equations form a closed set of mathematical equations to describe gas flow.

$$p = \rho R_{gas} T \quad (2.27)$$

With the two separate coefficients in the first perturbation term, the Chapman-Enskog expansion can avoid the unphysical Prandtl number value of unity suffered by the original form of the BGK approximation. However, the Chapman-Enskog expansion does assume that the velocity distribution function can be sufficiently described by just lower order moments and the expansion is only valid when the expansion parameter,  $\xi$ , is small. This expansion parameter is often written in terms of a local Knudsen number of the flow [17, 16], since the Boltzmann H-Theorem states that molecular collisions drive a velocity distribution towards equilibrium and the inverse Knudsen number is a measure of the number of collisions an average molecule experiences over a given length scale. Therefore, the Chapman-Enskog expansion is valid for highly collisional flows (where the Knudsen number is small). In addition, linear relations are used to describe the molecular transport of momentum and energy through the gas flow. Again, these are only valid for velocity distributions that are slightly perturbed from equilibrium, which also coincides with highly collisional flows.

In general, a globally-averaged Knudsen number is often used to determine the physical validity of the Navier-Stokes equations [14]. However, many gas flows with

global Knudsen numbers signifying fully continuum flow may include localized regions that are far from continuum [2, 18] and the Navier-Stokes equations do not have the sufficient physical accuracy to describe the entire gas flow. Because of this, care must be taken in using the Navier-Stokes equations to describe gas flows that are at the edge of the continuum approximation.

### 2.2.3 Higher Moment Equations

More terms of the Chapman-Enskog expansion can be kept to derive other transport equations from the Boltzmann transport equation to increase the physical range of validity. The Burnett equations [19, 20] can be derived if the first two perturbation terms ( $\varphi_1$  and  $\varphi_2$ ) are kept, while the super-Burnett equations [19, 20] are derived if the first three perturbation terms are kept. This may give a more accurate description of the flow field, but there is research [21] that suggests that the Burnett equations can not be used anywhere that the Navier-Stokes equations are invalid, so the added mathematical and numerical complexity of these higher order terms do not guarantee an increased range of applicable flows. This is due to the velocity distribution often being bimodal in many regions where the Navier-Stokes equations fail and the distribution function can not be accurately described with a single perturbation.

Instead of assuming a Newtonian fluid and Stokes hypothesis to model shear stress and using Fourier's law to model heat transfer, separate transport equations for each transport quantity can also be derived using Maxwell's equation of change (Eq. 2.7). For example, Grad's 13 moment approximation assumes a symmetric shear stress tensor and tracks each unique component of  $\tau_{i,j}$  and  $q_i$  for a total of 13 transport equations. Now the closure due to linear transport is unneeded, but additional closure of higher order terms are still (and will always) be needed for

an increase in the number of transport equations. As with keeping higher terms of the Chapman-Enskog expansion, modeling of higher order moments significantly increases the mathematical complexity of the problem with an often unknown increase in physical accuracy over the Navier-Stokes equations.

## 2.3 Numerical Methods

This subsection will outline some numerical methods required to solve the mathematical descriptions of gas flow previously outlined in the chapter. In addition, current hybrid methods that combine different numerical methods are outlined.

### 2.3.1 Deterministic Numerical Methods of Rarefied Flows

Ideally, if the Boltzmann equation is the governing equation for all possible flows, an efficient and accurate numerical scheme that produces a solution to this equation would be preferable over any solution to the mathematical approximations. Unfortunately, due to the evolution in time of a flow variable across the six-dimensional phase space, the solution of the Boltzmann equation requires large computational resources. Grid spacing in velocity space becomes acutely difficult for hypersonic, flow over blunt bodies where the flow transitions from a velocity distribution dominated by a very sharp peak in the free stream to a very diffuse velocity distribution in the high temperature, low Mach number shock layer, and back to a sharp peak in the high Mach number wake. In order to accurately and efficiently solve this type of problem, variable grid spacing throughout velocity space at each point in physical space is required and is still an ongoing area of research [22]. Furthermore, the addition of each separate mode for internal energy increases the number of dimensions which further increases the size of the computational grid necessary and restricts the current simulation of flows to normal shock waves or very simple fore-body flow

fields [23, 24]. Though promising, an increase in maturity must be obtained before the ability to solve the Boltzmann equation over generic hypersonic vehicles is possible.

### 2.3.2 The Direct Simulation Monte Carlo Method

Instead of deterministically finding a solution to the Boltzmann equation which is mathematically complex and requires numerically intensive solution methods, a probabilistic particle method can be used to simulate the physical processes described by the Boltzmann equation without requiring a fully resolved mesh in velocity space. The direct simulation Monte Carlo (DSMC) [10] is one such particle method that simulates representative particles, or simulators, that move and collide with other particles and the vehicle surface. In general, a DSMC simulator maintains its own velocity, internal energy, and specific location and represents a very large number (for example over  $1 \times 10^8$ ) of real particles. A mathematical proof has shown that the DSMC method converges to the Boltzmann equation as the number of particles increases [25].

In the DSMC technique, collisions are treated in a probabilistic manner within each cell using phenomenological collision models that match macroscopic collision rates and are fully decoupled from the movement of particles. This approach places numerical restrictions required to maintain a physically accurate simulation. Because of decoupling of the movement and collide steps, the time-step in each cell should be much less than the mean collision time of particles. In addition, since collision pairs are probabilistically chosen within a cell, these collision cells should be less than the local mean free path to maintain the physical accuracy of the diffusion process in the DSMC method. Collision rates within a cell are computed using a history of

the number of simulators in the cell and the current number of simulators in the cell. The use of these values introduces inherent statistical scatter from the physical and numerical fluctuations. To minimize the numerical fluctuations in each cell, in general, the average number of simulators in a cell should be around or above 20 particles per cell.

A typical DSMC simulation of steady-state gas flows proceeds as follows. The DSMC simulators are initialized throughout a computational grid. Particles are moved throughout the domain ignoring inter-particle collisions. Particles that collide with solid boundaries are processed using a collision procedure consistent with the boundary type. Particle pairs are selected and collisions between pairs that are probabilistically selected are performed. The move and collide routines are repeated until the flow has reached steady-state. After reaching steady state, macroscopic quantities of interest, such as density, velocity, and temperature in each computational cell are sampled at the end of each collide routine and the flux of energy and momentum at each boundary face of interest are sampled for every particle colliding with the boundary. These sampling procedures are repeated for many iterations until the statistical scatter in the macroscopic quantities is acceptably small.

Physically, the probability,  $P$ , of a collision between two simulated particles over a time-step,  $\Delta t$ , is equal to the ratio of the volume of the total cross-section,  $\sigma_T$ , moving at a relative speed,  $g$ , to the total volume of the cell as shown in Eq. 2.28 where  $W$  is the ratio of the number of real particles in the cell with volume  $V_{\text{cell}}$  to the number of simulator particles [10].

$$P = \frac{W\sigma_T g \Delta t}{V_{\text{cell}}} \quad (2.28)$$

Bird's no time counter (NTC) scheme uses this probability to determine the

number of collisions simulated in each cell per time step.

The approximations used to formulate the DSMC method only place restrictions on the cell size and time-step. As long as these are satisfied, there are no physical approximations that invalidate the DSMC method from simulating dilute gas flows at any degree of collisional nonequilibrium. However, the cell size and time-step restrictions place a numerical constraint on the degree of equilibrium flow that can be accurately simulated with the DSMC method. In general, both the mean free path and mean collision time are proportional to the global Knudsen number. For three-dimensional flows, this results in a cubic increase in the number of cells required to resolve a given volume while the number of time-steps increases linearly with the inverse of the Knudsen number. The computational time required can be estimated as the number of cells required multiplied by the number of time-steps which results in the computational time of the DSMC method varying with the inverse of the Knudsen number to the fourth power. For very low Knudsen number flows, the computational requirements necessary to perform an accurately resolved DSMC computation may become prohibitively high.

### 2.3.3 Computational Fluid Dynamics

For flow fields with very low global Knudsen numbers, the use of fully kinetic schemes, such as a deterministic Boltzmann solver or DSMC, requires a large amount of computational resources (both time and memory). However, numerical solution of continuum equations, such as the Navier-Stokes equations, can significantly reduce the required computational resources, while maintaining sufficient physical accuracy in description of the gas flow. With continuum methods, cell size restrictions are dependent on reducing the numerical error associated with discretization, instead

of physical restriction of cell size due to the computational method. In addition, discretization is only required in physical space, rather than throughout the full phase space that is required by a deterministic numerical solution of the Boltzmann transport equation.

Historically, computational fluid dynamics (CFD) methods have used finite-volume methods [26], but there is a growing interest in using finite element methods, such as the discontinuous Galerkin method [27]. Both finite volume and finite element methods allow for implicit formulations which reduce the number of required time-steps needed to reach steady state [28]. In addition, both allow for use of structured or unstructured grids, though additional research is required for use of unstructured grids in regions that contain strong shocks [29, 28]. Both methods provide numerical solutions to the Navier-Stokes equations (shown in Sec. 2.2.2) by the use of a grid that discretizes the space in each physical direction and solves a discretized version of the Navier-Stokes equations. For continuum flows, where the Navier-Stokes equations are valid, CFD methods can provide a sufficiently accurate solution at a much lower computational cost in comparison to kinetic schemes such as the DSMC method [30].

#### **2.3.4 Hybrid Numerical Methods for Partially-Rarefied Flow**

For mixed flows that contain some regions that are considered fully continuum while other regions are rarefied, neither fully kinetic nor continuum schemes can provide the combination of numerical efficiency *and* physical accuracy. For hypersonic flow about a vehicle, regions with very small length scales, such as strong shocks, boundary layers, or sharp edges, and very low density regions, such as the near wake region, can be rarefied, while the rest of the flow field can be considered continuum.

Although some modifications, such as slip models, can be made to model some of the rarefied phenomena in a CFD method, these are only found to work well in specific flow types that they were designed for, specifically attached flow with a well defined boundary layer [30, 31]. Because of this, many hybrid methods that couple kinetic and continuum numerical schemes have been developed. This subsection will outline some hybrid methods that have been developed for simulation of partially-rarefied, hypersonic flows.

### **Unified Methods**

Some research has been performed in developing hybrid methods that combine deterministic Boltzmann solvers, used in the rarefied regions, while using a continuum, Navier-Stokes solver in the continuum region. One such method has been proposed by Kolobov et al. as the Unified Flow Solver (UFS) [32, 33]. This method uses adaptively refined Cartesian cells in physical space and uses the same simulation technique throughout the flow, but using different assumptions depending on the nature of the flow. For example, similarly to the DSMC method, it splits the solution methodology into convection and collision steps. Regardless of the degree of nonequilibrium, the convection (which corresponds to the left hand side of the Boltzmann equation shown in Eq. 2.1) is computed in the same manner throughout the physical domain. Then the calculation of the collision integral is performed depending on an empirical continuum breakdown parameter. In nonequilibrium regions, options for full Monte Carlo integration of the collision integral or simplified BGK approximations are available. In the continuum regions, the calculation of the collision integral is simplified using approximations of the probability distribution function,  $f$ , based on local flow quantities and gradients. This simplification of the collision integral

is reported to be over a factor of 100 faster than the full Monte Carlo integration, making simulation of the continuum region insignificant compared to the rarefied region [32]. However, recently reported results have found that the full Monte Carlo integration of the collision integral within the Boltzmann solver may be nearly 1000 times more expensive compared to a similar DSMC calculation [34]. Extension of a Boltzmann solver to include internal relaxation and chemical reactions is still a research topic of interest. Currently only simplified collision models using the BGK approximation have the capabilities of modeling thermal nonequilibrium relaxation [33]. Inclusion of these models will significantly increase the dimensionality of the collision integral, which can amplify the already high computational requirements.

Le Tallec and Mallinger have proposed another approach that couples a Boltzmann solver with a Navier-Stokes solver by matching consistent half-fluxes at the interface location [35]. The method has been applied to flow of monatomic gas over two-dimensional objects, such as a flat plate or ellipse. Again, this method is unable to simulate the necessary physical phenomena, such as internal energy excitation, that regularly occur in hypersonic flows.

### All particle methods

As an alternative to unified methods that use a deterministic Boltzmann solver for the rarefied regions, modifications to the DSMC method can be made that increase the numerical efficiency in regions that can be considered fully continuum. These are attractive because they require very small modifications to existing DSMC codes and may allow the direct use of DSMC phenomenological models to account for the physical processes important in hypersonic flows. Historically, many of these equilibrium particle methods have either allowed multiple collisions to occur at the end of

each time-step [36, 37, 38] or replaced the collision routine with a new method that re-sampled the particle velocities from a Maxwellian velocity distribution function at the end of each time-step to conserve total linear momentum and energy [39, 40]. All of these methods suffer from introducing numerical dissipation that scales with the cell size which still puts strong restrictions on the cell size.

More recently, Burt and Boyd [41] have proposed a low-diffusion (LD) particle method where particles are forced to move along stream lines and introduces far less numerical diffusion than other methods. The random thermal motion in the LD method is suppressed and tracked using a temperature, much like a continuum method. Current research has been focused on implementing physical models [42, 43] within the LD method and fully coupling the LD method within a DSMC code [44]. One major benefit of an LD-DSMC hybrid method is the transfer of information between each method can be naturally performed as particles move from rarefied to continuum regions or vice versa. However, it has only been tested using smooth mesh density requirements throughout the simulation domain. This has an effect of either decreasing the accuracy of the DSMC method (by using too coarse of a mesh in DSMC regions) or severely increasing the cost of the LD method (by using needlessly refined mesh in LD regions). Research towards improving the efficiency of the LD method such that the computational time required for the LD method is much less than the DSMC method is still required to make an LD-DSMC hybrid method viable for hypersonic flows [45, 46].

### Coupled particle-continuum methods

Typically, dilute flows that display collisional nonequilibrium effects are simulated with the direct simulation Monte Carlo (DSMC) method, while fully continuum flows

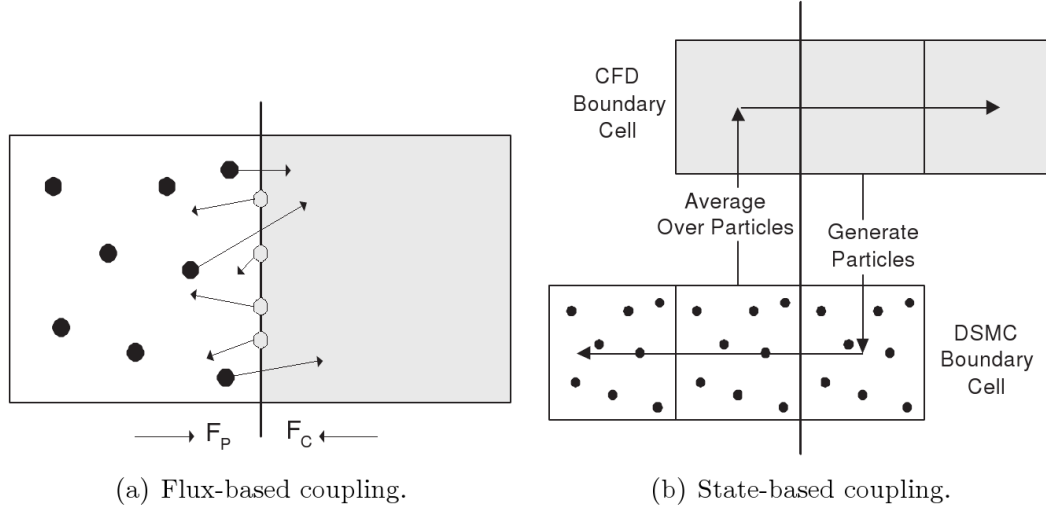


Figure 2.1: Schematic of typical hybrid coupling procedures

are simulated using modern CFD techniques to find solutions to the Navier-Stokes equations. Because of this, a significant amount of research has been performed towards coupling these two preferred methods. This type of hybrid method requires estimation of the interface location by use of a continuum breakdown parameter and formulation of coupling routines into a hybrid framework that remains consistent and numerically efficient. References [47] and [48] provide a discussion of the major considerations involved in coupling particle and continuum methods and a summary of previously published work on these types of coupled schemes.

The method of information transfer between particle and continuum methods can typically be split into two categories: coupling by maintaining consistent fluxes or coupling by maintaining consistent state properties in reservoir cells. Figure 2.1 provides a visual comparison of the two coupling methods. A flux-based, coupling method, which is depicted in Fig. 2.1(a), involves calculating fluxes of conserved variables at the interface location according to each simulation method. The particle flux can be directly calculated by tracking the number of particles that cross

the interface, but the continuum flux must be extrapolated using macroscopic cell-averaged state quantities and their gradients. In general, the estimated fluxes are not the same and are often modified to ensure that mass, momentum, and energy are conserved within the simulation. This modified flux is applied as a boundary condition to both simulation techniques and used to update the continuum solution and to estimate the probability density functions that are sampled to assign DSMC particle information.

With state-based coupling, shown in Fig. 2.1(b), transfer of information between simulation methods is performed by one method providing a Dirichlet boundary condition to the other simulation technique. For the coupling from particle to continuum methods, these values are calculated by performing an averaging procedure to sample state quantities of interest, such as average density, velocity, and energy in DSMC cells along the edge of the interface location. These values are assigned to continuum ghost cells which are used to calculate inviscid and viscous fluxes to update the solution within the continuum domain. For coupling from continuum to particle methods, average state and gradient information is used to estimate the probability density functions of velocities and internal energies in DSMC boundary cells. Before each particle iteration, all simulators in these boundary cells are deleted and new particles are generated consistent with the estimated probability density functions constructed from the continuum data.

Often, an overlap region between the continuum and particle boundary cells is also used, where the particle region is extended into the continuum domain and both simulation methods calculate the solution. These overlap cells can be used to filter the physical inaccuracies from an incorrect initial solution or to compare simulation predictions to ensure that the interface location is located in a near continuum region,

where the Navier-Stokes equations are appropriate.

Wadsworth and Erwin developed a strongly coupled, flux-based hybrid DSMC-CFD scheme and applied it both to one-dimensional shocks [49] and a two-dimensional rarefied slit flow [50]. In these studies, a Maxwellian distribution was used to generate simulation particles at the interface location, which was consistent with the governing Euler equations in the continuum region while the domain boundaries remained fixed. Although the flow was unsteady, the scheme used cumulative averages to calculate the particle to continuum flux to reduce the inherent statistical scatter, while the continuum to particle flux was time accurate based on the current continuum solution.

Hash and Hassan also coupled particle and continuum codes using a flux-based procedure to simulate Couette flow [51] and near equilibrium, hypersonic flow over a sting-mounted blunted sphere-cone [52, 53]. Bird's DSMC method that took into account internal excitation and finite rate chemistry was used as the DSMC module while the modified Navier-Stokes equations were solved on a structured grid in the continuum module. Both the Marshak condition and property interpolation technique were employed to transfer information at the interface. Along much of the rarefied-continuum interface location for the hypersonic flow case, the normal Mach number was small which greatly increased the statistical scatter associated with particle fluxes at the boundary. The statistical scatter was reduced using a smoothing operator over highly sampled data for the property extrapolation before imposing the flux boundary condition. Although these smoothing procedures reduced the scatter for bulk properties, oscillations of properties with large gradients along the boundary could produce unphysical, negative values. In addition, the statistical scatter of gradients were still appreciable with low order smoothing operators so a fourth-order

smoothing procedure with a 7-point stencil had to be used in certain regions. To maintain consistency at the interface, the researchers also found that sampling particle velocities from the Chapman-Enskog velocity probability density function was necessary in regions that displayed significant momentum or energy transfer [51].

Garcia et al. proposed an adaptive mesh and algorithm refinement (AMAR) method [54, 55] that introduces the DSMC methodology at the highest level of refinement of an adaptive mesh scheme. During each time-step, the continuum method is applied to the entire flow. Then, regions that are labeled as rarefied are resolved with a finer mesh that meets DSMC requirements and multiple DSMC time-steps are taken to match the larger, continuum time-step. Particles are generated in reservoir cells around DSMC regions consistent with the time-interpolated continuum data, while particle fluxes across each continuum face are recorded. After the DSMC simulation procedure has reached the current continuum time, DSMC samples are used to update the applicable continuum cells and conserved fluxes are calculated based on the sampled particle simulator fluxes. This method has been successfully applied to one- and two-dimensional gas flows.

Roveda et al. proposed a hybrid particle-continuum method that used a state-based coupling procedure to simulate moving planar shock waves [56] and two-dimensional unsteady flow [57]. The continuum module solved the Euler equations using Nadiga's adaptive discrete velocity (ADV) method [58], while Bird's DSMC method was used in the particle module. Although the state-based procedure had less statistical scatter at the boundary when compared to flux-based coupling procedures, the method was time-accurate which reduced the number of statistically independent samples to the current number of DSMC simulator particles in each cell. In order to reduce the statistical scatter in boundary cells, their method used a

novel algorithm to clone particles in a buffer around the rarefied region to increase the number of nearly statistically independent DSMC samples. This had an effect of reducing the statistical scatter by over a factor of two. Two layers of DSMC reservoir cells were constructed along the DSMC boundary and particles were assigned velocities from the Maxwell-Boltzmann velocity distribution function which is consistent with the continuum solver used in this work.

Wang and Boyd constructed a hybrid framework that coupled a Navier-Stokes solver with the DSMC-Information Preservation (DSMC-IP) scheme [59]. Compared to DSMC, the IP scheme reduces the statistical scatter of macroscopic variables by tracking both microscopic and macroscopic information for each simulator. Although this method was successful for some two-dimensional flows [60, 61], the DSMC-IP scheme was found to produce the incorrect shock jump and thickness for simulation of planar shock waves. A partial remedy was found by reformulating the IP energy flux, but came at the cost of a large computational expense [62].

Wu et al. [63, 64, 65] have developed a loosely-coupled approach, similar to the method which is used in this dissertation, to simulate hypersonic flow over a wedge and expansion of nitrogen gas through a three-dimensional nozzle into near vacuum conditions. This hybrid cycle is employed with shell script routines that couple existing DSMC and CFD codes. However, the interfaces are not allowed to completely move to near continuum locations before updating the continuum region in their proposed algorithm, unlike other methods that first ensure that the interface location is in near continuum regions. Schwartzentruber et al. [66, 11] have shown that this subtle difference can lead to creation of unphysical errors that accumulate in the post-shock region for hypersonic flows that involve strong shocks. In addition, this hybrid technique used the simplified, Maxwell-Boltzmann equilibrium probabil-

ity density function to assign velocities to DSMC simulator particles and a single temperature description of the fluid in the continuum region to reduce the computational cost of the hybrid algorithms. However, this requires the region simulated by DSMC to be expanded into regions where the velocity distribution function is near equilibrium. Results in Chapter IV of this dissertation show that the increase in expense of the continuum solver by the increase in the number of conservation equations is far out-weighed by the decrease in the computational expense to simulate the smaller DSMC region to reduce the overall computational cost of the hybrid method.

Schwartzentruber and Boyd [67] have proposed a Modular Particle-Continuum (MPC) method to simulate partially rarefied, steady-state flow over hypersonic vehicles. This method couples existing DSMC and CFD modules that remain nearly unmodified. State-based coupling is performed with particle velocities assigned with the Chapman-Enskog velocity distribution function using the algorithm of Garcia and Alder [68], and the statistical scatter of particle samples is reduced by use of a novel subrelaxation scheme of Sun and Boyd [69]. The method has been successfully applied to reproduce full DSMC predictions for planar shock waves [70], two-dimensional blunt body flows [67, 66], axi-symmetric blunt body flows [5], and interaction flows [71]. The following chapter provides further details of the MPC method as the work of this dissertation extends the capabilities of this specific hybrid method.

## CHAPTER III

# A Modular Particle-Continuum Method

Many flows of interest contain a wide range of flow length scales and/or mean free path such that neither kinetic nor continuum methods can be applied to the entire flow field in a physically accurate *and* numerically efficient manner. Because of this, multiple hybrid methods have been proposed to simulate partially rarefied flows. A hybrid method that couples the simulation methods of choice in both continuum and rarefied regimes has the advantage of leveraging the experience and advancements in each area to allow the focus of development on the topics applicable to mixed flow simulations, such as the information transfer procedure, demarcation of the rarefied and continuum regions, and the overall hybrid algorithm. For rarefied, hypersonic flows, the prevalent simulation method of choice is the DSMC method, while a numerical solution of the Navier-Stokes equations with modern Computational Fluid Dynamics (CFD) is the most popular simulation method for continuum flows. This work extends the Modular Particle-Continuum (MPC) method [67, 4] for simulating partially rarefied, hypersonic flows. This chapter will provide an overview of the hybrid method, including details about each flow module, the serial structure of the MPC method, and the organization of the memory structures. Finally, the chapter summarizes the new features and capabilities that are added to the flow solver as

a result of this dissertation to extend its capacity to simulate hypersonic, partially rarefied flows.

### 3.1 Flow Modules

#### 3.1.1 DSMC Module

Noncontinuum regions are simulated using MONACO [72], a parallel, general cell-based implementation of the DSMC method that statistically simulates the Boltzmann equation. It is capable of simulating axi-symmetric, two- and three-dimensional flows using body-fitted, unstructured grids. The implementation can run both on serial processors or on distributed memory computing systems using dynamic domain decomposition and the Message Passing Interface (MPI). MONACO can use either Variable Hard Sphere (VHS) or Variable Soft Sphere (VSS) models to simulate the collision process. All results shown in this work are simulated using the VHS model. Various internal relaxation models are available for both rotational [73] and vibrational [74, 75] energy modes and are described in sections 4.2 and 5.1, respectively. The ability to simulate multiple species and chemical nonequilibrium are also available, but are not used in this study. Bird's NTC algorithm, which was described in subsection 2.3.2, is used to compute the collision probabilities. Complete details of MONACO can be found in Ref. [72].

#### 3.1.2 CFD Module

Continuum regions are simulated using LeMANS [28, 76], a laminar, hypersonic code that uses state of the art CFD methods to find a numerical solution to the Navier-Stokes equations that are modified to account for rotational and/or vibrational nonequilibrium for axi-symmetric, two-, or three-dimensional flows. Multiple viscosity models are available; this work uses the VHS viscosity model, as seen in

Eqs. 3.1 and 3.2, to be consistent with the DSMC module. For all simulations presented in this dissertation, diatomic nitrogen is used with a reference diameter,  $d_{ref}$ , of  $4.17 \times 10^{-10}$  m at the reference temperature,  $T_{ref}$ , of 273 K. The power law exponent used in this work is  $\omega = 0.75$  while  $m$  is the molecular mass,  $k$  is the Boltzmann constant, and  $T_{TRA}$  is the local translational temperature.

$$\mu = \mu_{ref} \left( \frac{T_{tra}}{T_{ref}} \right)^\omega \quad (3.1)$$

$$\mu_{ref} = \frac{15\sqrt{\pi mkT_{ref}}}{2\pi d_{ref}^2 (5 - 2\omega) (7 - 2\omega)} \quad (3.2)$$

The inviscid fluxes are evaluated in LeMANS using a modified version of the Steger-Warming flux vector splitting method. This method is less dissipative outside of the shock which is required to resolve the boundary layer, but switches back to the original form of the Steger-Warming fluxes within the shock. Additional details concerning the inviscid fluxes that are used in this work can be found in Refs. [77, 78, 79, 28]. Viscous fluxes are calculated using both values at the cell centers and nodes. For this work, the MPC method uses a point-implicit time-integration method, however, the line implicit formulation is used for full CFD simulations to speed convergence. More details about the numerical implementation can be seen in Refs. [28, 76].

## 3.2 Overview of Existing Modular Particle-Continuum Method

### 3.2.1 Interface Location and Continuum Breakdown

An MPC simulation is initialized with a CFD solution over the entire flow field. In regions where the flow is in collisional nonequilibrium, this initial solution will be incorrect. The MPC method must be able to predict which regions are incorrect and apply the DSMC module to these regions of the flow to arrive at the physically

accurate solution. Therefore, the physical accuracy of the MPC method depends on the DSMC region being sufficiently large to contain all regions of the flow that are locally rarefied. In contrast, the numerical efficiency of the MPC method depends on the DSMC method to *only* be applied to regions where the Navier-Stokes equations can not provide the physical accuracy needed to properly describe the flow. Therefore, accurate prediction of continuum breakdown is vital to ensure that a hybrid method maintains sufficient physical accuracy *and* numerical efficiency.

The MPC method uses the gradient-length, local Knudsen number, shown in Eq. 3.3, where  $Q$  is some macroscopic quantity of interest and  $\lambda$  is the local mean free path, to predict the regions of the flow that are in collisional nonequilibrium.

$$Kn_{GL-Q} = \lambda \left| \frac{\nabla Q}{Q} \right| \quad (3.3)$$

In this work, the gradient-length Knudsen numbers based on mass density,  $\rho$ ; the local speed,  $|\mathbf{V}| = \sqrt{u^2 + v^2 + w^2}$ ; and translational temperature,  $T_{\text{TRA}}$ , are used. Physically, the gradient-length Knudsen number estimates a flow length scale with the gradient of macroscopic properties and compares this to the mean free path. These terms are directly related to the Chapman-Enskog expansion terms, which were described in Sec. 2.2.2, that describe the molecular diffusion of mass, momentum and energy. As with the global Knudsen number, if a flow length scale is on the order of the collision length scale, insufficient collisions occur for the transport properties to be modeled with linear relations. Instead, a more detailed, kinetic description of the flow field should be used. Previous research [80, 81] has found that regions that have a gradient-length Knudsen number less than 0.05 display a continuum prediction that differs from the DSMC prediction by less than 5%. Therefore regions that exhibit a gradient-length Knudsen number less than 0.05 can be simulated with

the continuum module while introducing little physical error.

The local mean free path used in the gradient-length Knudsen number is calculated using Eq. 3.4 where  $n$  is the local number density,  $T_{\text{TRA}}$  is the translational temperature,  $\omega$  is the macroscopic viscosity temperature exponent that appeared in Eq. 3.1, and  $T_{\text{ref}}$  is the temperature that the reference cross section,  $\sigma_{\text{ref}}$ , is calculated at, which is consistent with the variable hard sphere collision model used in the DSMC simulation and the corresponding temperature viscosity relation used within the CFD module. The reference cross section can be calculated using Eq. 3.5 where  $k$  is the Boltzmann constant and  $\mu_{\text{ref}}$  is the coefficient of viscosity at  $T_{\text{ref}}$ .

$$\lambda = \frac{1}{\sqrt{2}n\sigma_{\text{ref}}} \left( \frac{T_{\text{TRA}}}{T_{\text{ref}}} \right)^{\omega-1/2} \quad (3.4)$$

$$\sigma_{\text{ref}} = \frac{15\sqrt{\pi mkT_{\text{ref}}}}{2(5-2\omega)(7-2\omega)\mu_{\text{ref}}} \quad (3.5)$$

Gradients of each quantity,  $Q$ , are calculated in an MPC simulation using the discretized version of the Green-Gauss method [82], which for cell-centered data, can be written as Eq. 3.6 where  $\Omega$  is the volume of cell  $I$ ,  $^{1/2}(Q_I - Q_F)$  is an estimate of the average value along the face between cell  $I$  and its neighbor cell,  $F$ ,  $\overrightarrow{n_{IF}}$  is the unit outward normal of the face between cells  $I$  and  $F$ , and  $\Delta S_{IF}$  is the face area of the face between cells  $I$  and  $F$ .

$$\nabla Q_I = \frac{1}{\Omega} \sum_{F=1}^{N_F} \frac{1}{2} (Q_I - Q_F) \overrightarrow{n_{IF}} \Delta S_{IF} \quad (3.6)$$

At first, the MPC method estimates regions that are in collisional nonequilibrium using the initial full CFD solution to compute the breakdown parameter, so the application of the gradient-length Knudsen number to a fully continuum prediction must label all regions that contain nonequilibrium flows. It is not necessary that this estimation label the correct size of the rarefied regions, since the MPC algorithm

will adaptively move the interface to the correct location as the flow evolves from the initial full continuum solution to the physically accurate final solution. Figures 3.1 and 3.2 show the maximum gradient-length Knudsen number applied to CFD and DSMC simulation results for flow over a cylinder with a free stream Mach number of 12 and global Knudsen numbers based on the cylinder diameter of 0.01 and 0.002, respectively. For both flow conditions, the breakdown parameter applied to the full CFD prediction is able to effectively label the bow shock, thin boundary layer and near wake region as rarefied regions, while the rest of the flow is identified as continuum.

When comparing rarefied regions (where  $Kn_{GL-MAX} > 0.05$ ), the size of the region that is in collision nonequilibrium decreases as the global Knudsen number decreases since the mean free path for the lower Knudsen number case is a factor of five lower in much of the flow region. However, it is interesting to note that, very near the surface of the after body, near the local maximum of  $Kn_{GL-MAX}$ , the decrease in magnitude is only about a factor of 2.5 as  $Kn_\infty$  decreases by a factor of five. This is because the flow can maintain higher gradients in the higher density (smaller mean free path) flow and has been seen by other researchers as well. For example, Figs. 3.3 and 3.4 show the degree of nonequilibrium predicted by DSMC for Mach 10 flow of N<sub>2</sub> over a sphere with global Knudsen numbers of 0.01 and 0.002, respectively [76]. Again, despite the factor of five increase in free stream density, the peak gradient-length Knudsen number, which occurs along the aft-body, only decreases by a factor of 2. Hence, even for flows where the global Knudsen number is much less than unity and signifies flow well within the continuum regime, small regions along the after body may still be in collisional nonequilibrium. This has been seen by other researchers [2] where the degree of nonequilibrium along the after-body surface of hypersonic blunt

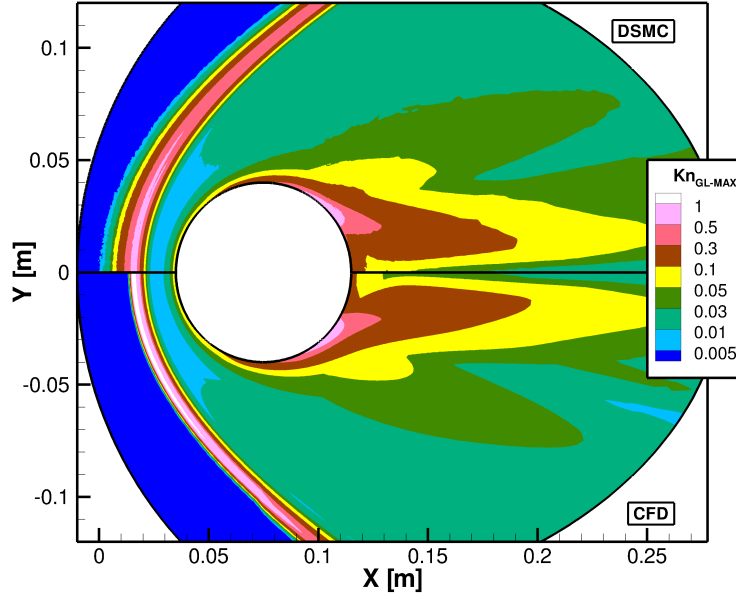


Figure 3.1: Degree of breakdown of collisional equilibrium predicted using  $Kn_{GL-MAX}$  based on the CFD and DSMC simulation results for Mach 12 flow over a cylinder with a global Knudsen of 0.01

bodies has been proposed to be the cause of the over prediction of heat transfer made by continuum methods when compared to available flight measurements.

Figure 3.4 also demonstrates a possible problem of using slip boundary conditions to extend continuum flow techniques. In the wake region, where the flow is separated, the CFD simulation with slip boundary conditions provides very little or adverse improvement in agreement with the DSMC prediction compared to the corresponding CFD simulation results with no slip boundary conditions.

In addition to collisional nonequilibrium, the MPC method must ensure that DSMC is used in other regions of the flow where certain physical processes, such as rotational relaxation, are important but are ignored in the continuum module. For example, if the continuum module assumes that translational and rotational energy modes are in equilibrium, the MPC should ensure that regions that can be

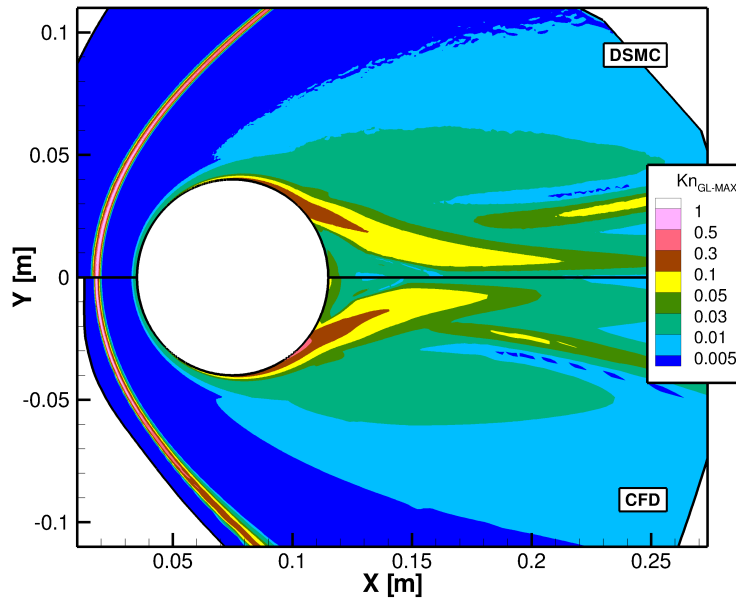


Figure 3.2: Degree of breakdown of collisional equilibrium predicted using  $Kn_{GL-MAX}$  based on the CFD and DSMC simulation results for Mach 12 flow over a cylinder with a global Knudsen of 0.002

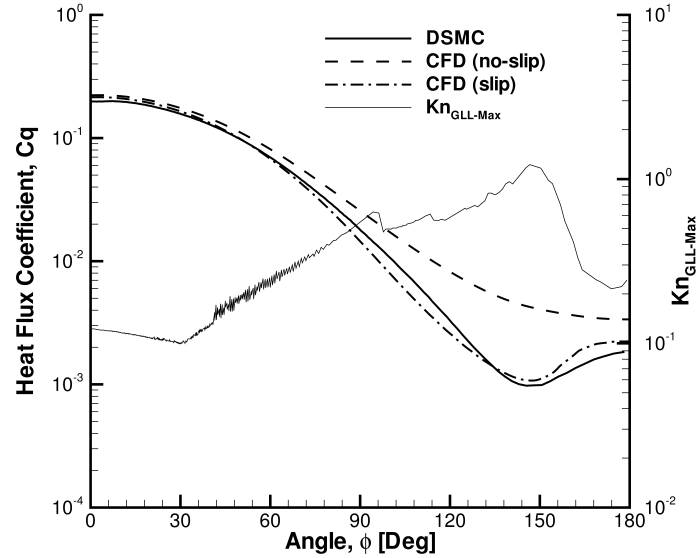


Figure 3.3: Degree of breakdown of collisional equilibrium, using  $Kn_{GL-MAX}$ , and heat transfer to the surface predicted by DSMC and CFD methods for flow over a sphere with a free stream Mach number of 10 and a global Knudsen number of 0.01 [3]

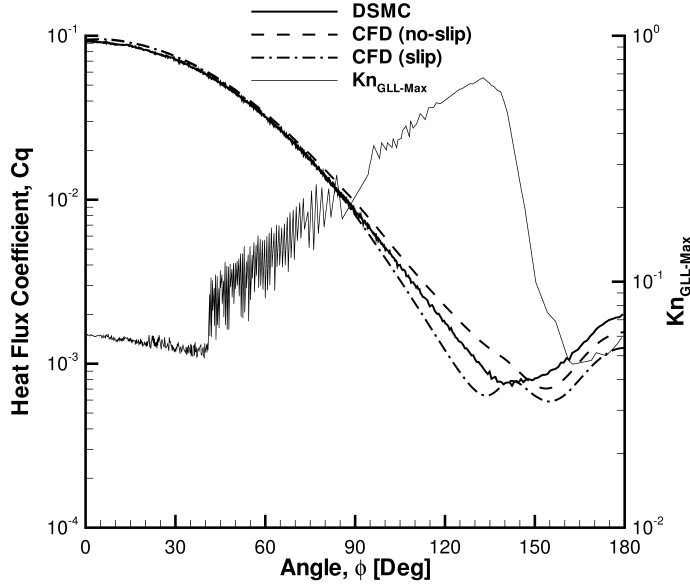


Figure 3.4: Degree of breakdown of collisional equilibrium, using  $Kn_{GLL-MAX}$ , and heat transfer to the surface predicted by DSMC and CFD methods for flow over a sphere with a free stream Mach number of 10 and a global Knudsen number of 0.002 [3]

considered in collisional equilibrium, such that the velocity distribution function can be described by a Chapman-Enskog velocity distribution function, but where the rotational energy modes are not in equilibrium with the translational energy modes, also be assigned to the DSMC module. For near equilibrium flows over blunt bodies, which are of interest for the MPC method, almost the entire region behind the strong expansion displays significant nonequilibrium between rotational and translational modes. This would greatly increase the size of the region simulated with the DSMC module in an application of the MPC method and would have a serious adverse effect on the numerical efficiency. However, Schwartzentruber et al. [66, 5, 83] found that only the strong thermal relaxation in the shock layer has a detrimental effect on the physical accuracy of the MPC method and proposed an additional breakdown parameter shown in Eq. 3.7 which labels any cell where the translational temperature

exceeds the rotational temperature by more than 1% as a DSMC cell.

$$Kn_{\text{ROT-NEQ}} = 5 \times \frac{(T_{\text{TRA}} - T_{\text{ROT}})}{T_{\text{ROT}}} \quad (3.7)$$

In addition to the strong bow shock, this supplementary breakdown parameter has been found to increase the size of the DSMC region behind the recompression wave in the wake of blunt body flows [84]. Results in Chapter IV show that this has an adverse effect on the efficiency of the MPC method, but is required to maintain sufficient physical accuracy in the MPC method with a single equilibrium energy mode modeled in the continuum module. By inclusion of a separate equation to describe the progression of rotational energy in the continuum module, the regions that display rotational nonequilibrium, while the flow is near collisional equilibrium, such that the velocity distribution function can be accurately described with the Chapman-Enskog perturbation of the equilibrium velocity distribution function, can instead be simulated with the continuum module with little physical error.

The MPC method uses a final breakdown parameter given by Eq. 3.8 where the DSMC module is used in cells with  $Br > Br_{\text{cutoff}}$  and the CFD module is used elsewhere.

$$Br = \max(Kn_{GL-\rho}, Kn_{GL-T_{\text{TRA}}}, Kn_{GL-|V|}, Kn_{\text{ROT-NEQ}}) \quad (3.8)$$

Periodically, the MPC method recalculates the breakdown parameter using the most physically accurate information available in each cell. Then, a simple smoothing operator, shown in Eq. 3.9 where  $Br_I$  is the breakdown parameter in the current cell,  $Br_F$  is the breakdown parameter in a neighboring cell, and  $N_F$  is the number of neighbors, is used to reduce the effect of statistical scatter in regions that use DSMC data.

$$Br_I = \frac{1}{N_F + 1} \left( Br_I + \sum_{F=1}^{N_F} Br_F \right) \quad (3.9)$$

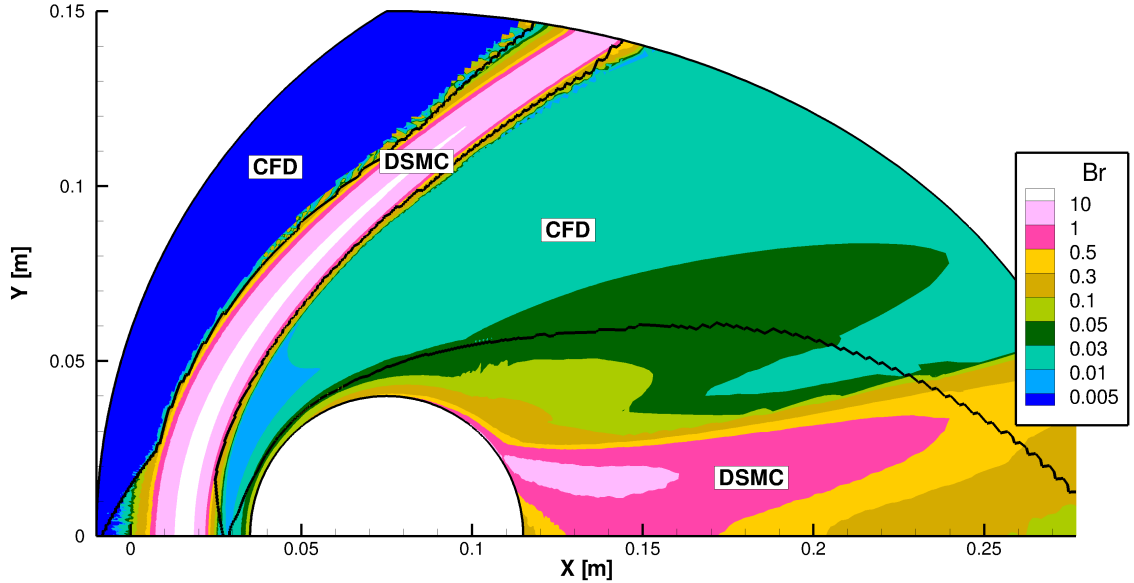


Figure 3.5: Final interface location and breakdown parameter, as defined by Eq. 3.8, for Mach 12 flow over a cylinder with a global Knudsen number of 0.01.

This smoothing operator is applied repeatedly a user specified number of times (typically between zero and five) and the final, smooth breakdown parameter is used to set the boundary between continuum and rarefied flow modules. It is important to note that since the cutoff parameter has been determined empirically, any slight change due to a smoothing algorithm is acceptable.

An example of contours of the breakdown parameter and the final interface location used by the MPC method for Mach 12 flow over a cylinder with a global Knudsen number of 0.01 using a cutoff value of  $Br_{cutoff} = 0.05$  is shown in Fig. 3.5. Here, the MPC method has successfully started with the interface location based on the continuum data (shown in Fig. 3.1) and adaptively moved the interface so that the DSMC module is applied to all rarefied regions. This is clearly visible where the MPC method has adaptively widened the nonequilibrium region to simulate the full shock structure, as it is well known that continuum methods underpredict the shock thickness.

### 3.2.2 Mesh Refinement

As outlined in Sec. 2.3.2, the mesh required by the DSMC method must be sufficiently small to ensure that the distance between colliding particles is less than the local mean free path,  $\lambda$ . Since DSMC cells are used to sort and collide particles, these cells should be less than or on the order of the mean free path to maintain the physical accuracy of the method. Implementation of dynamic sub-cells within the DSMC method allows the cell-size restriction to be slightly relaxed, but cells still should not exceed more than  $2 - 3\lambda$  in each direction to maintain physical accuracy of the simulation. These cell-size requirements are very different than those required by CFD techniques to find numerical solutions to the Navier-Stokes equations, where the cell size should be small enough that the error associated with the discretization of the partial differential equations is sufficiently small.

In addition, current solutions of the Navier-Stokes equations that contain strong bow shocks and/or thin boundary layers require quadrilateral cells in two dimensions (or hexahedral cells in three dimensions). Use of unstructured triangular (or tetrahedral) meshes to resolve these flow features is still an ongoing research topic [29, 85, 86]. This requirement necessitates the MPC simulation method be initialized with a full CFD solution on a quadrilateral (or hexahedral) mesh.

Typically, the DSMC sizing requirements necessitate a finer mesh than the continuum cell size requirements. For example, Fig. 3.6 shows contours of the mean free path for Mach 12 flow over a cylinder with a global Knudsen number of 0.002. The variation in collision length scales about this geometry exceeds two orders of magnitude and corresponds to the local spatial resolution required by the DSMC method. Across the bow shock, the mean free path has decreased by about a factor of three. There is an additional reduction by a factor of eight as the flow traverses

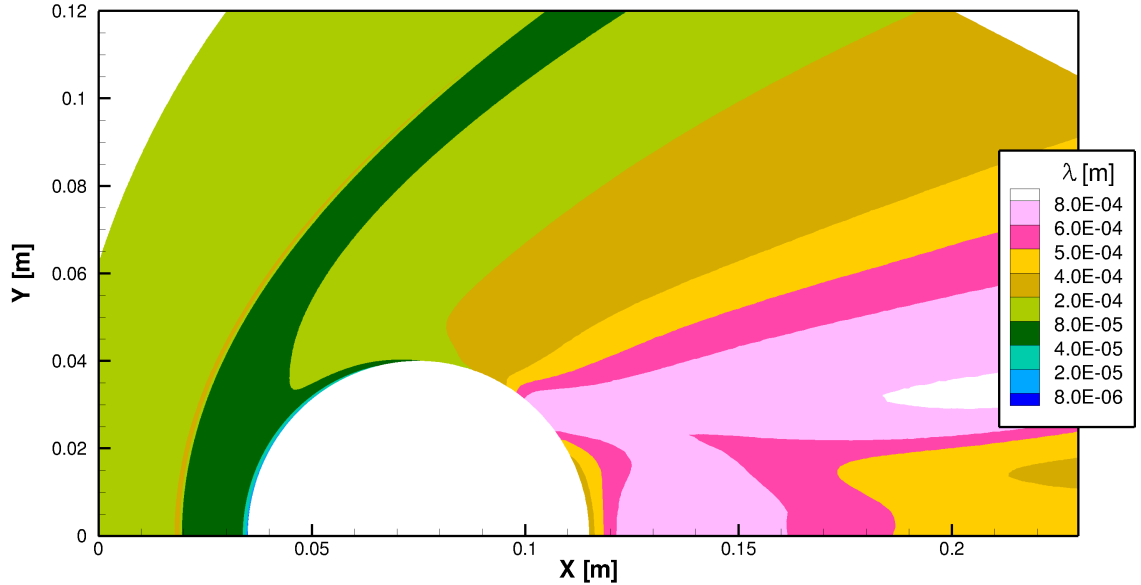


Figure 3.6: Variation of mean free path for Mach 12. flow over a cylinder with a global Knudsen number of 0.002.

from the rear of the bow shock, through the thermal boundary layer, to the cool surface. Figure 3.7 shows the typical meshes used in each simulation method for this same flow condition. Here the DSMC mesh is refined to about  $2\lambda$  in each direction and requires a significantly finer mesh throughout the entire shock layer.

Though DSMC cells should be less than the mean free path in all directions, it is especially important in the direction of the flow gradient, as this is the direction that the probability density function of particle properties changes most. To reduce complications associated with coupling the two flow modules, the DSMC mesh is created as a refinement of the continuum mesh in the MPC method. First, an estimate of the local mean free path is calculated everywhere in the flow field using the initial full CFD solution. Next, the MPC method creates a quadrilateral DSMC mesh that meets its cell size restrictions by refining the provided continuum mesh in the following way. Refinement in each direction is calculated using Eq. 3.10, where  $Q$  is the flow variable with the maximum flow gradient. The dot product between

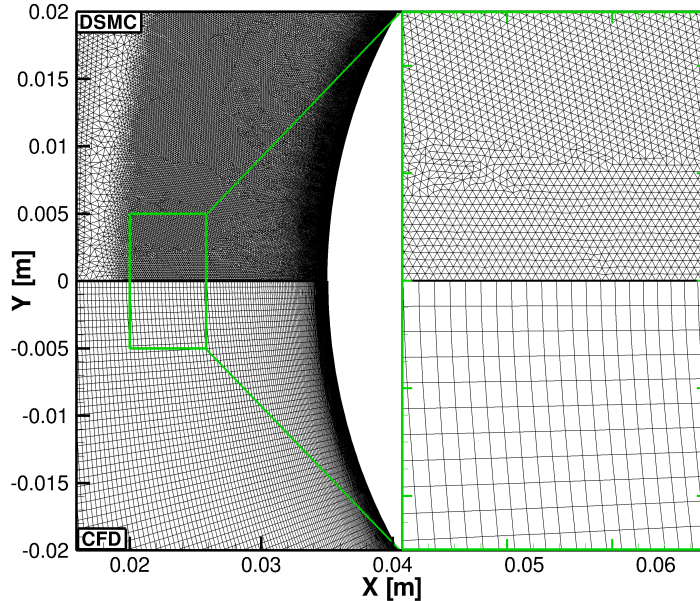


Figure 3.7: Comparison of DSMC and CFD mesh densities in the shock layer for Mach 12. flow over a two-dimensional cylinder with a global Knudsen number of 0.002

the face unit vector,  $\hat{n}_f$ , and the maximum gradient direction,  $\frac{\nabla Q}{|\nabla Q|}$ , determines the alignment of the cell face with the direction. For example, if the cell is perfectly aligned with the maximum flow gradient (where  $\hat{n}_f$  is perpendicular to  $\frac{\nabla Q}{|\nabla Q|}$ ), this dot product is zero and the cell is refined by a factor of  $F\lambda$  in that direction. Conversely, the refinement for the other direction is relaxed to  $F\lambda(g+1)$ . Typically, the value of  $g$  is selected to be between zero and nine which corresponds to cell aspect ratios between unity and ten. Higher aspect ratio cells in DSMC are typically employed along the axis of rotation in axi-symmetric flows, where the flow gradients are in the direction of this rotation axis, to increase the number of simulator particles in these cells.

$$r_f = \frac{l_f}{F\lambda \left( g \left| \hat{n}_f \cdot \frac{\nabla Q}{|\nabla Q|} \right| + 1 \right)} \quad (3.10)$$

A schematic of the mesh refinement procedure is shown in Fig. 3.8 where the

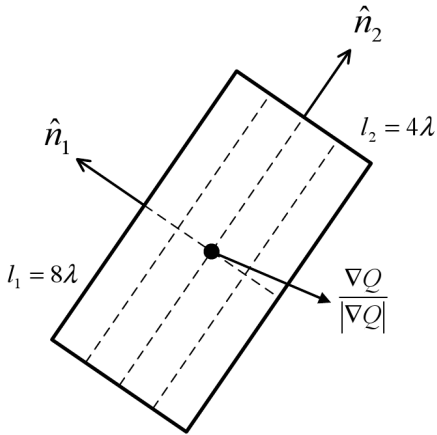


Figure 3.8: Schematic of mesh refinement calculation on continuum cell [4]

outer solid cell is the continuum cell with face normal vectors and the direction of maximum gradient. Here, the coarse, continuum cell has the dimensions of  $8\lambda \times 4\lambda$ , while the gradient is very near normal to the  $\hat{n}_2$  face vector. Taking  $F = 1$  and  $g = 3$  results in the DSMC cells, shown with dashed lines, where the cell is refined to one mean free path ( $\lambda$ ) in the direction of maximum gradient and to  $4\lambda$  in the direction of smallest gradient.

The DSMC module used in this work requires the mesh refinement to be consistent across each neighbor face to eliminate any hanging nodes. Therefore, a simple algorithm is employed to ensure that all cells are refined consistently and that the largest refinement factor is still maintained. This can lead to an over refined mesh in some regions if there is a very large variation in refinement factors along a line of neighbors. For an MPC simulation of very near equilibrium flows, this may occur along the surface due to the enormous variation in mean free path between the front and aft stagnation points. For very low Knudsen number flows, much of the region that requires the largest refinement factors experiences highly collisional flow, which are simulated (on a different coarse mesh) by the continuum module. There-

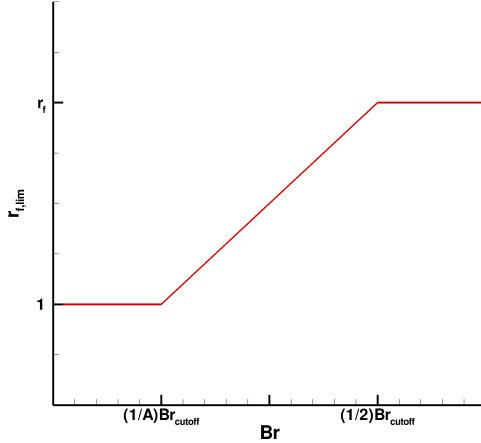


Figure 3.9: Schematic of the refinement limiter as a function of the local breakdown parameter

fore, the MPC method only refines cells that are rarefied, or nearly rarefied. This is implemented by limiting the refinement factor in each cell using Eq. 3.11.

$$r_{f,lim} = \begin{cases} \max\left(1, r_f \left(1 - \frac{2A}{ABr_{cutoff} - 2Br}\right)\right) & \text{if } Br < \frac{Br_{cutoff}}{2} \\ r_f & \text{if } Br > \frac{Br_{cutoff}}{2} \end{cases} \quad (3.11)$$

Here, the refinement is unchanged for cells that have an initial breakdown parameter greater than half of the cutoff parameter. Then the refinement is multiplied by a factor that decreases linearly from unity at  $Br = \frac{1}{2}Br_{cutoff}$  to zero at  $Br = \frac{1}{A}Br_{cutoff}$ . The factor  $A$  must be greater than two and is typically set to values between two and eight. For cells with the initial breakdown parameter less than  $Br_{cutoff}/A$ , no refinement is used. A plot of this limiting procedure is shown in Fig. 3.9 which shows that cells that exhibit a high level of collisional nonequilibrium maintain DSMC refinement levels, while regions that are initially predicted to be very near equilibrium (and should remain very near equilibrium) are not refined since these cells are always simulated with the continuum flow module. It should be noted that even though the refinement factor is set to unity in cells where the breakdown parameter is

less than  $B_{rcutoff}/A$ , the algorithm that eliminates hanging nodes will set a refinement factor based on neighbor (or neighbor of neighbor, etc.) cells that display larger collisional nonequilibrium effects. Once the refinement in each continuum cell is set to be consistent through all face neighbors, the node indices and mesh connectivity for the refined DSMC mesh are computed and the full DSMC mesh structure is created.

### 3.2.3 Information Transfer

The modular implementation of the MPC method allows both DSMC and CFD modules to maintain their own mesh and data structure. Information is transferred between each flow module using a state-based coupling procedure which has been successfully demonstrated by other researchers [56, 57, 87, 61, 64]. The state-based coupling procedure assigns boundary cells on the edge of each module domain and transfers flow information, such as density, velocity components, and temperatures to these cells from corresponding cells of the other module. Rarefied boundary cells act as reservoir cells, while the continuum boundary cells are used in the same manner as ghost cells. Figure 3.10 shows a schematic of how data is transferred between the two modules at an interface location. After calculation of the breakdown parameter (shown in Eq. 3.8), regions are assigned to continuum or rarefied flow modules using the procedures described in Sec. 3.2.1. Next, DSMC overlap cells are extended to create a buffer region. This buffer region is used throughout the unsteady portion of the simulation as the MPC method relaxes the initial CFD solution to reproduce the full DSMC result. In order to obtain an accurate DSMC prediction in rarefied regions, the buffer region *must* be large enough to eliminate any error caused by the possibly inaccurate DSMC boundary conditions provided by the initial CFD prediction. The

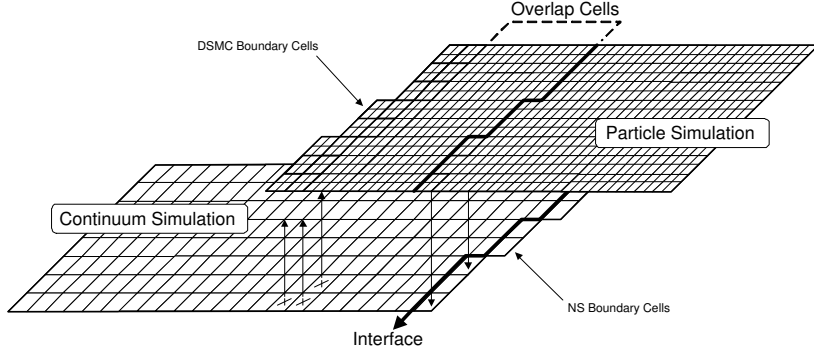


Figure 3.10: Hybrid particle-continuum coupling procedure [4]

number of overlap cells is a user defined input variable, and typical simulations use between six and twenty overlap cells. Then, boundary cells are added along the edge of both particle and continuum regions. The numbers of boundary cells for each flow module are also user input variables. Typically, two DSMC boundary cells are employed, while one or two CFD boundary cells are used in an MPC simulation. Two DSMC boundary cells are used to ensure that high velocity particles, that are associated with the tail of the velocity distribution function and may move across more than one cell in a time-step, are accurately captured in the DSMC region. Use of only one DSMC boundary cell may cause the first DSMC cell of the rarefied region to receive a noticeably reduced flux. The probability of particles traversing three full DSMC cells in one time-step is much less likely and the inability to capture this portion of particle flux in the first layer of DSMC cells creates an insignificant error. It should be also noted that the number of boundary cells is applied at the continuum level cell, so the user input is the *minimum* number of DSMC boundary cells. Therefore, the number of DSMC boundary cells is typically higher due to the mesh refinement that exists between continuum and rarefied meshes. The CFD module requires two layers of boundary layer cells to calculate the correct gradients when higher order, MUSCL schemes are used to compute the inviscid flux at each

face, while one layer of CFD boundary cells is adequate for first order simulations.

Once the rarefied and continuum regions are established, information transfer across the interface can be performed by updating the boundary cells with data from the other flow module. Then, flux calculations are handled internally within each flow module using existing procedures.

For information transfer from the continuum solver *to* the rarefied module, the state-based coupling consists of creating particles and assigning velocities and internal energies consistent with the data contained within the cell-averaged Navier-Stokes data. At the beginning of each DSMC time-step, all particles remaining in DSMC boundary cells (and pure continuum regions) are deleted. Then, particles are created in each DSMC boundary cell consistent with the density of the corresponding continuum cell,  $\rho_{cc}$ ; the numerical particle weight of the cell,  $W_{rc}$ ; and the DSMC cell volume,  $V_{rc}$ . The random molecular velocities of each particle are assigned by sampling from the Chapman-Enskog probability density function, which is consistent with the description of the velocity distribution function in the continuum module and is shown in Eq. 3.12 where  $f_0$  is the Maxwell-Boltzmann velocity distribution function and  $\varphi_1$  is the first expansion term defined by macroscopic variables and gradients in Eq. 2.13.

$$f_{CE}(\mathcal{C}) = f_0(\mathcal{C}) [1 + \varphi_1] \quad (3.12)$$

This velocity probability density function is sampled using an acceptance-rejection scheme outlined by Garcia and Alder [68]. These thermal velocities are superimposed on the averaged, bulk velocities to assign the velocity to each particle. Initial particle locations are assigned randomly within the cell. The rotational energy of each particle is sampled from the equilibrium, Boltzmann probability density function by method of inverse transform sampling based on the description of rotational temperature

within the continuum module. This particle generation procedure is performed before all particles are moved in DSMC and also when new cells are added to the DSMC module which occurs at the initialization of the simulation and when the rarefied-continuum interface has adapted towards regions of near equilibrium.

For information transfer from the rarefied module *to* the continuum module, bulk properties are sampled at each iteration within each continuum level cell. Bulk properties in each continuum cell can be easily calculated using Eqs. 3.13-3.17, where  $N_{real}$  is the number of real particles in the cell,  $N_{rc}$  is the number of rarefied cells in the corresponding continuum cell,  $N_{P_{rc}}$  is the number of simulators in the rarefied cell, and  $W_{rc}$  is the numerical particle weight factor of the rarefied cell. The sample of bulk density in the continuum cell over one iteration can be calculated using Eq. 3.14 where  $\rho$  is the density and  $m$  is the mass of each particle. Bulk velocity components are calculated using Eq. 3.15 where  $c_{i,P_{rc}}$  is the velocity component of a simulator in a rarefied cell. The translational temperature can be estimated at each time-step using Eq. 3.16 where  $k$  is the Boltzmann constant and  $\langle c_i^2 \rangle$  is defined by Eq. 3.17. In addition, a correction factor, proposed by other researchers [56, 57], is used to increase the consistent depression of translational temperature by use of a small number of samples, where  $s = \sum_{rc=1}^{N_{rc}} N_{P_{rc}}$  is the total number of samples (and particles) over one time-step in the continuum cell.

$$N_{real} = \sum_{rc=1}^{N_{rc}} \sum_{P_{rc}}^{N_{P_{rc}}} W_{rc} \quad (3.13)$$

$$\rho = \frac{m N_{real}}{V_{cc}} \quad (3.14)$$

$$u_i = \langle c_i \rangle = \frac{1}{N_{real}} \sum_{rc=1}^{N_{rc}} \sum_{P_{rc}=1}^{N_{P_{rc}}} c_{i,P_{rc}} W_{rc} \quad (3.15)$$

$$T_{TRA} = \frac{s}{s-1} \frac{m}{3k} [\langle c_i^2 \rangle - u_i^2] \quad (3.16)$$

$$\langle c_i^2 \rangle = \frac{1}{N_{real}} \sum_{rc=1}^{N_{rc}} \sum_{P_{rc}=1}^{N_{P_{rc}}} c_{i,P_{rc}}^2 W_{rc} \quad (3.17)$$

Although the statistical scatter associated with the sample of bulk properties at the continuum cell level is smaller than the scatter of sampled properties at the rarefied cell level or sampled fluxes at faces, the scatter of properties at each time-step is still too large to apply directly to continuum boundary cells. This level of scatter applied to boundary cells for the continuum module would create numerical instabilities. Instead, a subrelaxation technique, proposed by Sun and Boyd [69], is employed which uses an exponential moving average of a quantity,  $Q$ , shown in Eq. 3.18, where  $\langle Q \rangle_j$  is the average of a quantity,  $Q$ , at step  $j$ ,  $\langle Q \rangle_{j-1}$  is the average of quantity  $Q$  at the previous time-step,  $Q_j$  is the current sampled quantity at time-step  $j$ , and  $\Phi$  is the subrelaxation coefficient.

$$\langle Q \rangle_j = (1 - \Phi) \langle Q \rangle_{j-1} + \Phi Q_j \quad (3.18)$$

This subrelaxation procedure is applied to all quantities,  $Q = \rho, u_i, T_{TRA}$ , to provide continuum cells with boundary data with a reduction in the statistical scatter. Typically, a subrelaxation parameter value of  $\Phi = 0.001$  is used which contains a sufficiently low level of scatter that is associated with  $1/\Phi = 1,000$  samples. Though this technique introduces a time lag, it is appropriate to use for steady-state flows and has an overall effect of reducing the computational expense by decreasing the number of time-steps required between coupling procedures of each flow module. The subrelaxation average is used for boundary cells and throughout the entire rarefied portion of the domain during the unsteady portion of the MPC cycle to recalculate the breakdown parameter. In addition, a correction factor, proposed by Sun and Boyd [69], is applied to effectively remove the old time history using Eq. 3.19 where  $j$  is the current time-step,  $i$  is a previous time-step where the corrected average,  $\langle Q \rangle'_i$ ,

was calculated.

$$\langle Q \rangle'_j = \langle Q \rangle_j + \frac{(1 - \Phi)^{j-i}}{1 - (1 - \Phi)^{j-i}} \left( \langle Q \rangle_j - \langle Q \rangle'_i \right) \quad (3.19)$$

Sun and Boyd [69] have shown that this correction should only be performed when the correction coefficient is between zero and unity, which is satisfied when  $j = 1/\Phi + i$ .

### 3.2.4 Hybrid Data and Algorithm Structure

Both CFD and DSMC modules within the MPC method maintain their own data structures and mesh for the entire flow field. However, as described in the preceding subsection, the DSMC mesh is created by refining the continuum mesh to meet DSMC cell size restrictions. This simplifies the modular hybrid structure so that each continuum cell contains exactly  $r_1 \times r_2$  DSMC cells, where  $r_1$  and  $r_2$  are the refinement levels in each direction for the continuum cell. The MPC method utilizes a modular data structure that leaves each flow module's data structure intact. Additional data required by the MPC method, to demarcate regions to each flow module and update or transfer information, is kept in a separate data structure. Figure 3.11 shows a schematic of the organization between CFD, DSMC, and hybrid data structures. The hybrid array of structures is created to be consistent with the index notation of the continuum data structure. The hybrid element contains information pertinent to the MPC method, such as if the cell is considered (p)article or (c)continuum, data required for information transfer between flow modules, and a list of pointers to the corresponding DSMC cells that are contained in the continuum cell. Therefore, given a continuum cell index, the corresponding hybrid element can be immediately accessed and used to access the corresponding DSMC cells. An additional hybrid data structure is maintained that, given a DSMC cell index, provides the corresponding continuum cell index. With these two hybrid data structures, given an index from

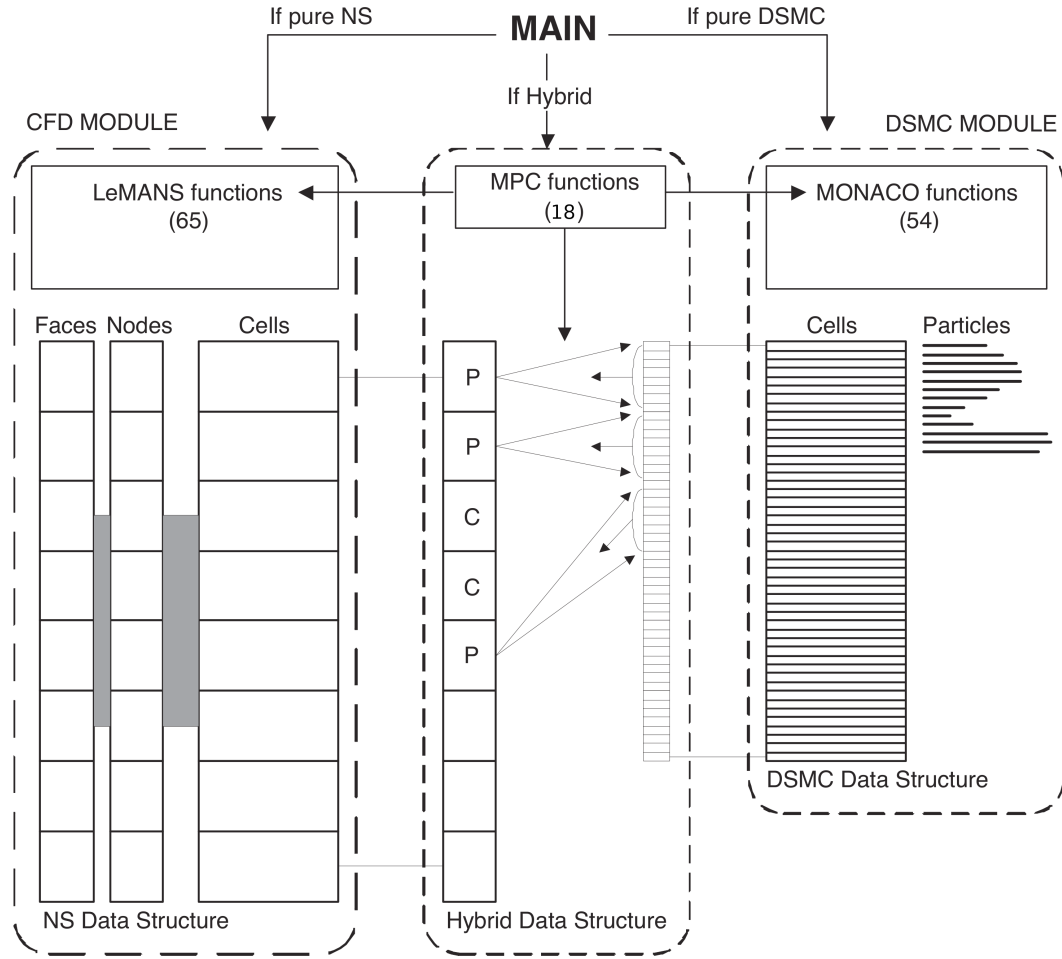


Figure 3.11: Organization of the data structures used by the flow modules and MPC method [4]

one module, any hybrid function can find the cell index corresponding to the other flow module quickly and efficiently.

An outline of the MPC method cycle is as follows:

1. Load a grid-independent, full Navier-Stokes solution on a structured mesh.

Use the continuum breakdown parameter (Eq. 3.8) to set up initial interface locations. Create overlap regions into the initial continuum domain. Create a DSMC grid by refining the CFD grid to meet local cell size restrictions using the initial continuum result and Eq. 3.11. Generate particles inside the DSMC

domain and overlap regions.

2. In particle boundary cells, destroy all old particles and create new DSMC particles based on Navier-Stokes information in corresponding cells. Sample particle thermal velocities from the Chapman-Enskog velocity distribution function and particle internal energies from Boltzmann energy distribution functions. Cycle through the DSMC solver for one time-step. Update hybrid macroscopic quantities using the subrelaxation approach (Eq. 3.18). Repeat a prescribed number of times (typically  $1/\Phi + 10$  iterations).
3. Re-evaluate the breakdown parameter; if needed, move interfaces, create particles in new DSMC cells, and destroy particles in newly labeled pure continuum cells.

*IF* Interfaces have significantly changed (number of DSMC cells increases by more than a user specified percentage), save and output the solution, and go to step 2.

*ELSE* Save and output the solution and update the Navier-Stokes boundary cells with the subrelaxation averages and continue.

4. Cycle through the Navier-Stokes solver. Repeat until converged to a user specified tolerance.
5. Re-evaluate the breakdown parameter; if needed, move interfaces, create particles in new DSMC cells, and destroy particles in newly labeled pure continuum cells.

*IF* Interfaces have significantly changed or steady-state has not been reached, save and output the solution and go to step 2.

*ELSE* Continue.

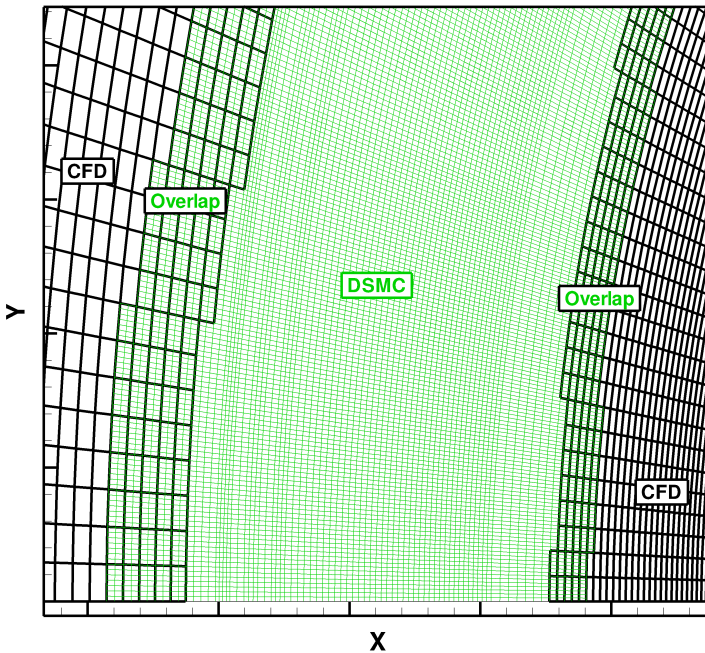


Figure 3.12: Schematic of CFD and DSMC meshes with overlap regions around a nonequilibrium shock

6. Remove overlap regions, delete particles in these regions, and save and output the solution.
7. In particle boundary cells, destroy all old particles and create new DSMC particles based on Navier-Stokes information in the cells. Cycle through the DSMC solver. Repeat for a prescribed number of iterations and collect samples.
8. Update the Navier-Stokes boundary cells and further converge continuum region.

*IF* DSMC statistical scatter and Navier-Stokes residual are below user specifications, end.

*ELSE* Save and output the solution and return to step 7.

Figure 3.12 shows the layout of the DSMC and CFD meshes with overlap regions around a nonequilibrium bow shock during the unsteady portion of an MPC sim-

ulation. For this simulation, five overlap cells were used and are shown where the CFD and DSMC meshes coincide in space. Although a mesh that covers the entire flow field is maintained by each flow module, only cells that are simulated are shown. If, after application of the DSMC module, any of the overlap region displays translational nonequilibrium (predicted with the breakdown parameter calculated using the DSMC information on the continuum level mesh), the DSMC region will be expanded and the buffer region is expanded further until the interfaces have stopped moving.

### **3.3 Extension of a Modular Particle-Continuum Method**

This section summarizes the new capabilities added to the MPC method as part of this dissertation. These improvements are developed to extend the usefulness and range of applicability to simulate flow fields with a higher level of physical accuracy. Inclusion of rotational nonequilibrium and vibrational excitation increases the range of applicability or increases the physical accuracy and predictive capability of flows to which the MPC method has been previously applied. Other routines, such as parallelization enables the future development of other capabilities, such as the full three-dimensional implementation.

#### **3.3.1 Rotational Nonequilibrium**

The extension of the continuum module to simulate nonequilibrium between translational and rotational energy modes includes solving an additional partial differential equation. Consistent physical models across the flow solvers are used to ensure that full DSMC simulations can continue to be used as a verification tool. With the added physical accuracy of the continuum module, the size of the region of flow that uses DSMC can be decreased, which increases the overall efficiency of

the MPC method. However, careful formulation of the breakdown parameter must be performed to ensure that the flow simulated with the continuum module is indeed both near collisional equilibrium, such that the velocity distribution function can be described with the Chapman-Enskog expansion, *and* the rotational energy distribution function is near equilibrium, such that the rotational energy distribution function can be described by a Boltzmann energy probability density function, with little additional error. A detailed explanation of the changes required to implement rotational nonequilibrium across the entire MPC method and verification and validation of the implementation with three different hypersonic flow cases is described in Chapter IV.

### 3.3.2 Vibrational Nonequilibrium

For almost all atmospheric hypersonic flows of interest, the amount of kinetic energy available in the post-shock region of the flow field is sufficiently high that inclusion of vibrational excitation in any simulation is required to maintain an acceptably high level of physical accuracy. Even a small degree of energy that the vibrational mode may remove from the translational modes has an effect on the flow field. First, vibrational energy transfer to the surface is much lower than the fully activated energy modes, so energy transferred to vibrational modes often reduces the heat transfer. In addition, vibrational excitation serves to reduce the post-shock pressure, which reduces the shock stand-off distance. Finally, accurate prediction of the vibrational excitation process is vital to future inclusion in the MPC method of chemical reactions and finite rate chemical processes that are also important for many hypersonic flows of interest. The implementation of vibrational excitation

in the MPC method is described in Chapter V. Consistent vibrational relaxation models are outlined, along with changes to the information transfer algorithms to maintain a combination of physical accuracy and efficiency within the MPC method. Finally, the new implementation is verified with comparison of flow results to full DSMC predictions.

### 3.3.3 Parallelization

The computational requirements of each separate flow module, even for two-dimensional flows, often become too demanding to maintain an acceptable level of physical and numerical accuracy while obtaining a solution in a reasonable amount of time on a serial processor. Although processor speeds have improved, much of the recent increase in computing capability in recent years comes in large clusters of processors performing smaller portions of the computation in parallel. A parallel implementation of the MPC method enables simulation of three-dimensional hypersonic flows that contain regions of thermal nonequilibrium. However, due to the large memory and CPU time requirements, careful consideration must be taken to ensure that the MPC method maintains both a high level of physical accuracy and efficiency. In addition to reducing the necessary wall clock time, these parallel operations also significantly reduce the required amount of memory for each single processor since only a small portion of the computational mesh and solution is stored on each processor.

With a modular implementation, such as the MPC method, where a DSMC, a CFD, and an MPC data structure are maintained to reduce the number of modifications performed to the flow modules, parallelization becomes an enabling feature for flow simulations that require large computational grids and expensive physical

models. The MPC method is parallelized using dynamic domain decomposition with emphasis on maintaining efficient and consistent computational load balance procedures to the heterogeneous data with fluctuations in flows that change as the continuum-rarefied interface changes. The full implementation of the parallel MPC method is outlined in Chapter VI. In addition, the chapter outlines the verification of the parallel implementation with comparison of serial flow predictions of the MPC method, and an estimate of the overhead of the parallel processes for a typical application of the MPC method.

### 3.4 Summary

This chapter has outlined the characteristics of the MPC method which are used throughout this dissertation. An outline of both the continuum flow module, LE-MANS, and the rarefied flow module, MONACO, are provided. The hybrid routines necessary for simulation of nonequilibrium flow with the MPC method, with emphasis on portions of the code that are important for the future modifications to extend the applicability of flows simulated with the MPC method, have been reviewed. A summary of new extensions to the MPC method that are further detailed later in the dissertation, including rotational nonequilibrium, vibrational excitation, and parallelization of the MPC method which enables the extension to full three-dimensional simulations have been outlined.

## CHAPTER IV

### Effects of Rotational Energy Nonequilibrium

For many hypersonic flows, local thermodynamic equilibrium between translational and rotational modes can often be assumed with little physical error. However, for flows that contain regions of collisional nonequilibrium, that the MPC method is designed to simulate, the assumption of local thermodynamic equilibrium between translational and rotational modes is inappropriate, even if the collision number,  $Z_{\text{ROT}}$ , is quite small for gas species of interest. If insufficient collisions occur to maintain collisional (or translational) equilibrium and the number of rotationally inelastic collisions is a fraction of the total number of collisions, rotational nonequilibrium will exist. Often at the edge of a rarefied region, there exists a portion of the flow field that can be considered near collisional equilibrium (such that the velocity distribution function can be described by the Chapman-Enskog expansion), but still exhibits thermal nonequilibrium between translational and rotational energy modes. In order to extend the applicability of the continuum solver, and therefore decrease the computational cost of the MPC method, the capability of modeling rotational relaxation within the CFD solver is included within the MPC method. This chapter describes and compares the models used in both solvers to simulate a separate rotational energy mode which may not be in equilibrium with the translational energy

mode and the relaxation models used to describe the transfer of energy between the translational and rotational energy modes. In order to continue the use of full DSMC simulations as a verification tool, rotational relaxation models must agree between CFD and DSMC modules in near equilibrium regions. This is assessed by comparing zero-dimensional relaxation processes predicted by each flow simulation method. Modifications to the algorithms used to calculate the interface location and transfer information are outlined. The hybrid particle-continuum method is then applied to hypersonic flow over a two-dimensional cylinder at two flow conditions with nominal free stream Knudsen numbers of 0.01 and 0.002, and to axi-symmetric flow over a sting-mounted, planetary probe with a free stream Knudsen number of 0.01. For all three flow conditions, the MPC method is compared with full CFD results and is verified with full DSMC simulations. In addition, limited experimental data available for flow over the planetary probe is used to assess the accuracy of the numerical methods.

## 4.1 Extension of Physical Models

Extension of the mathematical and numerical models required to include rotational nonequilibrium within the MPC method is first discussed. Extension of the Boltzmann equation, its relevance to the development of rotational collision models in DSMC, and an added conservation equation to the single temperature Navier-Stokes equations are outlined.

### 4.1.1 Extension of the Boltzmann Equation

Instead of modeling a single velocity distribution function for the gas, the general Boltzmann equation (as seen in Eq. 2.1) can be extended to include internal, quantized energy by modeling the rate of change of the probability density function,

$f_i(\mathbf{x}, \mathbf{c}, t, E_i)$ , for each quantum state  $i$  as shown in Eq. 4.1.

$$\frac{\partial}{\partial t} [n_i f_i] + c_m \frac{\partial}{\partial x_m} [n_i f_i] = \left\{ \frac{\partial}{\partial t} [n_i f_i] \right\}_{\text{col}} \quad (4.1)$$

Now the collision integral, shown in Eq. 4.2, must include a collision cross section,  $\sigma_{i,j}^{i',j'}$ , that is not only dependent on the velocity, but the initial  $(i, j)$  and final  $(i', j')$  rotational quantum states of the two particles.

$$\left\{ \frac{\partial}{\partial t} [n_i f_i] \right\}_{\text{col}} = \Sigma_{j,i',j'} \int_{-\infty}^{\infty} \int_0^{4\pi} (n_{j'} f_{j'} n_{i'} f_{i'} - n_j f_j n_i f_i) g_{i,j} \sigma_{i,j}^{i',j'} d\Omega d\mathbf{V}_j \quad (4.2)$$

As the two particles collide, either one can move through the four-dimensional velocity and internal energy space, assuming one internal energy mode. This collision cross section determines the rate at which internally elastic and inelastic collisions occur within the flow. Since the quantum step sizes between rotational energy states increase as the quantum number increases [88], pure rotation-rotation energy transfer, where the translational energy remains constant through the collision process, is statistically infrequent, which results in the rotationally inelastic cross section always being modeled with translational energy exchange.

If all collisions are assumed to be internally inelastic, which corresponds to a rotational collision number of unity, and the velocity distribution function can be considered Maxwellian, the flow is in local thermodynamic equilibrium and both translational and internal states can be described with one temperature. Although the exact form of the differential cross section is not known, experimental measurements at typical conditions signify that most collisions can be considered elastic with about 20% of collisions being rotationally inelastic [89].

For most flows of interest, the rotational quantum energy levels are much smaller than the mean rotational energy and the rotational energy can be assumed to be continuous and fully activated with very little loss of physical accuracy. This allows

the triple summation in the collision integral shown in Eq. 4.2 over partner and post-collision rotational states located in the collision term to be converted to a triple integral over the continuous internal energy states which is shown in Eq. 4.3.

$$\left\{ \frac{\partial}{\partial t} [n_i f_i] \right\}_{\text{col}} = \int_0^\infty \int_0^\infty \int_0^\infty \int_{-\infty}^\infty \int_0^{4\pi} (n_{j'} f_{j'} n_{i'} f_{i'} - n_j f_j n_i f_i) g_{i,j} \sigma_{i,j}^{i',j'} d\Omega d\mathbf{V}_j dE_j dE_{i'} dE_{j'} \quad (4.3)$$

Even if the exact form of the differential cross section was known, adding rotational nonequilibrium physics to the Boltzmann equation increases the dimensionality of numerically finding a steady-state, deterministic solution from 6D to 7D for diatomic, symmetric molecules. This significantly increases the cost of obtaining deterministic numerical solutions to the Boltzmann equation.

#### 4.1.2 Rotational Relaxation in DSMC Methods

In a similar manner to how DSMC directly simulates rotationally elastic collisions as described in Section 2.3.2, the DSMC method can also include rotationally inelastic collisions. Physically, the probability of a collision being rotationally inelastic is a ratio of the rotational inelastic cross section to the total collision cross section. Although the exact form of the inelastic cross section is unknown, MONACO assumes that the total cross section, given by the variable hard sphere (VHS) model, is independent of the internal energy content and uses a phenomenological form of the probability of a rotationally inelastic collision that only depends on total collision energy between collision pairs, first proposed by Boyd [73] and shown in Eq. 4.4, which is derived from the rotational collision number of Parker [89].

$$\phi_{\text{ROT}}(\varepsilon_c) = \frac{\left[ 1 + \frac{\pi^{3/2} \Gamma(\zeta+2-\omega)}{2\Gamma(\zeta+3/2-\omega)} \sqrt{\frac{kT_s^*}{\varepsilon_c}} + \frac{\Gamma(\zeta+2-\omega)}{\Gamma(\zeta+1-\omega)} \frac{kT_s^*}{\varepsilon_c} \left( \frac{\pi^2}{4} + \pi \right) \right]}{Z_{\text{ROT},s}^\infty} \quad (4.4)$$

$$\varepsilon_c = \frac{1}{2} \mu g^2 + \varepsilon_{\text{ROT}} \quad (4.5)$$

Here,  $T_s^*$  and  $Z_{\text{ROT},s}^\infty$  correspond to the constants in Parker's macroscopic model,  $\zeta$  is the number of internal degrees of freedom,  $\omega$  is the viscosity temperature exponent,  $k$  is the Boltzmann constant, and  $\varepsilon_c$  is the collision energy defined by Eq. 4.5. Here,  $g$  is the relative velocity between collision partners,  $\mu$  is the reduced mass of the partners, and  $\varepsilon_{\text{ROT}}$  is the available rotational energy in the collision. This form of the inelastic probability is phenomenological and chosen for mathematical convenience to match Parker's continuum model by satisfying Eq. 4.6.

$$\langle P_{\text{ROT},s} \rangle = \frac{1}{Z_{\text{ROT},s}} = \frac{1}{\nu_s \tau_{\text{ROT},s}} = \int_0^\infty \phi_{\text{ROT},s}(\varepsilon_c) f(\varepsilon_c) d\varepsilon_c \quad (4.6)$$

This ensures that the variable probability of rotational energy relaxation can match the macroscopic form of the rotational relaxation given by Parker and shown in Eq. 4.7 when the energy distribution of colliding particles can be considered equilibrium.

$$Z_{\text{ROT},s} = \frac{Z_{\text{ROT},s}^\infty}{1 + \frac{\pi^{3/2}}{2} \left( \frac{T_s^*}{T_{\text{TRA}}} \right)^{1/2} + \left( \frac{\pi^2}{4} + \pi \right) \left( \frac{T_s^*}{T_{\text{TRA}}} \right)} \quad (4.7)$$

Lumpkin et al. [90] found that the definitions of continuum and particle collision rates differ by a factor given by Eq. 4.8 where  $\zeta_{\text{int,tra}}$  is the number of internal degrees of freedom based on the translational temperature and  $\omega$  is the VHS temperature exponent.

$$\tau_{\text{int}}^{\text{DSMC}} = \frac{\tau_{\text{int}}^{\text{CFD}}}{1 + \frac{\zeta_{\text{int,tra}}}{4-2\omega}} \quad (4.8)$$

In order to maintain consistency between microscopic and macroscopic models, the suggested factor is used giving the final variable probability shown in Eq. 4.9.

$$\begin{aligned} \phi_{\text{ROT,FIN}}(\varepsilon_c) &= \\ \left[ \frac{1 + \frac{\zeta_{\text{int,tra}}}{4-2\omega}}{Z_{\text{ROT},s}^\infty} \right] \left[ 1 + \frac{\pi^{3/2} \Gamma(\zeta + 2 - \omega)}{2 \Gamma(\zeta + 3/2 - \omega)} \sqrt{\frac{k T_s^*}{\varepsilon_c}} + \frac{\Gamma(\zeta + 2 - \omega)}{\Gamma(\zeta + 1 - \omega)} \frac{k T_s^*}{\varepsilon_c} \left( \frac{\pi^2}{4} + \pi \right) \right] \end{aligned} \quad (4.9)$$

This probability is used in an acceptance-rejection algorithm for each DSMC collision pair to determine if the pair undergoes rotation-translation relaxation. If a collision pair is selected, the Larsen-Borgnakke [91] method is used to distribute energy between available translational and rotational energy modes.

#### 4.1.3 Rotational Relaxation in Continuum Methods

Derivation of a separate rotational energy equation follows the procedure of Chang and Uhlenbeck which is listed in Ref. [15]. The local Maxwell-Boltzmann probability density function, shown in Eq. 4.10, is now a function of both a translational temperature,  $T_{\text{TRA}}$ , and a rotational temperature,  $T_{\text{ROT}}$ , which may or may not be the same.

$$f^0 = \left( \frac{1}{2\pi k T_{\text{TRA}}} \right)^{3/2} \frac{1}{k T_{\text{ROT}}} \exp \left( \frac{-mc^2}{2k T_{\text{TRA}}} - \frac{\varepsilon_{\text{ROT}}}{k T_{\text{ROT}}} \right) \quad (4.10)$$

$$\varphi_1 = -\frac{1}{n} \left[ \sqrt{\frac{2k T_{\text{TRA}}}{m}} A_{\text{TRA},i} \frac{\partial \ln T_{\text{TRA}}}{\partial x_i} - \sqrt{\frac{2k T_{\text{TRA}}}{m}} A_{\text{ROT},i} \frac{\partial \ln T_{\text{ROT}}}{\partial x_i} - B_{i,j} \frac{\partial c_i}{\partial x_j} \right] \quad (4.11)$$

$$f(\mathbf{c}, \varepsilon_{\text{ROT}}) d\mathbf{c} d\varepsilon_{\text{ROT}} = f^0(\mathbf{c}, \varepsilon_{\text{ROT}}) [1 + \varphi_1] d\mathbf{c} d\varepsilon_{\text{ROT}}$$

Now, six macroscopic variables define the state of the gas at near collisional equilibrium conditions, but there are only five ( $m$ ,  $m\mathbf{c}$ , and  $mc^2/2 + \varepsilon_{\text{INT}}$ ) collision invariant terms. Therefore, the additional equation needed to represent the state of the gas requires a model of the collision integral term in the Maxwell-Boltzmann equation. An additional equation can be derived by setting the quantity of interest in Maxwell's equation of change to the rotational energy,  $\varepsilon_{\text{ROT}}$ , which results in Eq. 4.12 with the collision term now only signifying rotationally inelastic collisions.

$$\frac{\partial}{\partial t} [n \bar{\varepsilon}_{\text{ROT}}] + \frac{\partial}{\partial x_j} [n \bar{c}_j \bar{\varepsilon}_{\text{ROT}}] = \Delta [\varepsilon_{\text{ROT}}]_{\text{Inel}} \quad (4.12)$$

Here, the spatial derivative results in a mean flow term and a fluctuation term that can be modeled with an internal heat flux term and defining a specific internal

energy as  $e_{\text{ROT}} = \overline{\varepsilon_{\text{ROT}}/m}$  results in Eq. 4.13.

$$\frac{\partial}{\partial t} [\rho e_{\text{ROT}}] + \frac{\partial}{\partial x_j} [\rho u_j e_{\text{ROT}} + q_{\text{ROT},j}] = \Delta [\varepsilon_{\text{ROT}}]_{\text{inel}} \quad (4.13)$$

Physically, the rotationally inelastic collisions involve two forms of energy transfer: transfer between rotational energies and transfer between translational and rotational energy modes. As previously stated, pure rotation-rotation energy transfer is very rare due to the rotational energy difference between levels varying as the rotational energy of the particle increases. Assuming small departures from thermal equilibrium, the rate of transfer of energy between translational and rotational modes due to collisions can be modeled as Eq. 4.14 [15] where the rotational relaxation time,  $\tau_{\text{ROT}}$ , is dependent on the inelastic cross section and macroscopic parameters.

$$\Delta [\varepsilon_{\text{ROT}}]_{\text{inel}} \approx \rho \frac{e_{\text{ROT}}^* - e_{\text{ROT}}}{\tau_{\text{ROT}}} \quad (4.14)$$

Again using Parker's model [89] for the rotational collision number,  $Z_{\text{ROT}}$ , the rotational relaxation time can be evaluated using Eq. 4.15 where  $\tau_{\text{col}}$  is the mean time between collisions.

$$\tau_{\text{ROT}} = Z_{\text{ROT}} \tau_{\text{col}} \quad (4.15)$$

The mean collision time is the inverse of the mean collision frequency,  $\nu$ , which is straight forward to compute for a gas modeled using the VHS cross section and macroscopic variables such as translational temperature and number density as shown in Eq. 4.16. Here  $i$  ranges through the number of species,  $s$  is the species of interest,  $d_{\text{ref}}$  is the reference diameter,  $n$  is the number density,  $\mu^*$  is the viscosity at the reference temperature,  $T_{\text{ref}}$ , and  $\omega$  is the viscosity temperature exponent.

$$\nu_s = \frac{1}{\tau_{\text{coll},s}} = \sum_i \left( n_i d_{\text{ref},s,i}^2 \left( \frac{8\pi k T_{\text{ref},i}}{\mu_{s,i}^*} \right)^{\frac{1}{2}} \left( \frac{T_{\text{TRA}}}{T_{\text{ref},i}} \right)^{1-\omega_i} \right) \quad (4.16)$$

This results in a final equation for the rate of change of rotational energy shown in Eq. 4.17 which, coupled with the time rate of change of density, linear momentum, total energy, and an equation of state, provides a sufficient number of equations to describe the gas state within each control volume.

$$\frac{\partial \rho e_{\text{ROT}}}{\partial t} + \nabla \cdot (\rho e_{\text{ROT}} \vec{u}) = -\nabla \cdot (\vec{q}_{\text{rot}}) + \rho \frac{e_{\text{ROT}}^* - e_{\text{ROT}}}{\tau_{\text{ROT}}} \quad (4.17)$$

#### 4.1.4 Comparison of Rotational Relaxation Models

In order to use full DSMC as a verification tool of the MPC method, specifically for the information transfer between the two methods and placement of the interface locations between continuum and rarefied flow modules, models used to approximate the physical processes in each flow module must agree at the continuum limit. In other words, if both CFD and DSMC flow modules simulate a physical process in a region of the flow that is entirely continuum, they must remain consistent. If this does not happen, differences in the prediction of the continuum region of the flow field could be attributed to either inconsistencies between the two models or discrepancies in the implementation of the MPC method, but the exact cause can not be determined. In order to ensure that the models used to approximate rotational relaxation in each flow module are consistent, adiabatic rotational relaxation processes are simulated using both MONACO and LeMANS.

Figure 4.1 compares one such case of the evolution of rotational and translational temperatures as they approach equilibrium after being initialized to different temperatures. Despite differences in how relaxation is modeled, the two models remain consistent at the continuum limit which results in excellent agreement of macroscopic quantities.

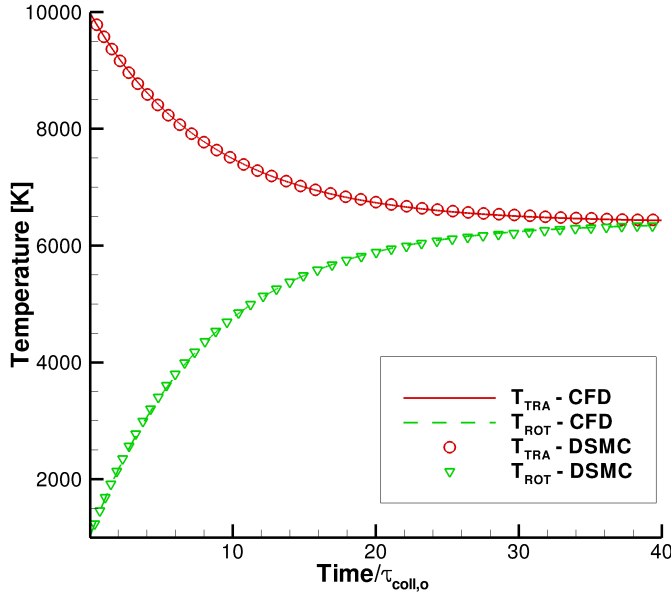


Figure 4.1: Comparison of an adiabatic rotational-translational relaxation process predicted by DSMC and CFD

## 4.2 Modifications to the MPC Method

This subsection outlines the required changes to the MPC method to ensure consistent and physically accurate simulation of flows that can be in rotational nonequilibrium in parts or all of the flow field.

### 4.2.1 Continuum Breakdown and Interface Location

As mentioned in Sec. 3.2.1, previous work with simulation of perfect gas physics indicates that the gradient length, local Knudsen number based on density, speed, and translational temperature with a cutoff value of 0.05 adequately predicts the onset of continuum breakdown and regions of the flow where DSMC should be used [80, 81, 66]. Since rotational temperature is also now a quantity of interest, the gradient length Knudsen number based on rotational temperature with the same breakdown parameter value is included as well.

Now, in addition to ensuring that the velocity distribution function is near equilibrium at the interface, the rotational energy distribution must also be near equilibrium. This is required so that the distribution of internal energies assigned to particles in DSMC boundary cells and relaxation rates calculated in both flow solvers remain consistent. In some regions of the flow, the velocity distribution functions may be very near equilibrium, while the rotational energy distribution function requires more collisions to reach equilibrium. To ensure that the rotational energy distribution function is near equilibrium, an additional breakdown parameter must be applied that characterizes the degree that the rotational energy distribution function departs from equilibrium. The primary cause of the departure of the rotational energy distribution function from Boltzmann is in regions where the flow is highly collisional and strong thermal relaxation takes place, such as the flow directly behind the bow shock in hypersonic flow, where the density and translational energy are large, but rotational relaxation is still significant. To characterize this process, the magnitude of the energy transferred by rotation-translation relaxation processes is compared to the total amount of energy stored in the rotational energy mode which results in a thermal breakdown parameter seen in Eq. 4.18. This added breakdown parameter is of the same form suggested by Schwartzenruber et al. as described in Ref. [66] and has been used in MPC simulations with a single temperature continuum module. However, it is further relaxed to take into account the capability of calculating rotational relaxation processes in the continuum solver and an absolute value is employed to label both heating *and* cooling of the rotational energy mode.

$$Kn_{ROT-NEQ} = \frac{|T_{TRA} - T_{ROT}|}{2 T_{ROT}} \quad (4.18)$$

Figure 4.2 compares translational temperature predictions of the MPC method

with (top) and without (bottom) the rotational nonequilibrium switch activated along with full DSMC results.

Without the nonequilibrium switch, the interface location between CFD and DSMC modules is located very near the shock. Since CFD does not contain the physical accuracy required to model this portion of the rotational relaxation process as the rotational energy distribution function is highly non-Boltzmann in this region, the post shock temperatures are over predicted compared to full DSMC. With an added rotational nonequilibrium breakdown parameter, the portion of the flow field modeled with the continuum solver is slightly decreased to only regions where the continuum solver is physically valid and agreement between MPC and full DSMC results is greatly improved. Velocity and rotational energy distribution functions are sampled from the full DSMC solution at locations denoted as **A** and **B** in Fig. 4.2 along the edge of the interface location predicted by each MPC simulation. Figures 4.3(a) and 4.3(b), respectively, compare the velocity distribution functions and rotational energy distribution function sampled from DSMC with equilibrium theory at point **A**. The procedures used to generate these probability density functions are described in Appendix B. Here, the equilibrium velocity distribution function is given by Eq. 2.3, while the equilibrium rotational energy probability density function, assuming a continuous energy distribution that is fully excited, is given by Eq. 4.19 where  $\varepsilon_{\text{ROT}}$  is the particle rotational energy,  $T_{\text{ROT}}$  is the rotational temperature which is calculated using Eq. 4.20, and  $k$  is the Boltzmann constant.

$$f(\varepsilon_{\text{ROT}}) d\varepsilon_{\text{ROT}} = \frac{1}{kT_{\text{ROT}}} \exp\left(\frac{-\varepsilon_{\text{ROT}}}{kT_{\text{ROT}}}\right) d\varepsilon_{\text{ROT}} \quad (4.19)$$

$$T_{\text{ROT}} = \frac{\langle \varepsilon_{\text{ROT}} \rangle}{k} \quad (4.20)$$

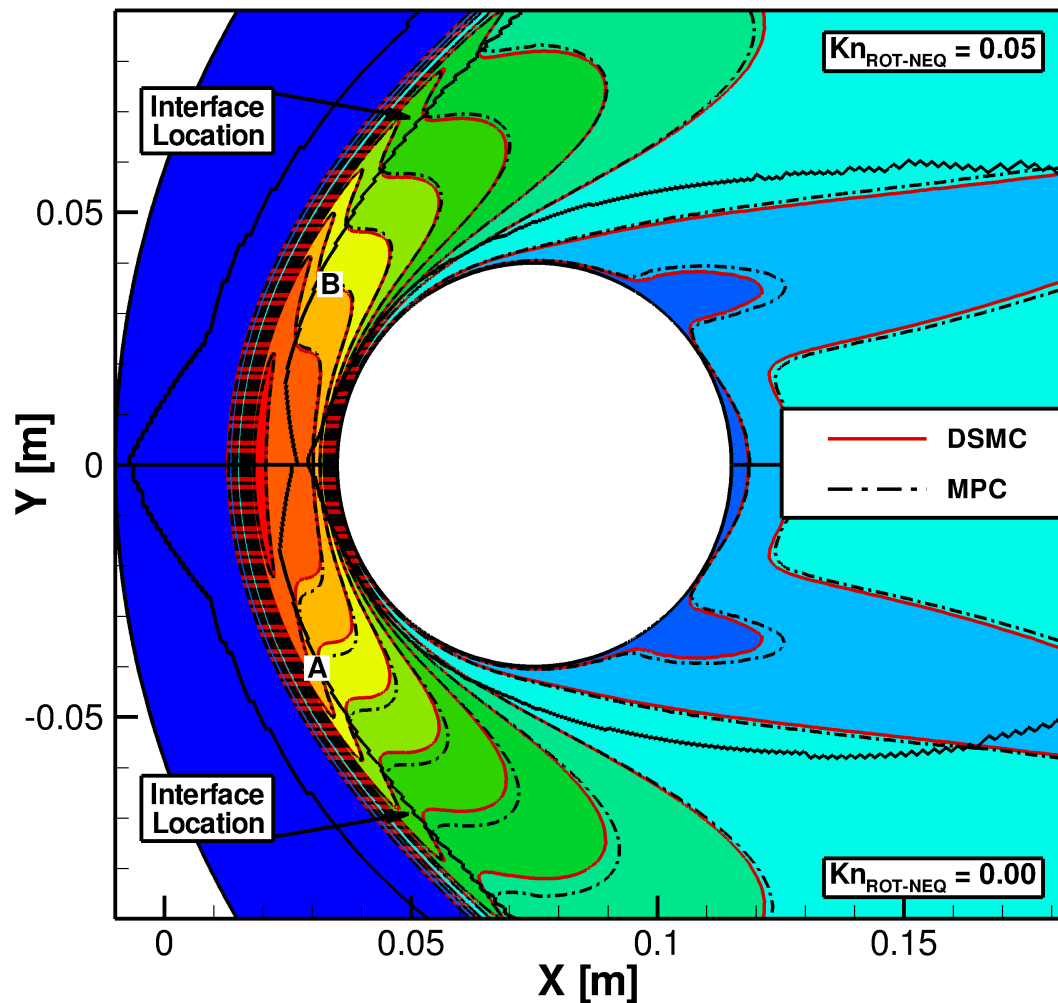
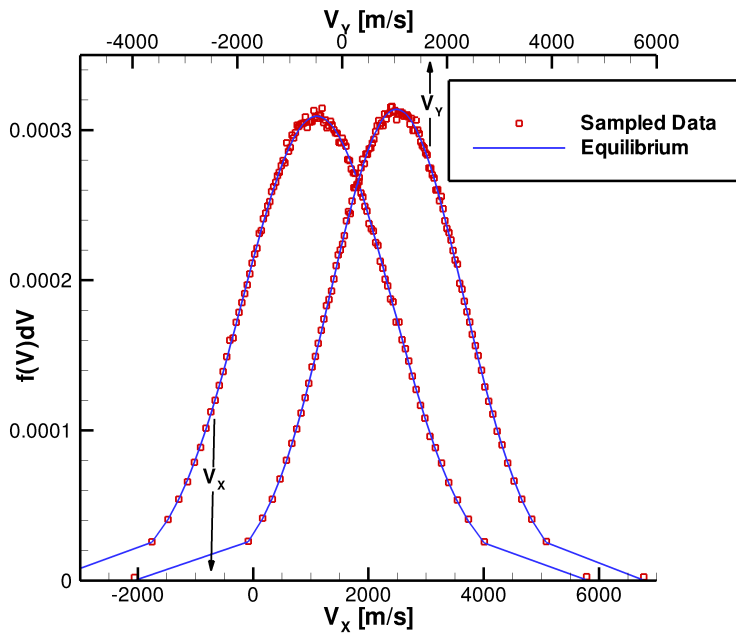
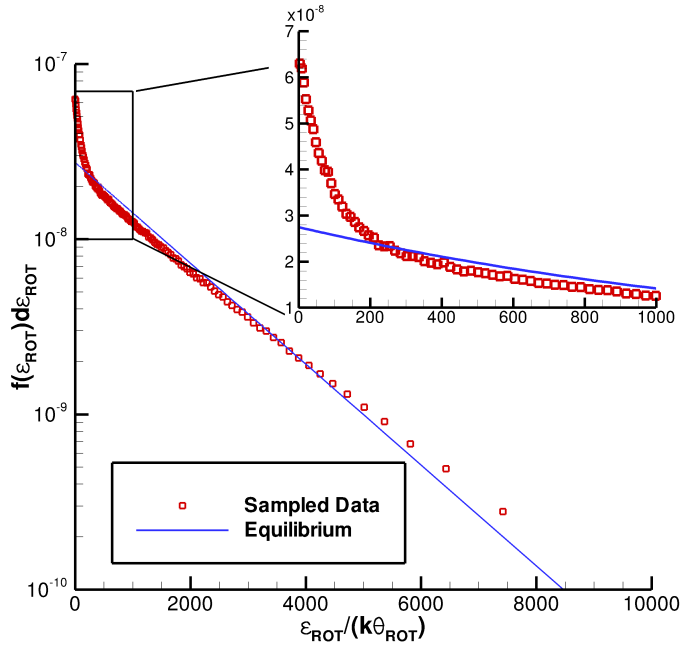


Figure 4.2: Comparison of translational temperatures predicted by the MPC method with (top) and without (bottom) the rotational nonequilibrium breakdown parameter compared with full DSMC computation of Mach 12 flow over a cylinder with a global Knudsen number of 0.01



(a) Velocity



(b) Rotational Energy

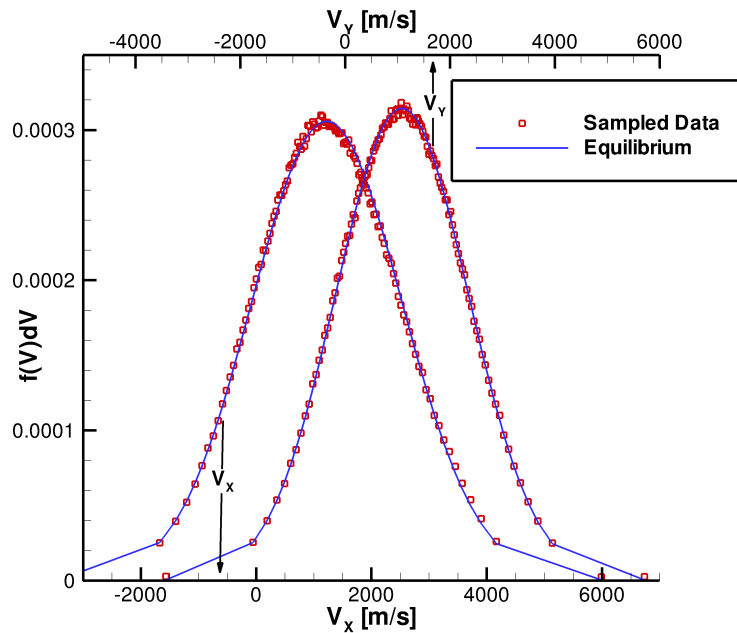
Figure 4.3: Comparison of probability density functions predicted by DSMC and equilibrium theory at point A shown in Figure 4.2.

Although the predicted velocity probability density functions are in excellent agreement with equilibrium theory, the rotational energy distribution function significantly differs from equilibrium. In contrast, Figs. 4.4(a) and 4.4(b) compare the velocity and rotational energy distribution functions, respectively, at the continuum interface location computed with the added breakdown parameter at point **B**. At this point in the flow, both the velocity *and* rotational energy probability density functions are in much better agreement with the equilibrium description and the models used in the continuum solver are valid. Since the equilibrium rotational energy distribution function is calculated based on the average rotational energy, comparison of higher order moments, such as the variance, calculated from sampled data and the equilibrium distribution can be used as a measure of degree of rotational nonequilibrium. For rotational energy, the variance of the Boltzmann energy probability density function is shown in Eq. 4.21.

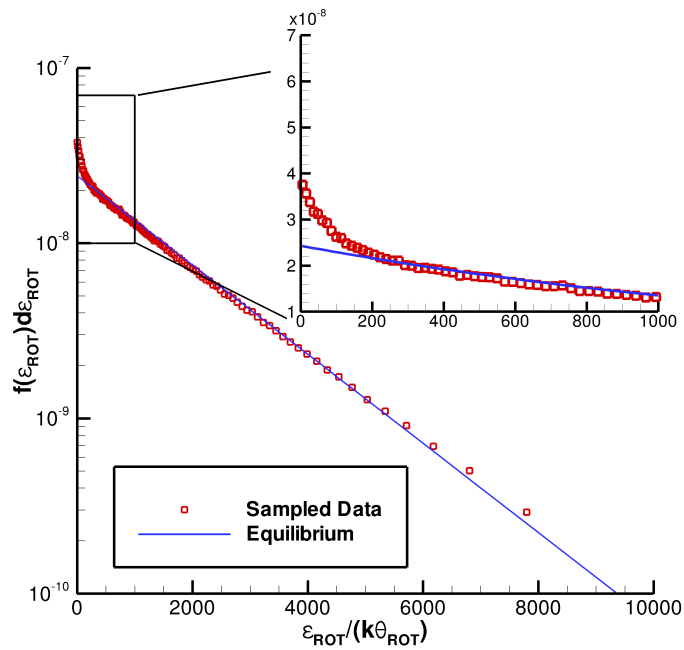
$$s^2 = (kT_{\text{ROT}})^2 \quad (4.21)$$

At point **A**, the sampled variance of the rotational energy probability density function differs by nearly 25% from equilibrium, while the sampled variance differs by less than 10% from the equilibrium value at point **B**.

By applying a breakdown parameter that ensures that the rotational energy distribution function is near equilibrium, internal energies assigned to particles in DSMC boundary cells are in excellent agreement with the rotational energies predicted in a full DSMC simulation method. This ensures that the energies assigned to particles generated in the MPC method along the rarefied-continuum interface are consistent with the full DSMC simulation. This results in a final breakdown parameter shown



(a) Velocity



(b) Rotational Energy

Figure 4.4: Comparison of probability density functions predicted by DSMC and equilibrium theory at point **B** shown in Figure 4.2.

in Eq. 4.22.

$$Br = \max(Kn_{GL-\rho}, Kn_{GL-T_{TRA}}, Kn_{GL-T_{ROT}}, Kn_{GL-|V|}, Kn_{ROT-NEQ}) \quad (4.22)$$

#### 4.2.2 Information Transfer

As with the other primitive values of  $\rho$ ,  $\mathbf{u}$ , and  $T_{TRA}$ , state-based coupling is used to transfer the evolution of rotational temperature between CFD and DSMC flow modules. Now instead of using the combined translational-rotational temperature from the continuum solver to assign rotational energies, the separate rotational temperature is used, along with the inverse transform sampling of the Boltzmann rotational energy probability density function which is shown in Eq. 4.19 to assign the rotational energies to DSMC particles. Rotational temperatures are calculated at each time step from the DSMC particle rotational energy using Eq. 4.23 and the subrelaxation average which is shown in Eq. 3.18 is applied to the rotational temperature.

$$T_{ROT} = \frac{1}{kN_{real}} \sum_{rc=1}^{N_{rc}} \sum_{P_{rc}=1}^{N_{P_{rc}}} W_{rc} \varepsilon_{ROT, P_{rc}} \quad (4.23)$$

### 4.3 Verification and Validation of the MPC Method

The goal of the MPC method is to be able to reproduce full DSMC results to within 5% at a fraction of the computational cost. In order to verify the implementation of modeling a separate rotational energy mode within the MPC method, simulation of Mach 12 flow over a cylinder with free stream global Knudsen numbers of 0.01 and 0.002 are performed with the MPC method. The MPC results are compared with full CFD predictions and verified with full DSMC predictions. In addition, simulations of Mach 20 flow over a planetary probe with a global Knudsen number of 0.01 are performed with DSMC, CFD, and the MPC method. Again, the

MPC method is verified with full DSMC simulation results, and all three methods are compared to available experimental measurements.

### 4.3.1 Flows Over a 2D Cylinder

#### Flow Conditions

The implementation of rotational relaxation in the MPC method is evaluated with simulation of hypersonic flow of molecular nitrogen about a cylinder with a free stream Mach number of 12 at two Knudsen numbers. The free stream temperature is  $T_{\text{TRA},\infty} = T_{\text{ROT},\infty} = 217.5 \text{ K}$  at a free stream velocity of  $U_\infty = 3,608 \text{ m s}^{-1}$ . The cylinder wall temperature is set to  $T_w = 1,000 \text{ K}$  with full diffuse reflection in DSMC simulations and a no-slip, isothermal condition in CFD simulations. The free stream density is set to two different values of  $\rho_\infty = 7.48 \times 10^{-5} \text{ kg m}^{-3}$  and  $\rho_\infty = 3.74 \times 10^{-4} \text{ kg m}^{-3}$  which correspond to global Knudsen numbers based on cylinder diameter of  $Kn_\infty = 0.01$  and  $Kn_\infty = 0.002$  and are also referred as case **CM12K01** and **CM12K02**, respectively. The diameter of the cylinder simulated is  $d = 8 \text{ cm}$ . A constant time-step of  $1.5 \times 10^{-8} \text{ s}$  and  $4.0 \times 10^{-9} \text{ s}$  are used in the DSMC method at global Knudsen numbers of  $Kn_\infty = 0.01$  and  $Kn_\infty = 0.002$ , respectively, while a maximum CFL number of 25 is used in all CFD simulations.

Figure 4.5 shows the final interface locations between rarefied and continuum solvers for the two cylinder flow conditions used to verify the implementation of the rotational relaxation models in the MPC method. For flow with a global Knudsen number of 0.01, a large portion of the flow field, such as the thick bow shock, boundary layer, and wake region, is rarefied. In contrast, only the near wake and thin boundary layer are rarefied at the lower Knudsen number. Even though the interior of the bow shock is highly nonequilibrium at any density, previous work [66] has shown that using DSMC in this region is not required for accurate prediction of flow

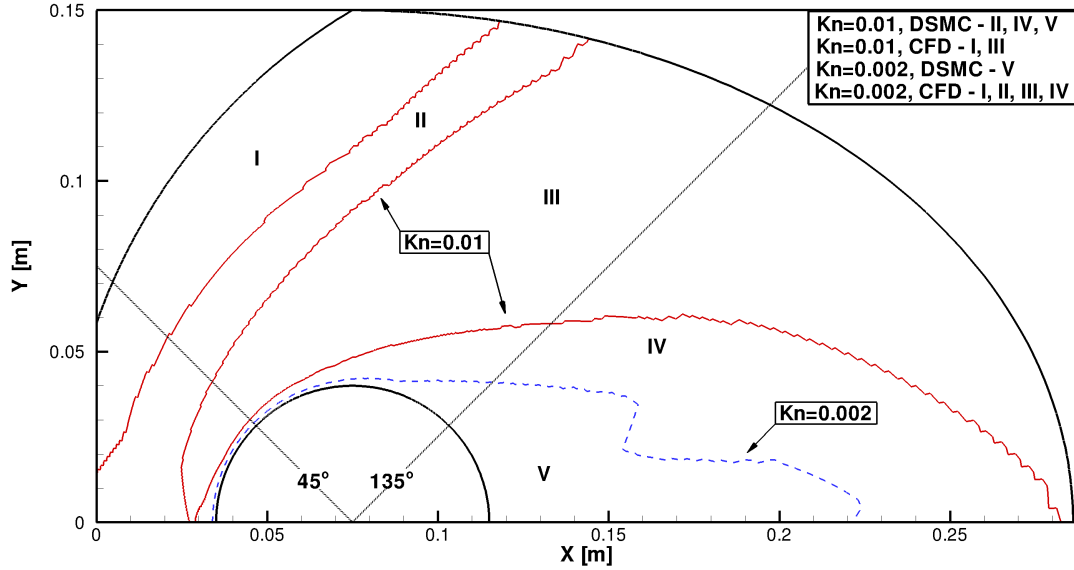


Figure 4.5: Comparison of the final continuum-rarefied interface locations for Mach 12 flow over a cylinder at global Knudsen numbers of 0.002 and 0.01.

field properties behind the shock if the nonequilibrium region due to the shock is completely disconnected from the rarefied region due to the boundary layer, so the MPC simulation does not label this region as a DSMC region. This is performed in the code by using the gradient length Knudsen number based on pressure, shown in Eq. 4.24, as a shock detector where  $\lambda$  is the local mean free path and  $p$  is the local pressure.

$$Kn_{GL-P} = \lambda \frac{\nabla p}{p} \quad (4.24)$$

### Flow Field Properties

Figure 4.6 qualitatively compares the translational temperature contours calculated using full DSMC, full CFD, and the MPC method along with the interface location between the DSMC and CFD modules for flow over a cylinder with a global Knudsen number of 0.01. Overall, the MPC method is able to reproduce full DSMC results while limiting the DSMC computation to areas that are rarefied, such as the

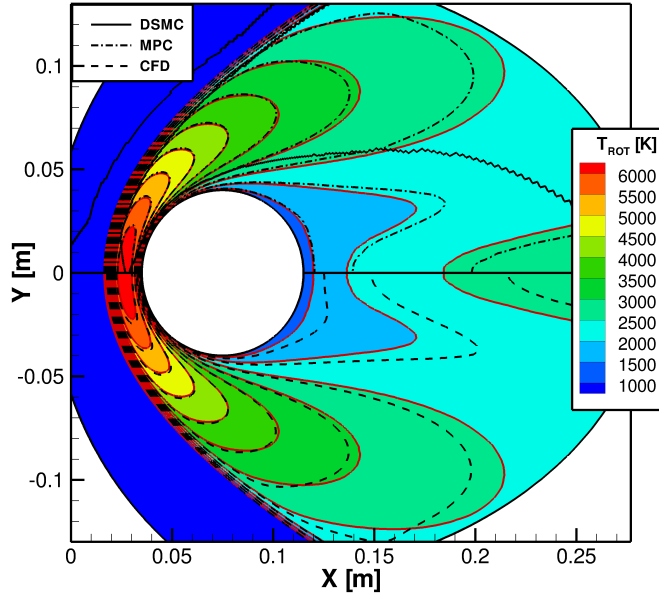


Figure 4.6: Comparison of translational temperature contours predicted by DSMC, CFD, and the MPC method for case **CM12K01**

diffuse shock, boundary layer, and near wake region. Even in regions of the flow where the continuum-based CFD module is used, the MPC method has improved the agreement with full DSMC over full CFD. This is because the DSMC module has shifted the solution and provides an improved boundary condition to the CFD module. The largest discrepancy between full DSMC and the MPC results, which occurs far away from the body, lies below 4%. Figure 4.7 compares the rotational temperature contours predicted by DSMC, CFD, and the MPC method. Again, agreement is very good with the largest difference of less than 3%, occurring far away from the body.

Figures 4.8 and 4.9, respectively, compare the translational and rotational temperature contours predicted by DSMC, CFD, and the MPC method for the near continuum case with a global Knudsen number of 0.002. The largest discrepancy of

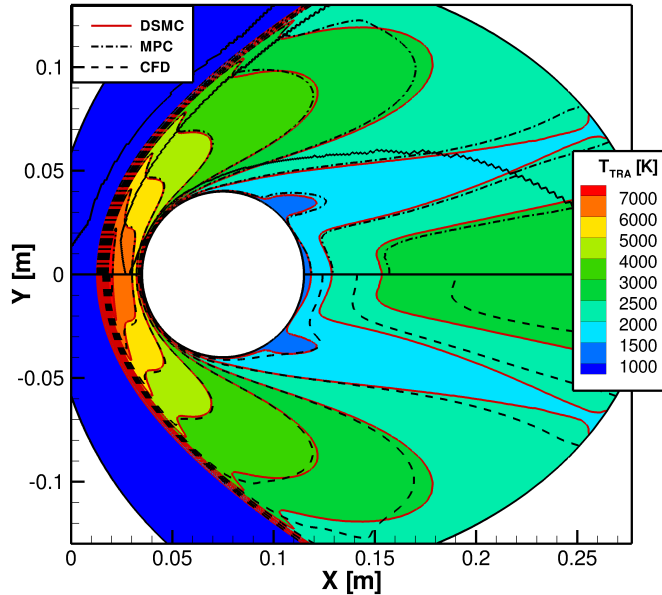


Figure 4.7: Comparison of rotational temperature contours predicted by DSMC, CFD, and the MPC method for case **CM12K01**

14% is located in the shock interior, where the CFD module is used despite the flow being highly nonequilibrium. Differences between MPC and DSMC results in the far wake region, which are located entirely downstream of the body in supersonic flow, remain within 8% for translational temperature and 5% for rotational temperature. Previous studies [66, 5] and the proceeding subsection show that these differences in the shock structure and far wake have very little effect on the prediction of surface quantities. In addition, the MPC results remain within 2% of full DSMC results throughout the rest of the shock layer and near wake region, which directly improves agreement of surface predictions made by the MPC method with full DSMC over full CFD.

Macroscopic quantities are extracted along two lines (shown in Fig. 4.5) located at  $45^\circ$  and  $135^\circ$  from the stagnation streamline. Figure 4.10 shows the predictions

of translational temperature, rotational temperature, and mass density along a  $45^\circ$  extraction line for flow with a global Knudsen number of 0.01. There is very good agreement between full DSMC and the MPC method along the entire extraction line. Especially in highly nonequilibrium regions where large disagreement between full CFD and full DSMC is observed, the difference between MPC and DSMC results is nearly indistinguishable. Even in regions where the CFD module is used, the MPC method has improved agreement with full DSMC compared to the initial full CFD solution. Figure 4.11 shows the comparison of flow variables along the  $135^\circ$  extraction line labeled in Fig. 4.5. In general, full DSMC and CFD are in close agreement along most of the extraction line and the MPC method maintains this same level of agreement. However, near the body, full DSMC and CFD are not in good agreement, while the MPC solution remains in excellent agreement with the full DSMC solution. This improvement near the body has a direct effect on predicted surface property agreement with full DSMC which will be shown in the proceeding subsection. Figure 4.12 compares the variation of macroscopic quantities predicted by DSMC, CFD, and the MPC method along a  $45^\circ$  extraction line for the  $Kn_\infty = 0.002$  flow condition. At this flow condition, the shock was simulated using CFD in the MPC simulation. Although there are some disagreements in shock structure with the full DSMC solution, all three methods are in very good agreement from the post shock condition to midway through the thermal boundary layer. Since the CFD module does not accurately model the natural slip at this condition, full DSMC and CFD are not in agreement in the near wall region. However, the cells very near to the surface are automatically labeled as DSMC cells with the breakdown parameter and the MPC results are able to reproduce full DSMC throughout the entire boundary layer. Figure 4.13 shows the comparison of macroscopic quantities

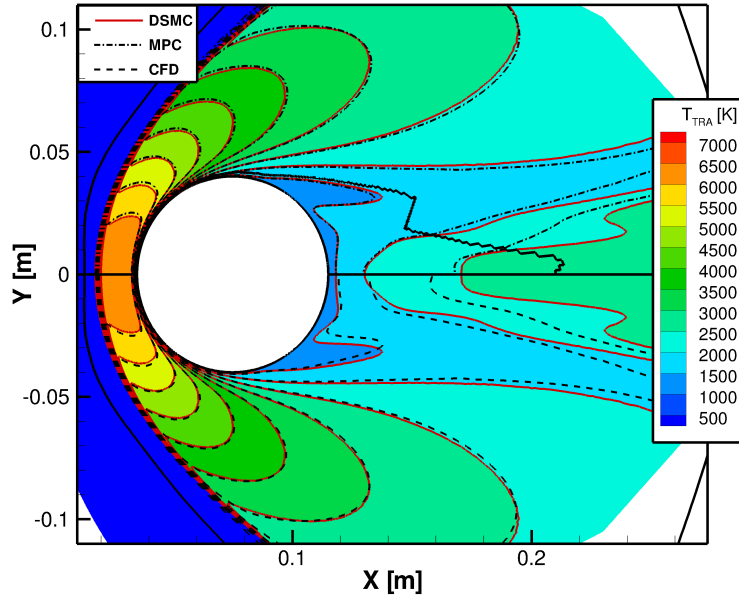


Figure 4.8: Comparison of translational temperature contours predicted by DSMC, CFD, and the MPC for case **CM12K002**

along the  $135^\circ$  extraction line. As in the higher Knudsen number case, both CFD and DSMC are in very good agreement far away from the body, and the MPC method maintains this level of agreement. However, near the wall, where the flow is highly nonequilibrium, full DSMC and CFD are in poor agreement while the MPC method maintains excellent agreement with the full DSMC results.

## Surface Properties

For many hypersonic flow problems of interest, accurate prediction of surface properties has a strong impact on vehicle design. Predictions of heat transfer, shear stress, and pressure from full DSMC, full CFD, and the MPC method are compared. Equations 4.25, 4.26, and 4.27, respectively, show the definitions of the surface pressure, shear stress, and heat transfer coefficient used to compare the surface properties predicted by the simulation methods where  $p$  is the pressure at the wall,  $p_\infty$  is the

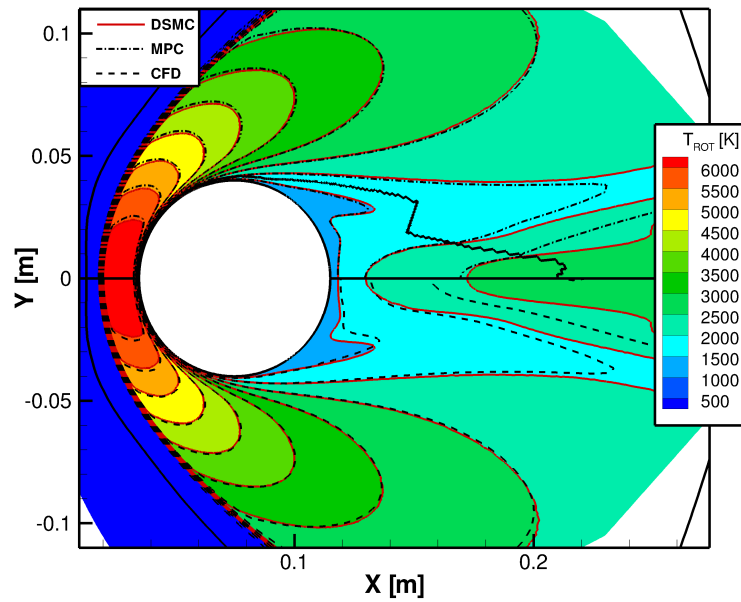


Figure 4.9: Comparison of rotational temperature contours predicted by DSMC, CFD, and the MPC for case **CM12K002**

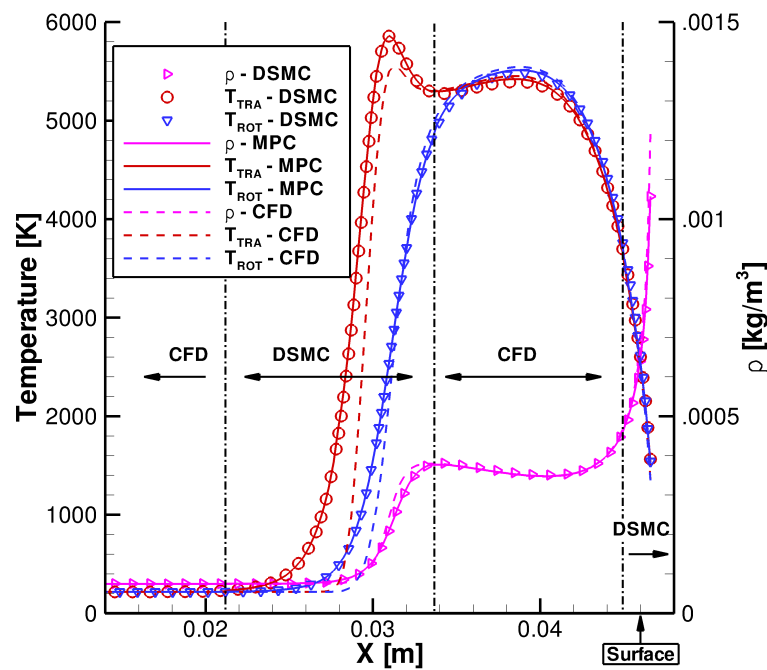


Figure 4.10: Comparison of temperatures and density along a 45° extraction line for case **CM12K01**

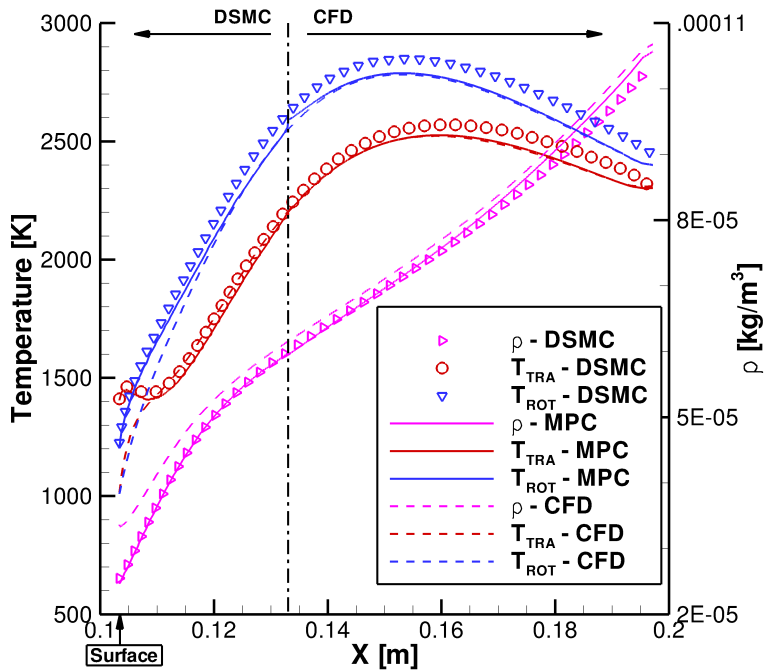


Figure 4.11: Comparison of temperatures and density along a  $135^\circ$  extraction line for case **CM12K01**

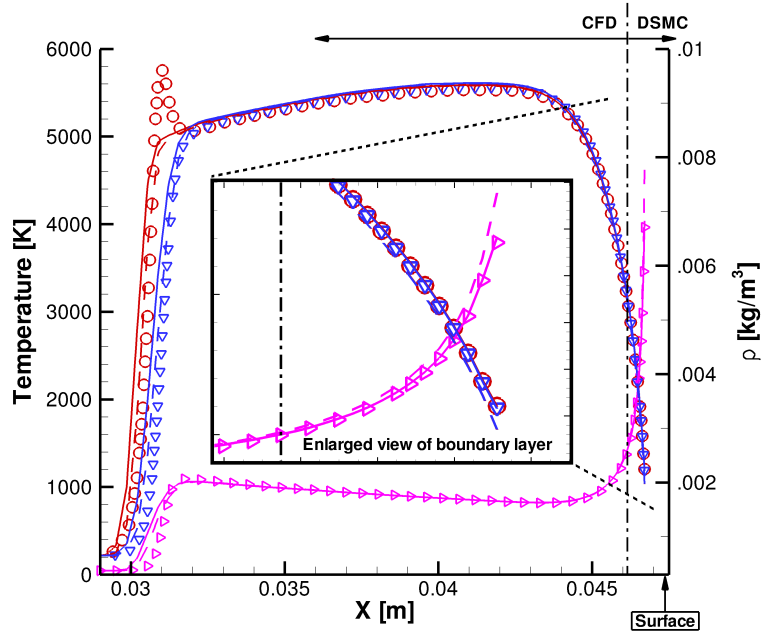


Figure 4.12: Comparison of temperatures and density along a  $45^\circ$  extraction line for case **CM12K002**

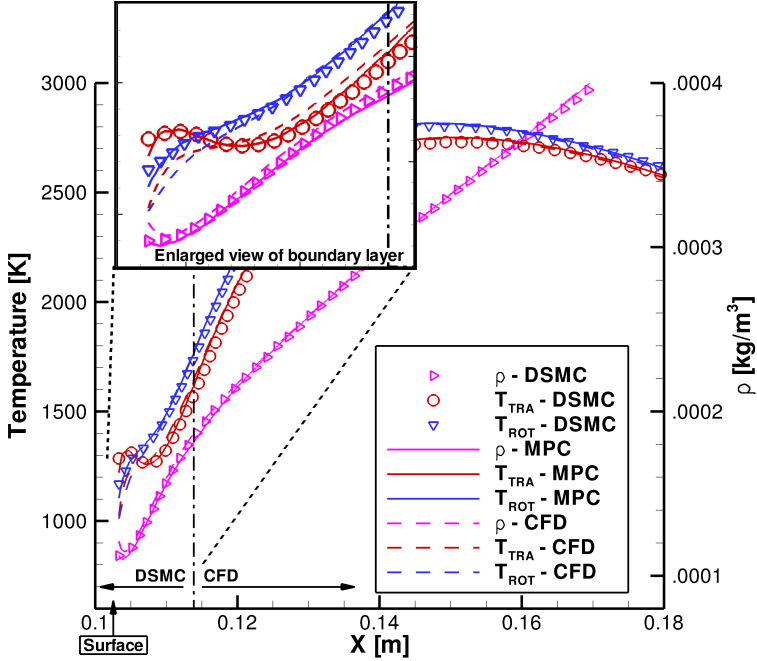


Figure 4.13: Comparison of temperatures and density along a 135° extraction line for case **CM12K002**

free stream pressure,  $\tau$  is the shear stress at the wall,  $q$  is the heat transfer to the wall,  $\rho_\infty$  is the free stream density, and  $u_\infty$  is the free stream velocity.

$$C_p = \frac{p - p_\infty}{\frac{1}{2}\rho_\infty u_\infty^2} \quad (4.25)$$

$$C_\tau = \frac{\tau}{\frac{1}{2}\rho_\infty u_\infty^2} \quad (4.26)$$

$$C_h = \frac{q}{\frac{1}{2}\rho_\infty u_\infty^3} \quad (4.27)$$

Figure 4.14 compares the surface pressure and heat transfer coefficient on the cylinder surface predicted by DSMC, CFD, and the MPC method for case **CM12K01**. All three methods remain within 5% of each other in the fore body region while the full CFD solution deviates from the full DSMC and MPC results as the flow expands around the cylinder. The largest difference between DSMC and CFD is located in the after body of the cylinder where CFD over predicts the surface pressure and

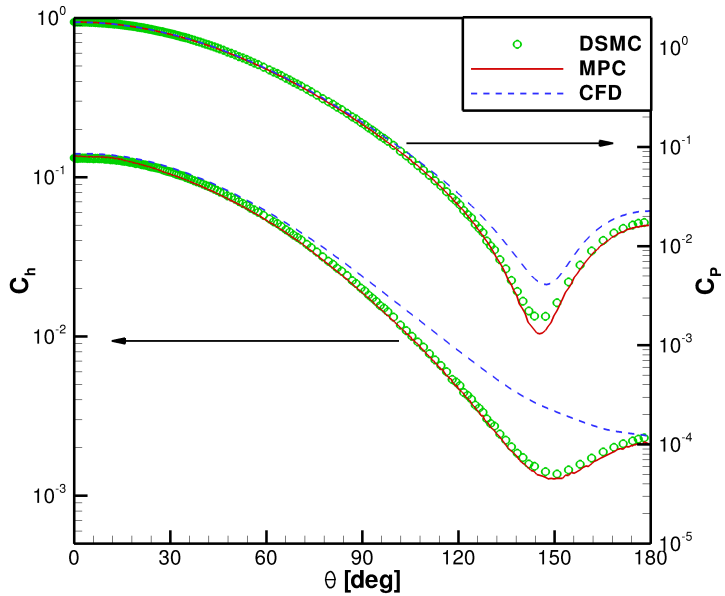


Figure 4.14: Comparison of surface quantities about the cylinder predicted by DSMC, CFD, and the MPC method for case **CM12K01**

heat transfer by over 200%. In contrast, the MPC method remains in very good agreement with DSMC along the entire cylinder body. Figure 4.15 compares the shear stress at the surface of the cylinder predicted by DSMC, CFD, and the MPC method for case **CM12K01**. Again, all three methods are in very good agreement along the fore body, but full DSMC and CFD begin to differ as the flow expands around the cylinder and nonequilibrium effects become significant. In addition, the points where the shear stress goes to zero can be used to compare the relative size of the recirculation zone in the near wake region. Full CFD over predicts the size of the recirculation zone by 32% relative to full DSMC, while the MPC method predicts a recirculation zone that differs from full DSMC by only 0.7%.

Figure 4.16 shows the surface pressure and heat transfer coefficient predicted by DSMC, CFD, and the MPC method for case **CM12K002**. For this higher density flow, full CFD remains in agreement with both DSMC and the MPC results along a

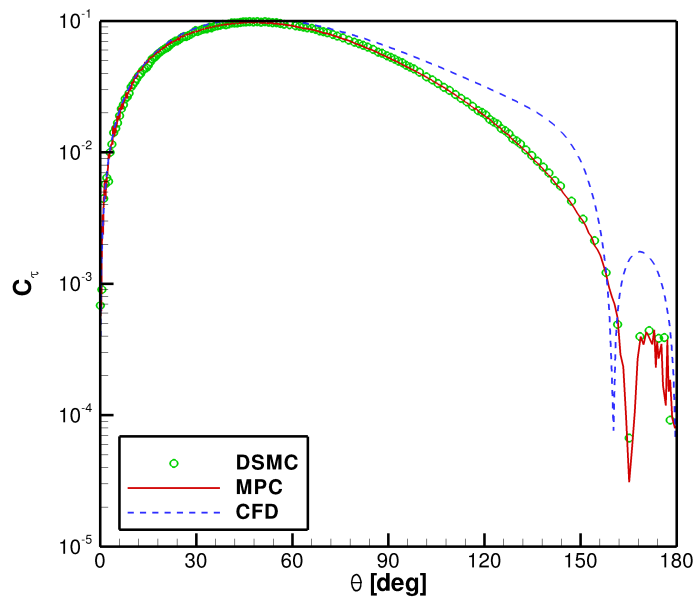


Figure 4.15: Comparison of surface quantities about the cylinder predicted by DSMC, CFD, and the MPC method for case **CM12K01**

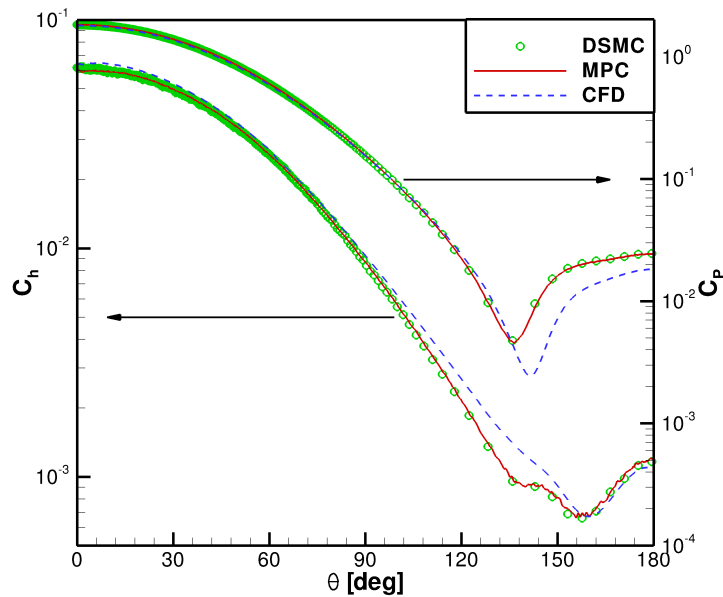


Figure 4.16: Comparison of surface quantities about the cylinder predicted by DSMC, CFD, and the MPC method for case **CM12K002**

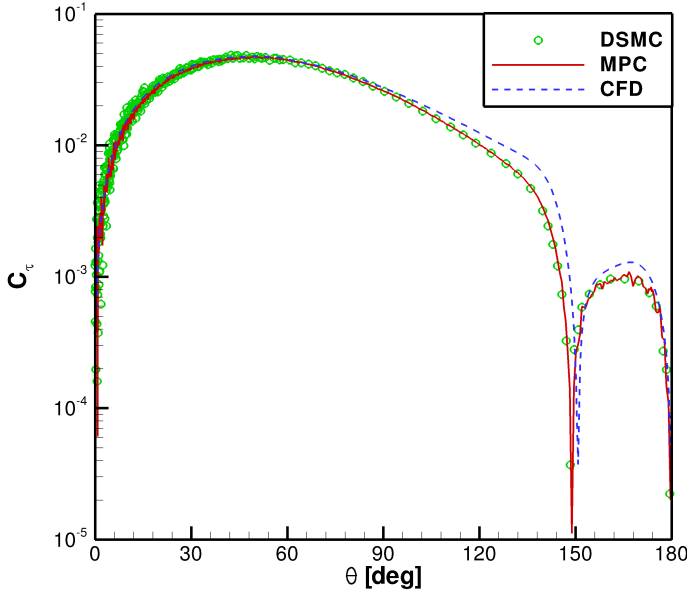


Figure 4.17: Comparison of surface quantities about the cylinder predicted by DSMC, CFD, and the MPC method for case **CM12K002**

larger portion of the cylinder, but still has large disagreement in the rarefied wake. Full CFD over predicts the DSMC heat flux by up to 40% while it under predicts full DSMC surface pressure by up to 70%. Interestingly, full CFD slightly under predicts the surface heat flux along the edge of the recirculation zone which occurs at angles greater than 150°. This could be due to the under prediction in the size of the recirculation zone predicted by full CFD relative to the full DSMC result. Again, the MPC method remains in excellent agreement with full DSMC predictions along the entire surface with differences of less than 1.5% for both surface pressure and heat transfer. Figure 4.17 compares the surface shear stress predicted by DSMC, CFD and the MPC method for case **CM12K002**. Although the difference between full CFD and DSMC has decreased with the increase in free stream density, there is still some disagreement in the magnitude in the wake region. Interestingly, now full CFD under predicts the size of the recirculation zone by over 7% relative to full

Table 4.1: Computational performance and memory requirements for the MPC method

Case	Computational Cost(Speedup)	Ideal Speedup	Memory Usage
<b>CM12K01</b>	34.% (2.94 $\times$ )	2.66	28%
<b>CM12K002</b>	3.56% (28.1 $\times$ )	17.6	75%

DSMC, while the MPC method is within 1.5% of full DSMC.

### Computational Performance

The MPC method reproduces full DSMC results by using DSMC in rarefied regions while decreasing the computational cost by limiting DSMC to *only* regions that are in collisional nonequilibrium. Continuum regions are computed using an implicit Navier-Stokes solver. By loosely coupling the methods and studying steady-state flows, the time-step used by CFD can be over 100 times larger than the time-step required by DSMC for the corresponding flow. In addition, decoupling of the mesh densities allows CFD to be unrestricted by DSMC cell size requirements, and can use cells that are up to 18 times larger in area. This significantly decreases the computational time and memory usage required by the MPC method to reproduce full DSMC results. The decreases in computational cost of the MPC method compared to full DSMC are summarized in Table 4.1. To make a fair comparison, the number of sample time-steps after reaching steady-state are the same for both full DSMC and the MPC DSMC module. In addition, all simulations are performed in parallel with the number of processors selected such that the average number of particles on each processor remains the same for each simulation method. Here, the actual speedup is defined as the ratio of the CPU time required for the full DSMC calculation to the CPU time required for the MPC method calculation. The ideal speedup is defined

as the ratio of particles used in a full DSMC simulation compared to the number in the corresponding MPC simulation. Since the computational cost of a DSMC simulation nearly scales linearly with the number of particles in the simulation, this should be the upper limit for computational speedup for that problem. The MPC method actually outperforms the ideal speedup ratio. This is because the unsteady portion of the MPC computation is much less than that of the corresponding DSMC simulation since MPC simulations begin from a fully converged CFD solution. The memory usage is defined as the ratio of the memory used by an MPC simulation to the memory used by the corresponding DSMC simulation. Here, the MPC method requires significantly less memory compared to full DSMC for the higher Knudsen number case, and moderately less for the lower Knudsen number case.

The computational requirements for the low Knudsen case can be directly compared to published requirements [4] for the serial implementation of the MPC method with a single temperature describing translational and rotational energy modes in the continuum model. That work found that the MPC method without rotational nonequilibrium modeled in the continuum module achieved a speedup factor of 10.6 relative to full DSMC. For this case, the additional capability of modeling rotational nonequilibrium within the continuum module has reduced the cost of the MPC simulation by nearly a factor of three. There are two factors that reduce the cost of the MPC method despite the new overhead of simulating an additional conservative equation throughout the entire continuum region. First, the initial full continuum result contains a higher level of physical accuracy which reduces the number of iterations for an MPC simulation to reach the fully nonequilibrium simulation result. Secondly, with the relaxation of the breakdown parameter associated with the simulation of rotational nonequilibrium in the continuum solver, the size of the DSMC region is

reduced. In particular, the recompression wave in the far wake region changes from being labeled rarefied to continuum. This has the net result of decreasing the number of DSMC simulators in the MPC simulation by nearly 40%.

#### 4.3.2 Flow Over an Axi-Symmetric Planetary-Probe Flow Conditions

Comparison of predictions of flow over a sting-mounted, 70-degree blunted sphere cone with full DSMC, full CFD, and the MPC method is performed. The geometry and flow conditions correspond to the moderate Knudsen number experimental test case performed in the SR3 wind tunnel in Meudon, France, with a probe diameter of 5 cm [92]. The free stream gas is N<sub>2</sub> with a velocity of 1502 m s<sup>-1</sup> and equilibrium temperature of 13.6 K which corresponds to a Mach number of 20. The wall temperature is assumed to remain constant at 300 K, while the free stream density is  $5.19 \times 10^{-5}$  kg m<sup>-3</sup> which corresponds to a global Knudsen number of 0.01. Figure 4.18 shows the continuum-rarefied interface location predicted and the variation in mean free path over the planetary probe. Due to the overlap region, the interface location correctly moves to the true continuum-rarefied boundary as the MPC method progresses towards the final rarefied flow result. The large variation in flow length scales about the probe shows that this test case is well suited for use to verify and validate the hybrid method.

#### Flow Field Properties

Figures 4.19 and 4.20, respectively, compare translational and rotational temperature contours predicted by full DSMC, full CFD, and the MPC method. In general, the MPC method has improved agreement with full DSMC results from the initial CFD result across the entire flow field. Even in regions where the CFD mod-

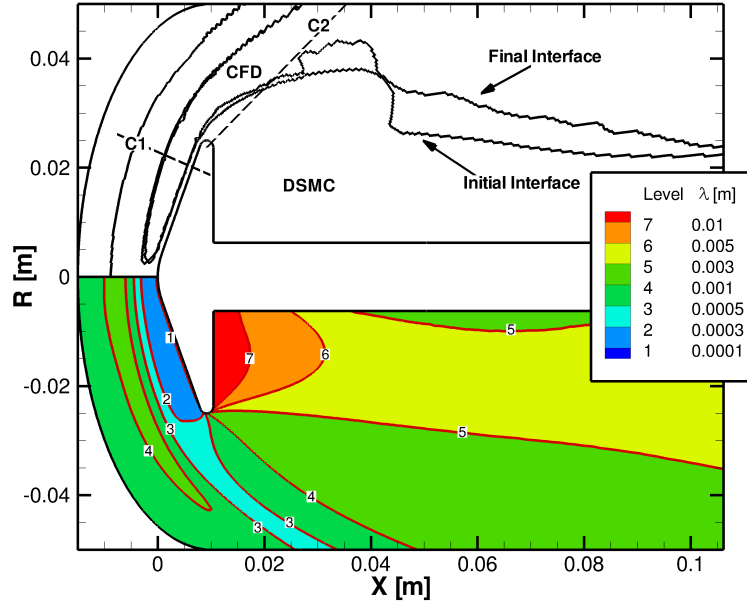


Figure 4.18: Interface location and variation of mean free path for Mach 20 flow around a sting-mounted, planetary probe with a global Knudsen number of 0.01

ule is used, the MPC method has obtained improved boundary conditions from the DSMC solver which has allowed the CFD solver to shift its result to achieve excellent agreement with full DSMC.

Figures 4.21 and 4.22 illustrate the prediction of flow field properties made by full DSMC, full CFD, and the MPC method along the extraction lines shown in Fig. 4.18. In addition to current MPC results, previous temperature results obtained with the MPC method using a single temperature model within the CFD solver are included [5]. To compensate for the inability to model rotational nonequilibrium within the continuum solver, this previous MPC simulation used a more restrictive rotational nonequilibrium parameter in compression regions shown in Eq. 3.7 [5, 67]. Vertical lines denote the interface location for the corresponding MPC result. In general, both MPC results remain in excellent agreement with the full DSMC predictions

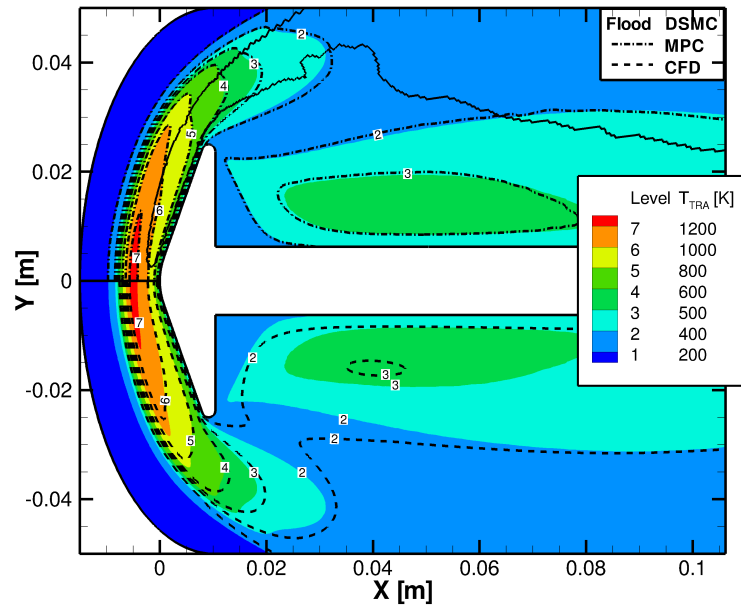


Figure 4.19: Comparison of translational temperature by DSMC, CFD, and the MPC method

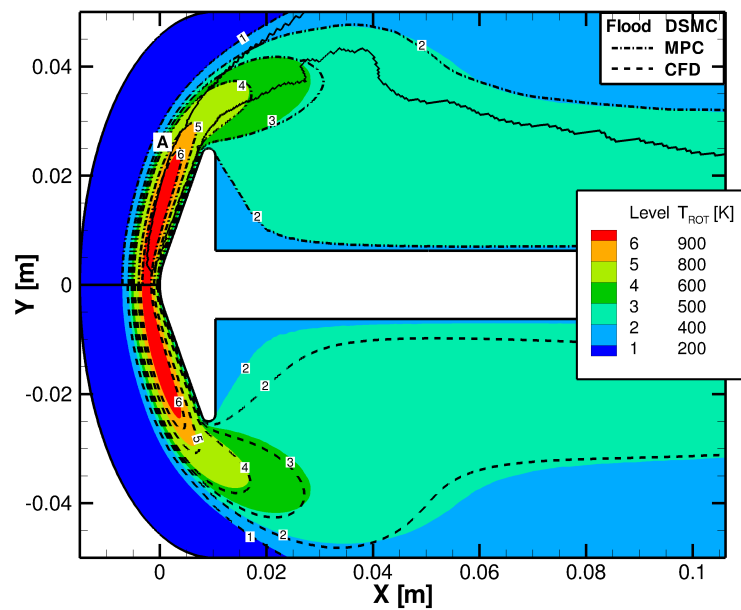


Figure 4.20: Comparison of translational temperature by DSMC, CFD, and the MPC method

along C1, while the MPC simulation with rotational nonequilibrium included in CFD can simulate a larger region of the flow with CFD which directly decreases the number of DSMC particles required and increases the computational efficiency of the MPC method relative to full DSMC. Although both MPC results remain in excellent agreement with DSMC very near the surface along C2, the MPC results with a single temperature describing translational and rotational energy modes within the CFD module can not accurately model the strong thermal nonequilibrium that exists along nearly the entire extraction line. In contrast, the MPC prediction with the ability of modeling a separate rotational temperature within the CFD solver remains in excellent agreement with full DSMC along the entire extraction line. Again, the DSMC region simulated using the MPC method with the ability to model rotational nonequilibrium within the CFD solver is smaller due to the less restrictive breakdown parameter.

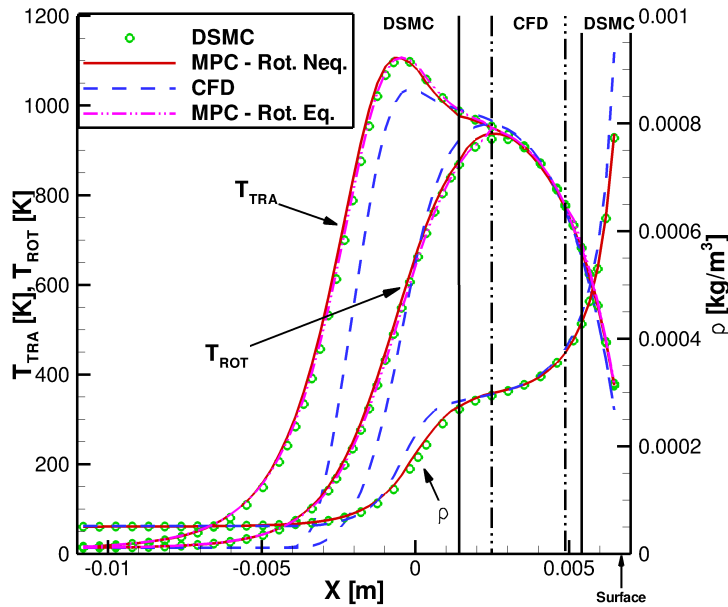


Figure 4.21: Temperature and density predicted by DSMC, CFD, MPC (Rot. Neq.), and the MPC method (Rot. Eq.) along C1

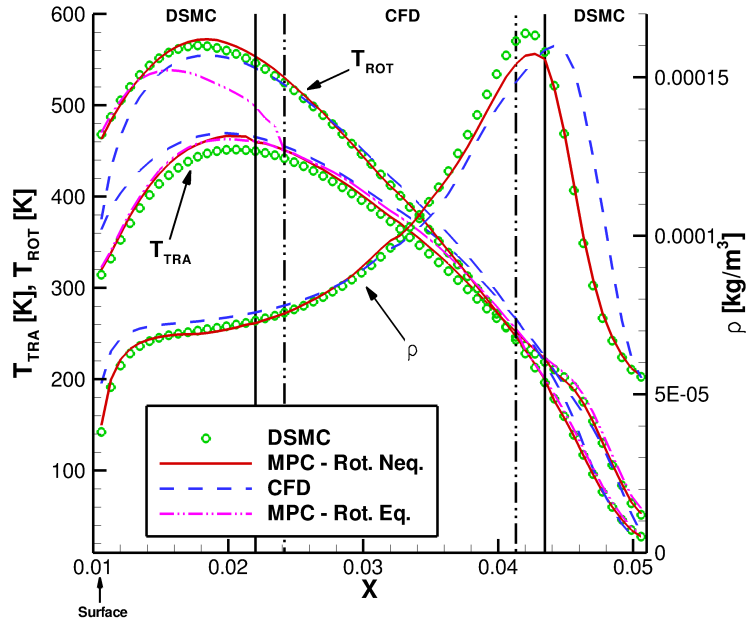


Figure 4.22: Temperature and density predicted by DSMC, CFD, MPC (Rot. Neq.), and the MPC method (Rot. Eq.) along C2

### Probability Density Functions

Figures 4.23 and 4.24, respectively, compare velocity and rotational energy probability density functions predicted by full DSMC, full CFD, and the MPC method at point A shown in Fig. 4.19. Due to the high degree of collisional nonequilibrium within the shock, the CFD velocity distribution function, which is generated from gradients and the first order Chapman-Enskog expansion, does not contain sufficient information to correctly generate the velocity distribution function predicted by full DSMC. In contrast, the MPC method is able to remain in very good agreement with DSMC throughout the entire velocity space. Despite the macroscopic rotational temperature predicted by CFD being within 5% of the full DSMC result, the rotational energy distribution function predicted by full CFD is in poor agreement with the DSMC result throughout the entire rotational energy space. Similarly to

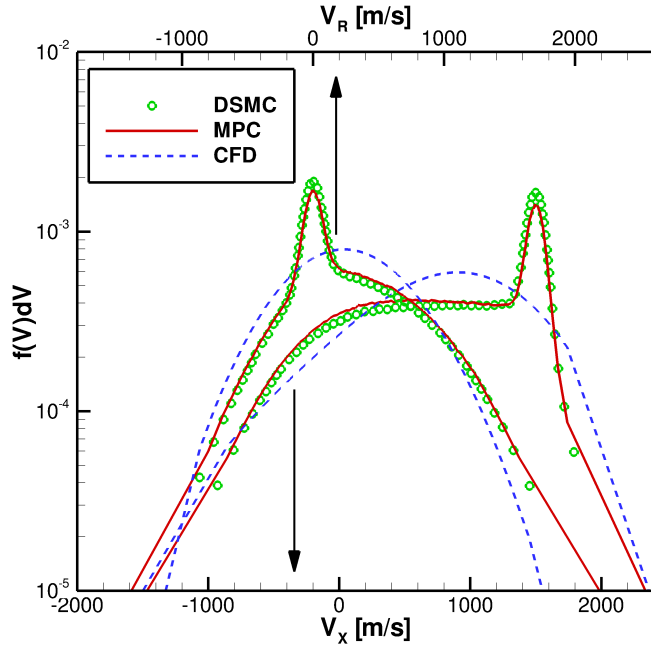


Figure 4.23: Comparison of velocity distribution functions predicted by DSMC, CFD, and the MPC method within the bow shock

the velocity distribution function, the MPC method remains in excellent agreement with full DSMC results for the rotational energy probability density function.

### Surface Properties

Figure 4.25 compares the surface coefficient of heat flux, defined in Eq. 4.27, predicted by full DSMC, full CFD, and the MPC method with available experimental measurements. Along the fore body where the flow is highly collisional, all three methods are in good agreement with each other and the experimental measurements. Despite this highly collisional flow, CFD still slightly over predicts DSMC and MPC results. This is due to the inability to correctly model the Knudsen layer within the CFD solver. As the flow expands around the corner, full CFD over predicts both DSMC and experimental measurements by over an order of magnitude. In contrast, the MPC method remains in good agreement with both the experimental

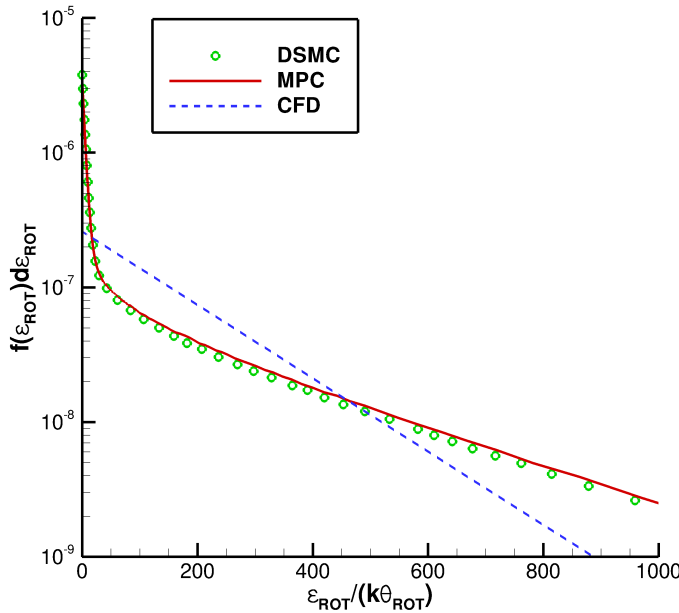


Figure 4.24: Comparison of rotational energy distribution functions predicted by DSMC, CFD, and the MPC method within the bow shock

measurements and the full DSMC results. Similarly, the MPC method remains in excellent agreement with full DSMC and experimental measurements along the sting mount, while full CFD over predicts full DSMC along the entire sting mount.

### Computational Performance

The MPC method reproduces full DSMC results by using DSMC in rarefied regions while decreasing the computational cost by limiting DSMC to *only* regions that are in collisional nonequilibrium. Continuum regions are computed using an implicit Navier-Stokes solver that can consistently model moderate rotational nonequilibrium. Table 4.2 summarizes the computational performance and memory requirements of the MPC method relative to full DSMC at this flow condition. Again, the number of DSMC samples are kept constant between MPC and full DSMC simulations, while parallel efficiency was similar by setting the final number of particles on each pro-

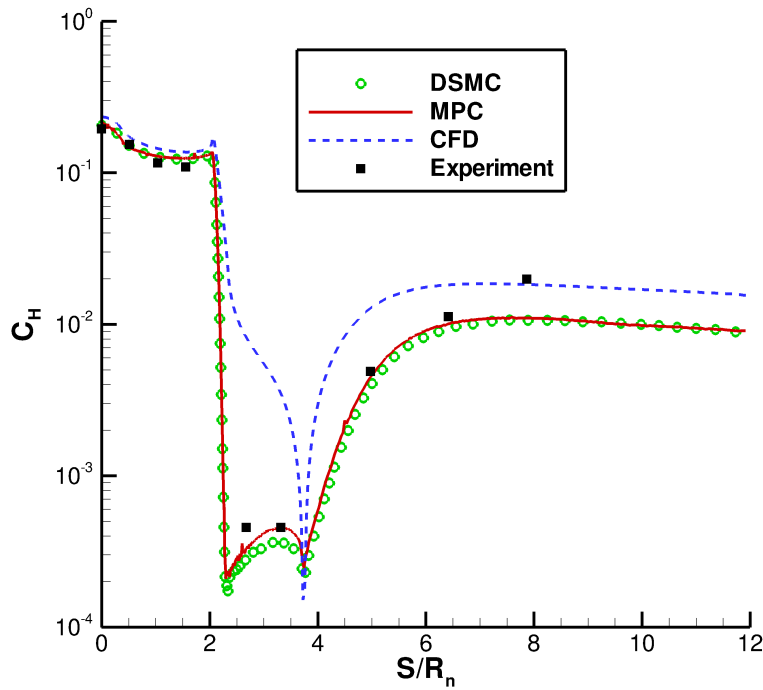


Figure 4.25: Surface heat transfer along planetary probe

Table 4.2: Computational performance and memory requirements for the MPC method.

$K_n$	Computational Cost (Speedup)	Ideal Speedup	Memory Usage	Initial CFD
0.01	60.% (1.67x)	1.65	130%	3.71%

cessor to be the same for both simulations. Despite the CFD module requiring a non-negligible amount of time within the MPC method for this test case, the ideal speedup was still exceeded due to the reduction in the number of DSMC iterations required to reach steady-state. In addition, this speedup can be compared to previous results obtained with the MPC method that used a single temperature model in the CFD module and a correspondingly more restrictive rotational nonequilibrium breakdown parameter within compression regions. Schwartzentruber et al. [5] found a relative speedup of  $1.52\times$  using a single temperature within the CFD module,

while this work finds a relative speedup of 1.67x using the same mesh and DSMC parameters. In addition, it should be noted that the MPC simulation with a single temperature modeled in the continuum solver was performed in serial and did not include the corresponding parallel overhead. Despite this extra overhead, the current simulation still outperforms the previous results. This improved efficiency is directly due to the reduction in the number of DSMC particles required by the MPC method due to the ability to model moderate rotational nonequilibrium within the CFD solver. The overhead of solving an extra conserved equation in each CFD cell is outweighed by the decrease in computational cost of simulating fewer DSMC particles. The modest speedup factor achieved for this test case is a result of the fact that the flow is highly rarefied and only a small region of the flow can be simulated with the continuum module. Due to both CFD and DSMC solvers using the same mesh density, the MPC method required moderately more memory compared to full DSMC.

#### **4.4 Summary and Conclusions from Effects of Rotational Energy Nonequilibrium**

The MPC method has been extended to simulate partially rarefied, hypersonic flows that exhibit thermal nonequilibrium between translational and rotational energy modes. An overview of the mathematical models used to describe flows that contain such physical phenomena has been provided. Comparison of physical relaxation models in each simulation module has been performed and changes to the MPC method to accommodate the inclusion of rotational energy nonequilibrium have been performed. Verification of the implementation has been performed by comparing MPC simulation results to those from full DSMC simulations. Where

available, MPC simulation results have also been compared to limited experimental measurements.

Three important conclusions can be drawn from the implementation and study of the effects of rotational energy nonequilibrium in the MPC method.

1. An implementation of a separate rotational energy equation within the continuum module can be coupled to a DSMC module within the MPC method provided the following considerations are made. First, the physical models describing relaxation processes in each simulation method should agree at the continuum limit. This allows full DSMC simulation results to be used as a verification tool where the uncertainty due to physical models is minimized. Next, the breakdown parameter associated with rotational nonequilibrium can be relaxed compared to the previous MPC simulation technique. However, it is important to continue to analyze very strong rotational energy relaxation processes with the DSMC module in order to avoid introducing physical inconsistencies in the description of the rotational energy probability density function.
2. The inclusion of modeling of rotational energy nonequilibrium within the continuum module has overall increased the agreement between predictions made by full DSMC and the MPC method. This is directly due to an increase in the physical accuracy of the continuum solver that can model the rotational relaxation processes associated with the strong expansion around hypersonic, blunt bodies with a high level of physical accuracy.
3. Despite the overhead of solving an additional conservation equation throughout the entire continuum region, the inclusion of rotational relaxation within

the continuum module has resulted in a net decrease in computational cost relative to MPC simulation requirements with a single temperature describing translational and rotational energy modes in the continuum solver. This is due to two factors. First, the increased physical accuracy of the initial continuum prediction has decreased the total number of iterations required by the MPC method to reach the nonequilibrium, steady-state solution. In addition, the increased physical accuracy has reduced the size of the flow domain that must be simulated with the DSMC module.

## CHAPTER V

### Effects of Vibrational Energy Nonequilibrium

As first outlined in Sec. 1.2, for flow over the majority of hypersonic vehicles flying through the atmosphere, the enthalpy of the free stream is sufficiently high that excitation of vibrational modes occurs in the heated shock layer. Accurate description of this flow process is important to maintain high predictive capabilities of the vehicle surface properties with the MPC method. For cases that include regions of the flow that are rarefied, the Dahmköhler number for vibrational relaxation processes is less than or on the order of unity, such that an accurate description of the entire vibrational relaxation process (as opposed to the vibrational energy mode being excited to maintain equilibrium with translational and/or rotational energy modes) is necessary. This chapter will outline the extension of the MPC method to include vibrational energy excitation that may or may not be in equilibrium with other energy modes. First, an overview of the extension of mathematical models and numerical methods required to describe vibrational energy nonequilibrium is provided, specifically the selection of vibrational relaxation models used in each simulation method that remain consistent at the continuum limit. Next, a description of the changes to the MPC method necessary to include vibrational energy excitation is given, including important changes to the information transfer procedure to reduce

the effect of high statistical scatter in regions where the vibrational temperature is much less than the characteristic temperature for vibration ( $\theta_{\text{VIB}}$ ). Then, the MPC method is applied to hypersonic flow over a two-dimensional cylinder, compared to full CFD predictions, and verified with full DSMC simulation results. Finally, a summary of the important conclusions from the study of inclusion of vibrational energy excitation in the MPC method to simulate partially-rarefied, hypersonic flows are reviewed.

## 5.1 Extension of Physical Models

Extension of the mathematical and numerical models required to include vibrational energy excitation and nonequilibrium within an MPC method are first discussed. Extension of the Boltzmann equation, its relevance to the development of vibrational collision models in DSMC, and an added conservation equation to model vibrational energy nonequilibrium within the Navier-Stokes equations are outlined. Comparison of the vibrational energy relaxation models is performed to verify that the continuum and rarefied relaxation models remain consistent at the continuum limit, and an example of one such simulation is shown.

### 5.1.1 Extension of the Boltzmann Equation

In the same manner outlined in Sec. 4.1.1, the general Boltzmann equation (as seen in Eq. 2.1) can be extended to include internal, quantized energy by modeling the rate of change of the probability density function,  $f_i(\mathbf{x}, \mathbf{c}, t, E_i)$ , for each quantum state  $i$ , as first shown in Eq. 4.1 and repeated below.

$$\frac{\partial}{\partial t} [n_i f_i] + c_m \frac{\partial}{\partial x_m} [n_i f_i] = \left\{ \frac{\partial}{\partial t} [n_i f_i] \right\}_{\text{col}} \quad (4.1)$$

Now the collision integral, shown in Eq. 4.2, must include a collision cross section,  $\sigma_{i,j}^{i',j'}$ , that is not only dependent on the velocity, but the initial  $(i, j)$  and final  $(i', j')$  vibrational quantum states of the two particles.

$$\left\{ \frac{\partial}{\partial t} [n_i f_i] \right\}_{\text{col}} = \Sigma_{j,i',j'} \int_{-\infty}^{\infty} \int_0^{4\pi} (n_{j'} f_{j'} n_{i'} f_{i'} - n_j f_j n_i f_i) g_{i,j} \sigma_{i,j}^{i',j'} d\Omega d\mathbf{V}_j \quad (4.2)$$

Identical to the modeling of an excited rotational energy mode with the Boltzmann equation, as the two particles collide, either one can move through the four-dimensional velocity and internal energy space, assuming one internal energy mode and the collision cross section determines the rate at which internally elastic and inelastic collisions occur within the flow. Unlike the rotational energy mode, the internal quantum energy jump between levels associated with vibrational energy is usually not small compared to the energy content of the flow. Therefore, assuming a fully excited state and a continuous energy distribution function would be inappropriate and introduces significant physical error. Therefore, the probability density function remains quantized to maintain the physical accuracy of the vibrational energy model and no further simplification of the collision integral within a kinetic method is appropriate. It is important to note that the addition of a quantized internal energy, such as vibrational energy, does not directly increase the dimensionality of the Boltzmann equation. Instead, it introduces complexity of the mathematical model by requiring a solution of  $N_v$  coupled six-dimensional equations where  $N_v$  is the number of vibrational energy levels. For typical diatomic species in air, there are about 30-40 vibrational levels before the energy available in the vibrational energy mode is sufficient to spontaneously dissociate the molecule. Therefore, inclusion of vibrational excitation increases the computational expense of obtaining a deterministic numerical solution to the Boltzmann equation by a factor between 30 and

40.

Vibrational energy is typically modeled with the simple harmonic oscillator approximation, so that the energy jump between vibrational levels remains constant at all vibrational levels. This is consistent with using the Born-Oppenheimer approximation for internal energy states where vibrational energy states are considered to be decoupled from the rotational and electronic energy states of the molecule [88]. This assumption allows vibration-translation, vibration-rotation, and vibration-vibration energy transfer to occur; however in this work, vibration-translation relaxation is assumed to be the dominant energy transfer method and the other two transfer processes are ignored.

### 5.1.2 Vibrational Relaxation in the DSMC Method

Similar to rotational relaxation, modeling of vibrational relaxation in the DSMC method assumes that the total collision cross section is independent of vibrational energy, and the vibrationally inelastic cross section is a fraction of this total cross section. Therefore, vibration-translation relaxation modeling processes are applied probabilistically to the collision partners within the DSMC collision routine to directly simulate the physics of the collision integral that is shown in Eq. 4.2.

The DSMC module used in this work has two different models available to simulate the vibration-translation relaxation process. The first is a phenomenological model based on the method described by Boyd [93] that calculates a variable probability of a vibrationally inelastic collision occurring based on the relative velocity between two colliding particles. First, separate phenomenological variable probabilities that are based on continuum relaxation times, that are described in Sec. 5.1.3 and have been proposed by Millikan and White [94] and Park [95], are computed.

The form of the Millikan and White variable probability is given by Eq. 5.1 where  $Z_o$ ,  $\alpha$  and  $g^*$  are found from VHS parameters and by evaluating Eq. 5.2 such that the relaxation process reproduces the established macroscopic relaxation times under continuum conditions.

$$\phi_{MW}(g) = \frac{1}{Z_o} g^\alpha \exp\left(\frac{-g^*}{g}\right) \quad (5.1)$$

$$\frac{1}{\tau_{MW} \nu_s} = \int_0^\infty \phi_{MW}(g) f(g) dg \quad (5.2)$$

Again, the collision rate,  $\nu_s$ , can be calculated from the VHS collision model using Eq. 4.16 and is repeated below.

$$\nu_s = \frac{1}{\tau_{coll,s}} = \sum_i \left( n_i d_{ref,s,i}^2 \left( \frac{8\pi k T_{ref,i}}{\mu_{s,i}^*} \right)^{\frac{1}{2}} \left( \frac{T_{TRA}}{T_{ref,i}} \right)^{1-\omega_i} \right) \quad (4.16)$$

However, the analytical evaluation of the integral can only be found approximately using the method of steepest descent. This approximation can result in errors in the effective relaxation rate in the DSMC method that may not agree with continuum rates at the continuum limit. Further details of these errors are shown later in this chapter. In a similar manner, an instantaneous probability can be formulated for Park's high temperature correction such that it satisfies Eq. 5.3.

$$\frac{1}{\tau_P \nu_s} = \int_0^\infty \phi_P(g) f(g) dg \quad (5.3)$$

The total probability for a vibrationally inelastic collision can be formulated from the two variable probabilities as shown in Eq. 5.4.

$$\phi_{tot} = \frac{\phi_{MW} \phi_P}{\phi_{MW} + \phi_P} \quad (5.4)$$

Similar to a correction proposed by Lumpkin et al. [90] for rotational relaxation processes, the Gimelshein [96] correction factor, shown in Eq. 5.5, is applied to all DSMC vibrational relaxation times to account for differences in the definition of relaxation

time used by continuum and kinetic methods and to minimize inconsistency between the two modules in the MPC method at the continuum limit.

$$\tau_{\text{TRA-VIB}}^{\text{DSMC}} = \tau_{\text{TRA-VIB}}^{\text{CFD}} \frac{\eta_{\text{TRA}}}{\eta_{\text{TRA}} + \frac{1}{2}\eta_{\text{VIB,TRA}}^2 \exp(\theta_{\text{VIB}}/T_{\text{VIB}})} \quad (5.5)$$

This results in the final probability of a particle collision pair experiencing a vibrational relaxation process given by Eq. 5.6 that is used within the DSMC flow module. Full details of the implementation of the variable probability vibration-translation relaxation model can be found in Ref. [74].

$$\phi_{\text{tot,fin}} = \left( \frac{\phi_{\text{MW}} \phi_{\text{P}}}{\phi_{\text{MW}} + \phi_{\text{P}}} \right) \left( \frac{\eta_{\text{TRA}}}{\eta_{\text{TRA}} + \frac{1}{2}\eta_{\text{VIB,TRA}}^2 \exp(\theta_{\text{VIB}}/T_{\text{VIB}})} \right) \quad (5.6)$$

Approximations to evaluation of the integral in Eq. 5.2 can cause discrepancy in relaxation times predicted by CFD and DSMC in regions of the flow that can be considered continuum [97, 98, 3]. Although correction factors have been proposed and used by other researchers, they are empirical in nature and currently can only be applied on average over the entire flow field.

To resolve these discrepancies, an additional vibrational energy relaxation model is implemented within the DSMC module that calculates the probability of vibrationally inelastic collisions in each cell based on cell-averaged quantities and applies the same probability to every collision pair in the cell. This method uses the macroscopic translational temperature to calculate the continuum relaxation time using Eq. 5.15, which is explained in the proceeding subsection, and applies the Gimelshein correction factor to find the DSMC relaxation time. The average probability,  $\langle P \rangle_{\text{VIB}}$ , within the cell is then calculated using Eq. 5.7 and applied to all collisions in the cell. The macroscopic cell translational temperature that is used to compute the relaxation times is tracked in each DSMC cell using the subrelaxation procedure in

the DSMC module that has been described in Sec. 3.2.3.

$$\langle P \rangle_{\text{VIB}} = \frac{1}{\tau_{\text{VIB},s}^{\text{DSMC}} \nu_s} \quad (5.7)$$

For the simulation of either vibration-translation relaxation model, an acceptance-rejection routine is used to probabilistically simulate the relaxation process. Then, energy is distributed among available translational and vibrational energy modes using a modified version of the Larsen-Borgnakke [91] procedure that accounts for quantized vibrational levels.

### 5.1.3 Vibrational Relaxation in Continuum Methods

Despite similar final results, the derivation of a continuum description of a separate vibrational energy mode is unlike the derivation of the rotational energy equation used in continuum methods, where a moment over the entire four-dimensional velocity/rotational energy space is taken. Now a moment over each Boltzmann equation with respect to the vibrational energy associated with a quantum level,  $\varepsilon_{\text{VIB},i}$  is performed. Then, a summation of all moment equations is calculated which results in Eq. 5.8.

$$\begin{aligned} \sum_i \int_{-\infty}^{\infty} \varepsilon_{\text{VIB},i} \frac{\partial}{\partial t} [n_i f_i] d\mathbf{c}_{m,i} + \sum_i \int_{-\infty}^{\infty} \varepsilon_{\text{VIB},i} c_m \frac{\partial}{\partial x_m} [n_i f_i] d\mathbf{c}_{m,i} \\ = \sum_i \int_{-\infty}^{\infty} \varepsilon_{\text{VIB},i} \left\{ \frac{\partial}{\partial t} [n_i f_i] \right\}_{\text{col}} d\mathbf{c}_{m,i} \end{aligned} \quad (5.8)$$

Assuming that the particle velocity and vibrational energy level are statistically independent and that the probability density function is near equilibrium, the initial term can be simplified to Eq. 5.9 where  $E_{\text{VIB}}$  is the vibrational energy per unit volume given by Eq. 5.10 and  $n_i$  is the number density of particles in the  $i$ th vibrational level.

$$\sum_i \int_{-\infty}^{\infty} \varepsilon_{\text{VIB},i} \frac{\partial}{\partial t} [n_i f_i] d\mathbf{c}_{m,i} = \frac{\partial}{\partial t} [E_{\text{VIB}}] \quad (5.9)$$

$$E_{\text{VIB}} = \rho e_{\text{VIB}} = \sum_i n_i \varepsilon_{\text{VIB},i} \quad (5.10)$$

The convection term can be simplified to Eq. 5.11 where  $\vec{u}$  is the bulk velocity vector and  $\vec{q}_{\text{VIB}}$  is the vibrational heat flux vector.

$$\sum_i \int_{-\infty}^{\infty} \varepsilon_{\text{VIB},i} c_m \frac{\partial}{\partial x_m} [n_i f_i] d\mathbf{c}_{m,i} = \nabla \cdot (E_{\text{VIB}} \vec{u} + \vec{q}_{\text{VIB}}) \quad (5.11)$$

By only taking into account vibration-translation energy exchange, the sum of the moment of the collision integral is the total measure of gain or loss of total vibrational energy due to collision processes which results in the final continuum description of the time rate of change of vibrational energy per unit volume shown in Eq. 5.12 where  $\dot{w}_{\text{VIB}}$  is the vibrational source term that is used to model the moment of the collision integral.

$$\frac{\partial E_{\text{VIB}}}{\partial t} + \nabla \cdot (E_{\text{VIB}} \vec{u}) = -\nabla \cdot (\vec{q}_{\text{VIB}}) + \dot{w}_{\text{VIB}} \quad (5.12)$$

The vibrational source term can be split into two parts: a vibrational-translational relaxation portion and a source term due to the gain and loss of vibrational energy through chemical reactions as shown in Eq. 5.13.

$$\dot{w}_{\text{VIB}} = \sum_s (S_{\text{VIB},s}^{\text{TRA-VIB}} + \dot{w}_s e_{\text{VIB},s}) \quad (5.13)$$

In this dissertation, chemical reactions are ignored and the chemistry source term,  $\dot{w}_s$ , is always zero. An expression for the vibration-translation relaxation source term,  $S_{\text{VIB},s}^{\text{TRA-VIB}}$ , which was originally derived by Landau and Teller [99], can be written as Eq. 5.14 where  $e_{\text{VIB},s}^*$  is the equilibrium specific vibrational energy and  $\tau_{\text{VIB},s}$  is the species vibration-translation relaxation time.

$$S_{\text{VIB},s}^{\text{TRA-VIB}} = \rho_s \frac{e_{\text{VIB},s}^* - e_{\text{VIB},s}}{\tau_{\text{VIB},s}} \quad (5.14)$$

Typically,  $e_{\text{VIB},s}^*$  is estimated by evaluation of Eq. 5.18 at the temperature associated with the translational energy mode. The vibrational relaxation time can be calculated using the summation of the Millikan and White correlation [94] and Park's high-temperature correction [95], shown in Eq. 5.15.

$$\tau_{\text{VIB},s}^{CFD} = \tau_{MW,s} + \tau_{P,s} \quad (5.15)$$

Equations 5.16 and 5.17 show the relaxation times using the Millikan and White correlation and Park's high temperature correction, respectively, where  $p$  is the pressure,  $\sigma_s$  is the vibrational cross section,  $n$  is the total number density, and  $m_s$  is the species mass.

$$\tau_{MW,s} = \frac{1}{p} \exp \left[ A_s \left( T_{\text{TRA}}^{-\frac{1}{3}} - B_s \right) - 18.42 \right] \quad (5.16)$$

$$\tau_{P,s} = \frac{\sqrt{\frac{\pi m_s}{8kT_{\text{TRA}}}}}{\sigma_s n} \quad (5.17)$$

In this dissertation, a constant vibrational cross section of  $5.81 \times 10^{-21} \text{ m}^2$  is used. As previously stated, these relaxation times are also used to evaluate the phenomenological probability of a vibrationally inelastic collision used in the DSMC module.

Coupled with the Navier-Stokes equations shown in Sec. 2.2.2, additional rotational energy equation shown in Sec. 4.1.3, and equation of state shown in Eq. 2.27, the vibrational energy equation provides sufficient information to simulate gas flows with vibrational and/or rotational energy nonequilibrium at the macroscopic level. Consistent with the simple harmonic oscillator model to describe the vibrational energy spacing, a vibrational temperature,  $T_{\text{VIB}}$ , can be computed for a single species using Eq. 5.18 where  $\theta_{\text{VIB}}$  is the characteristic temperature of vibration,  $E_{\text{VIB}}$  is the vibrational energy per unit volume,  $\rho$  is the mass density,  $e_{\text{VIB}}$  is the vibrational

energy per unit mass, and  $R$  is the species gas constant.

$$\frac{E_{\text{VIB}}}{\rho} = e_{\text{VIB}} = \frac{R\theta_{\text{VIB}}}{\exp(\theta_{\text{VIB}}/T_{\text{VIB}}) - 1} \quad (5.18)$$

#### 5.1.4 Comparison of Vibrational Relaxation Models

In order to continue the use of full DSMC simulation results as a verification tool of the MPC method, the physical models used within the DSMC and CFD modules must agree at the continuum limit. If they do not agree, it would be unclear if any discrepancies between full DSMC and MPC results were caused by an incorrect implementation of the MPC method or due to inherent differences in modeling between the two simulation methods. In addition, maintaining consistent physical models that agree at the continuum limit has a supplementary benefit for application of the MPC method to analyze continuum breakdown. If the DSMC and CFD module maintain consistent results in regions that can be considered continuum and the MPC method has been thoroughly verified to produce full DSMC results, the MPC method can then be used to determine the effect of continuum breakdown by comparing with full CFD results for flows that are prohibitively expensive to predict by applying the DSMC method over the entire flow field.

Figure 5.1 shows an example of an adiabatic vibration-translation relaxation process simulated using the two DSMC models and the continuum method that are outlined in this section. The cell based vibrational relaxation rate is in much better agreement with the continuum calculation than the variable vibrational relaxation probability. This is because of errors resulting from the approximate techniques used to evaluate the integral in Eq. 5.2. The effect of the improved agreement in prediction of vibrational relaxation between DSMC and CFD methods in continuum regions will be tested within a hybrid DSMC-CFD code in the proceeding section.

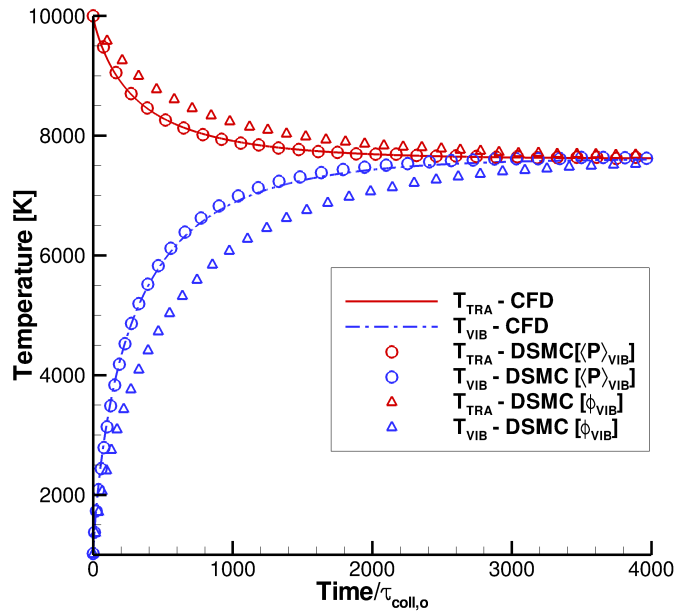


Figure 5.1: Comparison of adiabatic vibrational-translational relaxation process predicted by DSMC and CFD

## 5.2 Modifications to the MPC Method

This subsection outlines the changes to the MPC method required to maintain consistent, physically accurate simulation of gas flows with vibrationally excited energy modes that are in thermal nonequilibrium with other energy modes in parts of the flow field.

### 5.2.1 Continuum Breakdown and Interface Location

Unlike rotation-translation energy relaxation, which was described in Chapter IV and occurs at nearly the same rate as translational relaxation, vibration-translation relaxation occurs at a much slower rate. For most air species of interest, vibrational relaxation requires about a hundred times more collisions than rotational relaxation. Because of this, vibrational energy can remain far from equilibrium with the translational mode for even highly collisional flows, where the Navier-Stokes equations are

valid. Unlike rotational energy, where it is important to correctly resolve the probability density function, the slow relaxation between vibrational and translational energy modes allows for slight discrepancies in the probability density function while maintaining an acceptable level of physical accuracy. This allows the MPC to use the unmodified breakdown parameter that was shown in Eq. 4.22. Though the relaxation of vibrational energy is typically quite slow which results in much smaller gradients compared to translational or rotational energy modes, the gradient-length Knudsen number based on vibrational energy is also included in calculation of the final breakdown parameter (shown in Eq. 5.19) to ensure that the MPC method is readily applicable to other gas species, such as diatomic iodine, that exhibit faster vibrational relaxation times.

$$Br = \max(Kn_{GL-\rho}, Kn_{GL-T_{TRA}}, Kn_{GL-T_{ROT}}, Kn_{GL-e_{VIB}}, Kn_{GL-|V|}, Kn_{ROT-NEQ}) \quad (5.19)$$

To maintain consistency with the model of molecular diffusion of vibrational energy (vibrational heat transfer), the gradient-length Knudsen number is calculated based on the specific vibrational energy, rather than the vibrational temperature.

### 5.2.2 Information Transfer

As outlined in Sec. 3.2.3, the MPC method uses state-based coupling to transfer information between rarefied and continuum flow modules. The subrelaxation average, which was shown in Eq. 3.18 and is repeated below, is used to reduce the statistical scatter inherent in DSMC macroscopic information sampled over a small interval.

$$\langle Q \rangle_j = (1 - \Phi) \langle Q \rangle_{j-1} + \Phi Q_j \quad (3.18)$$

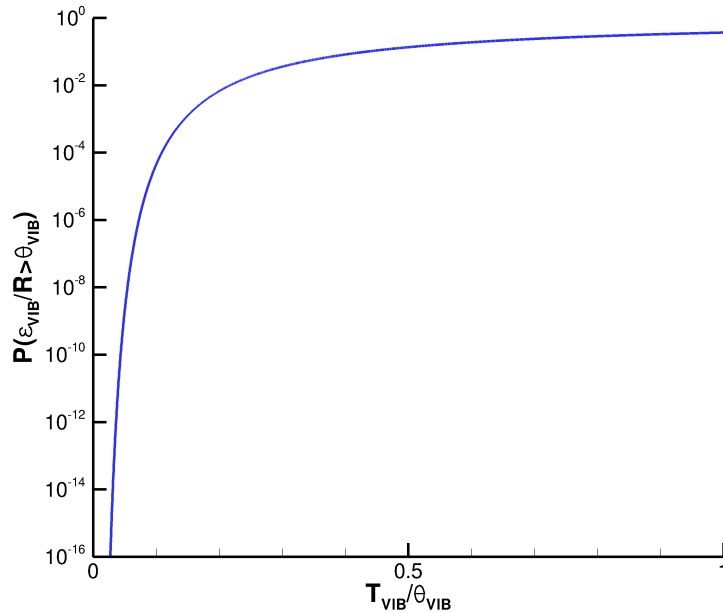


Figure 5.2: Probability of a particle with any vibrationally excited state as a function of macroscopic vibrational temperature

A  $\Phi$  value of 0.001 is used in typical MPC simulations so that the statistical scatter associated with  $\langle Q \rangle$  is at the same level as the quantity sampled over 1,000 ( $1/\Phi = 1/0.001$ ) iterations. For almost all flow variables of interest, the statistical scatter associated with a sample over 1,000 iterations is sufficiently small. However, this is not the case for vibrational energy since a discrete probability density function must be used to maintain a physically accurate description and the number of iterations required to resolve low vibrational temperatures becomes enormous. For example, Fig. 5.2 compares the probability of a particle being excited above the ground vibrational state as a function of vibrational temperature. In front of the bow shock, where free stream temperatures of less than  $0.1\theta_{\text{vib}}$  (339.5 K for N<sub>2</sub>) are commonly experienced, the probability of finding a vibrationally excited particle is less than  $1 \times 10^{-6}$  and accurately resolving the vibrational temperature in these re-

gions would require greater than 1,000,000 ( $20 \times 50,000$ ) samples. Decreasing the subrelaxation parameter,  $\Phi$ , could decrease the statistical scatter of the subrelaxation averaged vibrational temperature at the expense of efficiency, but typical high altitude free stream temperatures would require  $\Phi$  to be many orders of magnitude smaller than what is currently used. This would make any coupled hybrid method using this technique slower than full DSMC.

Instead of assigning vibrational energies consistent with the discrete Boltzmann energy probability density function, the average vibrational energy is assigned to all particles in the boundary cells. Equation 5.20 shows the final calculation of the vibrational energy where  $N_{max}$  is the level at which the discrete Boltzmann distribution is truncated,  $R$  is the universal gas constant, and  $P_i$  is the probability of a particle having the  $i$ th level of vibrational energy.

$$E_{\text{VIB}} = \sum_{i=0}^{N_{max}} P_i i \theta_{\text{VIB}} R \quad (5.20)$$

Assuming vibrational energy is modeled as a simple harmonic oscillator, the probability of a particle being in a vibrational level can be calculated using Eq. 5.21 where  $\varsigma$  is the ratio of vibrational temperature to characteristic vibrational temperature shown in Eq. 5.22.

$$P_i = \exp[-i/\varsigma] (1 - \exp[-1/\varsigma]) \quad (5.21)$$

$$\varsigma = \frac{T_{\text{VIB}}}{\theta_{\text{VIB}}} \quad (5.22)$$

The maximum level,  $N_{max}$ , is chosen such that the probability of a particle having a vibrational energy greater than that level is less than  $1 \times 10^{-8}$ .

At higher vibrational temperatures, such that  $\varsigma > 0.2$ , vibrational energies can be sampled from the discrete Boltzmann probability density function without adversely affecting the efficiency of the MPC method and may be necessary for physical pro-

cesses that directly depend on the vibrational energy distribution function such as chemistry. Based on the results shown in Fig. 5.3(a), a switching parameter,  $\varsigma$ , may be used to change from assigning average energies to all particles generated in a cell at low temperatures to sampling energies directly from the discrete Boltzmann energy probability density function at higher temperatures. The results shown in Fig. 5.3(a) suggest that a switching value of 0.2 may be sufficient, such that the average value is assigned when  $\varsigma < 0.2$  and particle vibrational energies are sampled from the Boltzmann probability density function when  $\varsigma > 0.2$ . However in this dissertation, the cell average vibrational energy (calculated using Eq. 5.20), is applied to all regions to evaluate the effect of the limiting case of setting the switching value to infinity. Regardless of the method used to assign vibrational energies, discrete vibrational levels are selected after vibrationally inelastic collisions.

In addition to the statistical scatter associated with assigning vibrational energies in low temperature regions, it is also important to note the effect of the order of operations between calculating the vibrational temperature and applying the subrelaxation average. Application of the subrelaxation procedure on conserved or primitive variables has an important effect on the accuracy of the subrelaxation process when a strong nonlinear relationship exists between average energy and temperature. For all other variables, the primitive variables ( $\rho, u_i, T_{\text{TRA}}, T_{\text{ROT}}$ ) are first computed in each cell and the subrelaxation average applied to these quantities. However, direct application of this procedure enhances the effect of statistical scatter associated with low vibrational temperatures and can lead to random walk errors. The effect of scatter at low energies is simulated here by directly sampling vibrational energies from the discrete version of the Boltzmann energy probability density function consistent with the simple harmonic oscillator description with twenty particles in

each cell. Then, the average vibrational energy is calculated and the subrelaxation procedure is applied to the energy. Finally, a vibrational temperature is calculated using Eq. 5.18 and the smoothed average vibrational energy. Figure 5.3(a) shows the results of this test at various equilibrium vibrational temperatures. Although the statistical scatter noticeably increases as the vibrational temperature decreases, the sampled results remain, on average, near the equilibrium value. A similar simulation is performed by first computing a vibrational temperature from the sampled data at each time-step, and then applying the subrelaxation procedure to the vibrational temperature. Figure 5.3(b) shows the results from such a simulation at varying vibrational temperatures. Now, the results are consistent with the previous algorithm at the highest temperature ( $\zeta = 0.5$ ), but diverge to incorrect values for very low vibrational temperatures. This effect is directly due to the highly nonlinear relation between vibrational energy and temperature. Figure 5.4 shows the relation of vibrational temperature as a function of vibrational energy which is computed by solving for the vibrational temperature in Eq. 5.18. The relation approaches a vertical asymptote as the average vibrational energy approaches zero. This has the effect of amplifying the statistical scatter that is already high due to the large energy spacing associated with discrete vibrational energies and causes the random walk shown in Fig. 5.3(b). Therefore, unlike the random translational and rotational energy modes, the subrelaxation procedure is applied directly to the vibrational energy,  $e_{\text{VIB}}$ , which is calculated using Eq. 5.23, rather than to the vibrational temperature, in the MPC method to avoid the nonlinear amplification of the statistical scatter experienced in cells that have low vibrational energies.

$$e_{\text{VIB}} = \frac{1}{N_{\text{real}}} \sum_{rc=1}^{N_{rc}} \sum_{P_{rc}=1}^{N_{P_{rc}}} \frac{W_{rc}}{m_{P_{rc}}} \varepsilon_{\text{VIB}, P_{rc}} \quad (5.23)$$

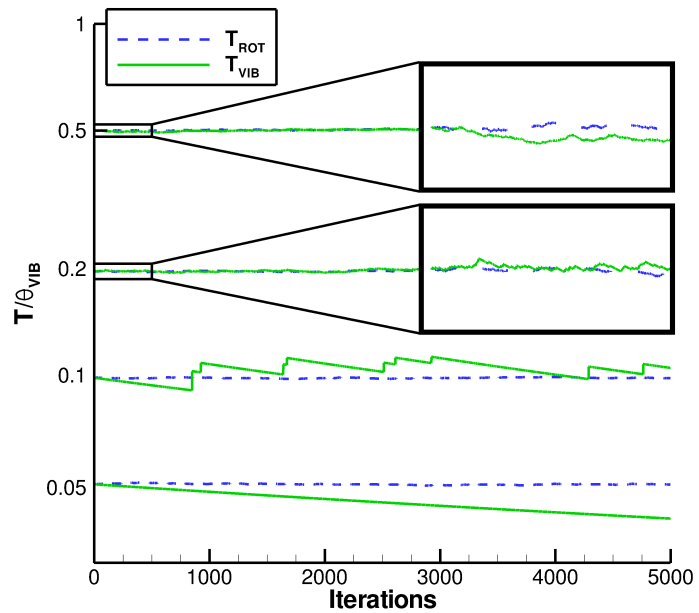
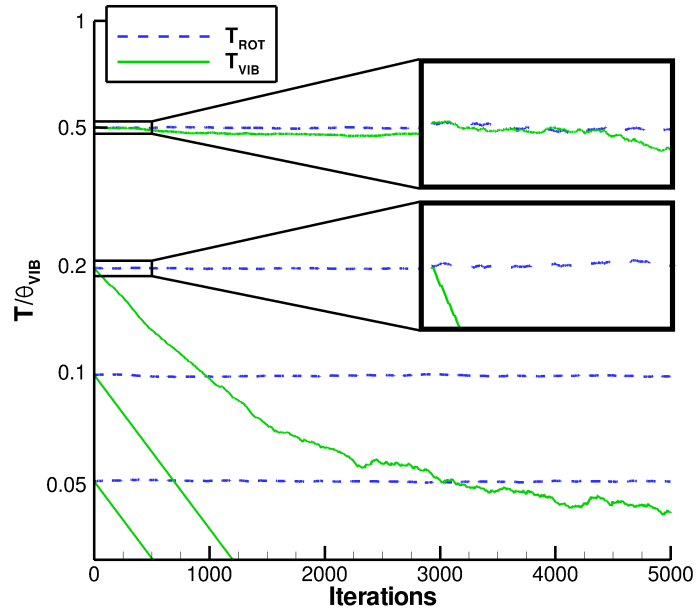
(a) Subrelaxation applied to  $Q = E_{\text{vib}}$ (b) Subrelaxation applied to  $Q = T_{\text{vib}}$ 

Figure 5.3: Comparison of the level of statistical scatter of subrelaxation averages of internal temperatures at various levels

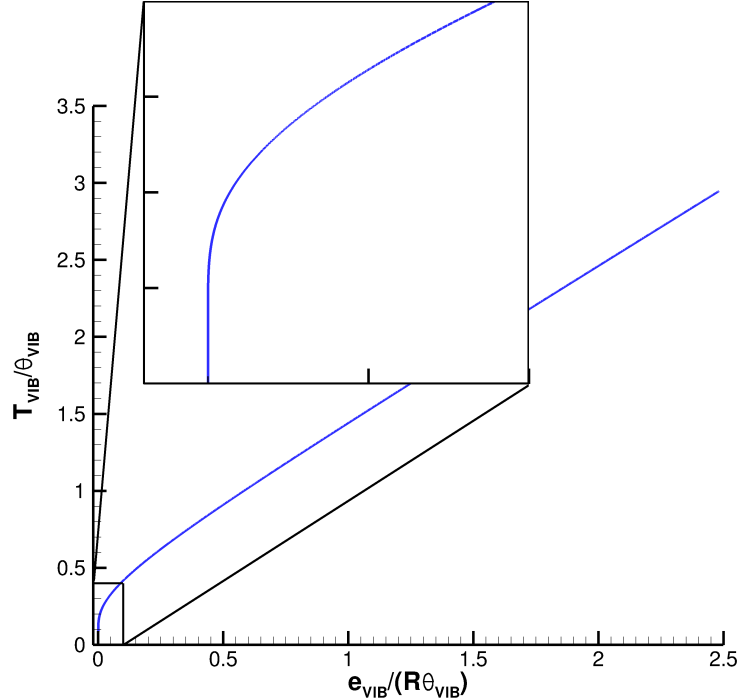


Figure 5.4: Vibrational temperature as a function of specific vibrational energy

Finally, an estimate of the vibrational temperature is computed using Eq. 5.18 and the subrelaxed value of average vibrational energy.

### 5.3 Verification of the MPC Method

The goal of the MPC method is to be able to reproduce full DSMC results to within 5% using a fraction of the computation cost. In order to verify the implementation of modeling the excitation of a vibrational energy mode that may or may not be in equilibrium with the other energy modes, the MPC method is applied to Mach 15 flow over a cylinder with a global Knudsen number of 0.01. The MPC results are compared with full CFD predictions and assessed with full DSMC simulation results.

In addition, the effect of the vibration-translation relaxation model used in the DSMC method is studied by running separate cases with each relaxation model. Case **CM15K01vp** corresponds to the approach where vibrational relaxation in

the DSMC module is simulated using the variable probability method based on the relative velocity between collision partners which is shown in Eq. 5.4. Case **CM15K01<sub>CB</sub>** corresponds to the approach where vibrational relaxation in the DSMC module is simulated using the cell-based constant probability which is shown in Eq. 5.7.

In addition to macroscopic quantities, the heat flux to the cylinder surface predicted by each simulation technique are compared for each case, and the computational requirements of each MPC simulation are compared to the requirements for corresponding full DSMC simulations.

### 5.3.1 Flow Over a 2D Cylinder

#### Flow Conditions

Hypersonic flow about a cylinder with a free stream Mach number of 15 is simulated. The free stream gas is N<sub>2</sub> with a number density of  $n_{\infty} = 1.61 \times 10^{21} \text{ m}^{-3}$  and equilibrium temperature of  $T_{\text{TRA},\infty} = T_{\text{ROT},\infty} = T_{\text{VIB},\infty} = 217.5 \text{ K}$ . This corresponds to a free stream density of  $\rho_{\infty} = 7.48 \times 10^{-5} \text{ kg m}^{-3}$  and a pressure of  $p_{\infty} = 4.22 \text{ Pa}$ . The diameter of the cylinder simulated is  $d = 8 \text{ cm}$  which results in a global Knudsen number of  $Kn_{\infty} = 0.01$ . The cylinder wall temperature is set to  $T_w = 1,000 \text{ K}$  with full diffuse reflection in DSMC simulations and a no-slip, isothermal condition in CFD simulations. The vibrational characteristic temperature used for all vibration temperature calculations is  $\theta_{\text{VIB}} = 3395 \text{ K}$ . A constant time-step of  $1.5 \times 10^{-8} \text{ s}$  is used in the DSMC module for all simulations, while a maximum CFL number of 50 is used in the CFD module. The full DSMC simulation requires about 26 million particles, while the full CFD calculation is performed on a mesh of 30,000 cells.

Figure 5.5 shows the final and initial interface locations for the **CM15K01<sub>CB</sub>** case along with extraction lines that are used to compare macroscopic quantities predicted

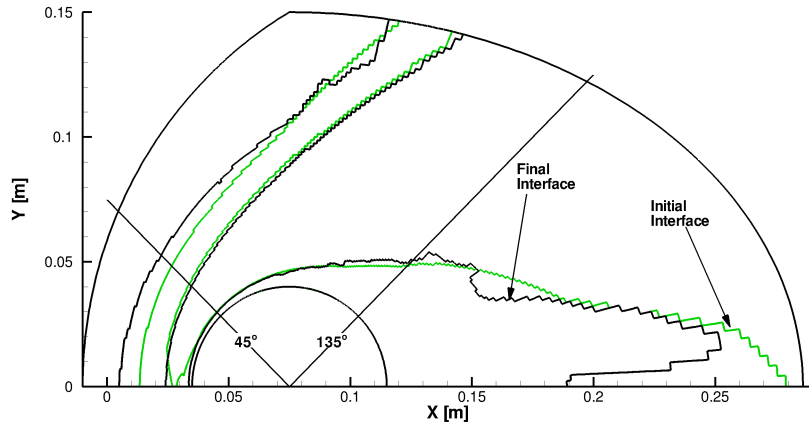


Figure 5.5: Comparison of initial and final rarefied-continuum interface locations used by the MPC method for the **CM15K01<sub>CB</sub>** case

by full DSMC, full CFD, and the MPC method. The interface locations for case **CM15K01<sub>VP</sub>** are very similar and are not shown for clarity. The DSMC module is used in the diffuse bow shock and also in the high gradient boundary layer and low density wake, while the CFD module is applied to the remainder of the flow.

### Flow Field Properties

Figures 5.6 and 5.7 compare the translational and vibrational temperature contours, respectively, predicted by full DSMC, full CFD, and the MPC method for the **CM15K01<sub>VP</sub>** case. For the translational temperature contours, the MPC method predictions are in much better agreement with the DSMC results than the full CFD predictions are with the DSMC results. The largest discrepancy observed between the MPC and the DSMC results for any flow variable other than the vibrational temperature remains below 4%. When comparing vibrational temperature contours, the MPC method greatly improves agreement with the full DSMC results over the full CFD predictions. The worst agreement occurs in the expansion region where the vibrational temperatures predicted by the DSMC and the MPC simulations deviate

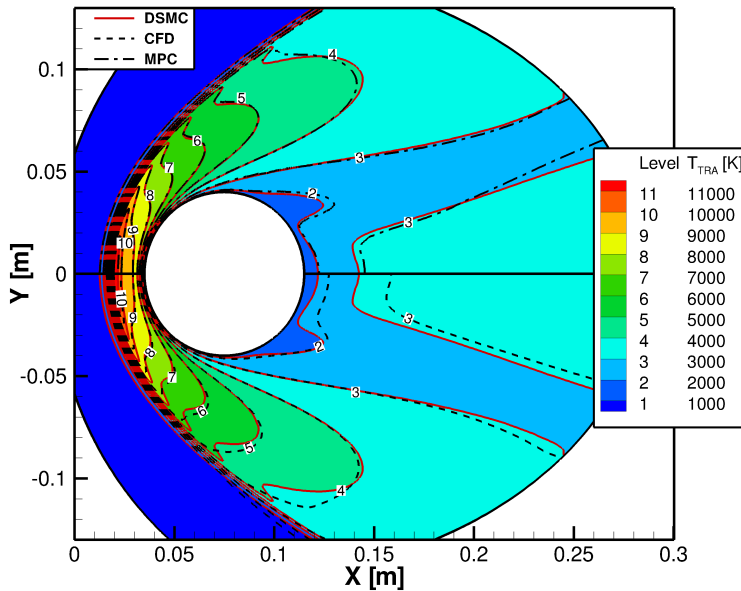


Figure 5.6: Comparison of temperature contours predicted by full DSMC, full CFD, and the MPC method for the **CM15K01<sub>VP</sub>** case

up to about 8%. This discrepancy can be partially attributed to the differences in the computation of the effective vibration-translation relaxation rates at near continuum conditions used in rarefied and continuum modules for this case.

Figure 5.8 shows a comparison of translational temperature contours predicted by full DSMC, full CFD, and the MPC method for the **CM15K01<sub>CB</sub>** case. Again, the agreement between the DSMC and the MPC predictions is excellent while the full CFD simulation results fail to accurately predict the flow in regions that are in collisional nonequilibrium. The largest discrepancy found between DSMC and the MPC results remains below 5% for all flow variables. Figure 5.9 compares the vibrational temperature contours predicted by full DSMC, full CFD, and the MPC method. The MPC method can nearly reproduce the full DSMC solution even in areas where the full DSMC and the full CFD predictions are in very poor agreement.

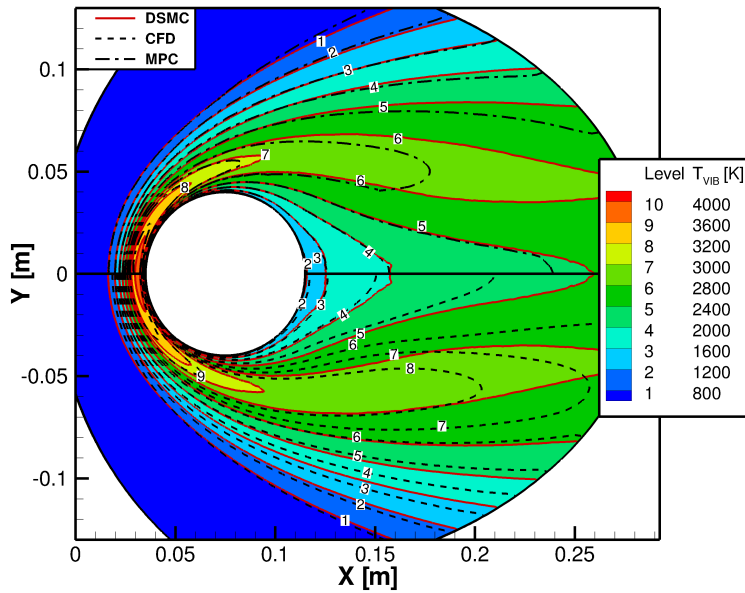


Figure 5.7: Comparison of temperature contours predicted by full DSMC, full CFD, and the MPC method for the **CM15K01VP** case

Still, there is a discrepancy between the MPC method and the full DSMC results in the expansion region, but the agreement between the DSMC and the MPC predictions has improved. Now, the maximum difference between the DSMC and the MPC results remains below 4%. The improved agreement between the MPC and the full DSMC predictions can be attributed to the improved agreement of the effective vibration-translation relaxation rates at near continuum conditions between CFD and the DSMC cell-based model.

Figure 5.10 compares the temperature predictions along a  $45^\circ$  extraction line by the DSMC, the CFD, and the MPC method with each vibrational relaxation model. In general, the MPC method has significantly improved agreement with the DSMC results compared to the CFD predictions regardless of the relaxation model. Even in regions that are considered continuum, and the CFD module is used, the MPC

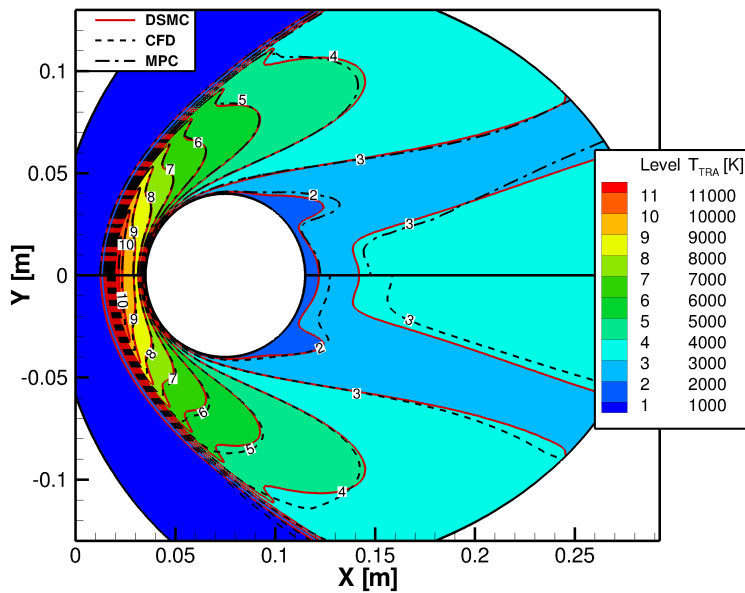


Figure 5.8: Comparison of temperature contours predicted by full DSMC, full CFD, and the MPC method for the **CM15K01<sub>CB</sub>** case

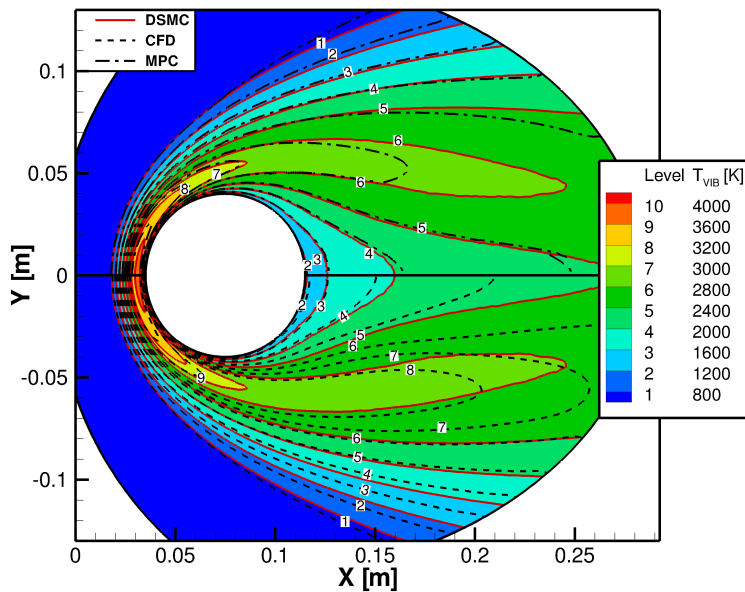


Figure 5.9: Comparison of temperature contours predicted by the DSMC, the CFD, and the MPC method for the **CM15K01<sub>CB</sub>** case

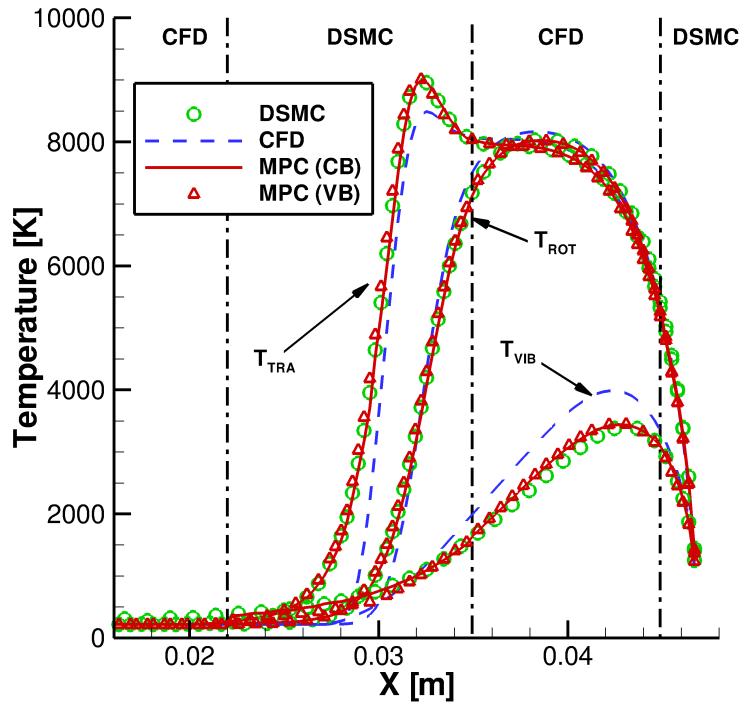


Figure 5.10: Comparison of temperatures predictions by full DSMC, full CFD, and the MPC method along the  $45^\circ$  extraction line for the **CM15K01<sub>VP</sub>** and **CM15K01<sub>CB</sub>** cases.

method can improve agreement with the full DSMC simulation results due to the improved boundary conditions provided to the continuum module. Though the cell based relaxation model provides slightly improved agreement with full DSMC for vibrational temperature at around  $x = 0.04$  m, the difference in the two relaxation models is negligible along this extraction line.

Figures 5.11(a) and 5.11(b) show the vibrational temperature predicted by DSMC, CFD, and the MPC method along the  $135^\circ$  extraction line for the **CM15K01<sub>VP</sub>** and **CM15K01<sub>CB</sub>** cases, respectively. Similar to the vibrational temperature contour plots, the MPC method greatly improves agreement with the full DSMC results

compared to the full CFD predictions for both cases. Despite the improved agreement, the effect of different relaxation rates in the **CM15K01<sub>VP</sub>** case is evident at the interface location between the continuum and rarefied flow modules. Here, there is a distinct change in vibrational temperature gradient. This is caused by the difference in the effective vibration-translation relaxation rates used in each module. When compatible relaxation rates are used in the two modules, as is done for the **CM15K01<sub>CB</sub>** case, the solution is smooth with no abrupt change in gradient at the interface. Though small for this test case, the difference in effective vibration-translation relaxation rates could have a larger effect on agreement between full DSMC results and the MPC predictions for flows where the continuum region exhibits faster relaxation rates which can occur in higher enthalpy or higher density flows.

## Surface Properties

For many hypersonic problems of interest, accurate prediction of surface properties has a strong impact on vehicle design. Predictions of heat transfer from full DSMC, full CFD, and the MPC method are compared using the definition of the coefficient of heat transfer that was previously shown in Eq. 4.27. Figures 5.12 and 5.13 show the heat transfer coefficient predicted by full DSMC, full CFD, and the MPC method for the **CM15K01<sub>VP</sub>** and **CM15K01<sub>CB</sub>** cases, respectively. Despite the slightly improved agreement in the prediction of vibrational temperature in the flow field between the full DSMC and the MPC results for the **CM15K01<sub>CB</sub>**, both cases have the same level of agreement between the MPC and the DSMC results for predicted heat transfer to the body. This is due to both MPC results maintaining excellent agreement with the full DSMC predictions near the body. Similar to heat

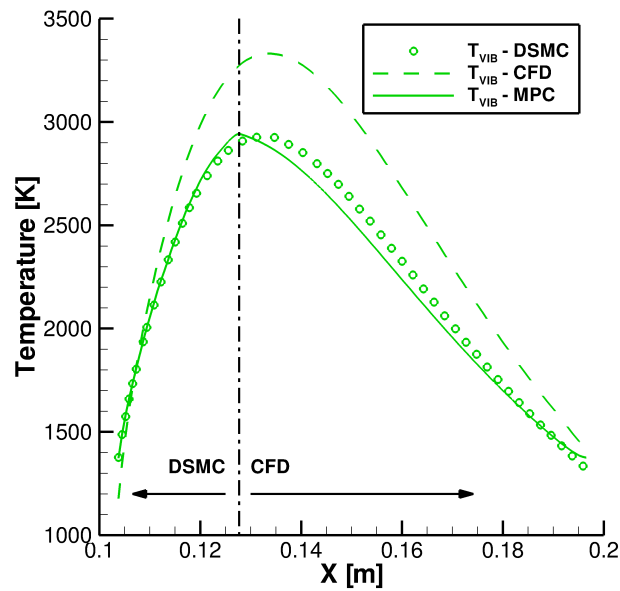
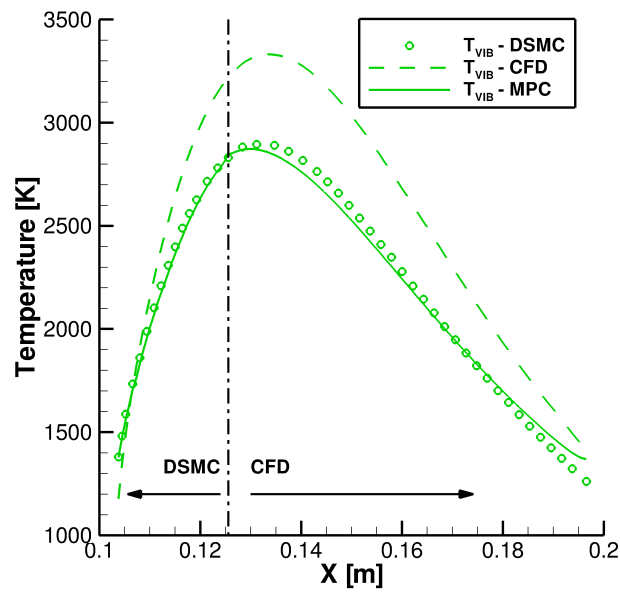
(a) Case **CM15K01<sub>VP</sub>**(b) Case **CM15K01<sub>CB</sub>**

Figure 5.11: Comparison of vibrational temperature predicted by full DSMC, full CFD, and the MPC method along the 135° extraction line using different vibration-translation relaxation models in the DSMC method

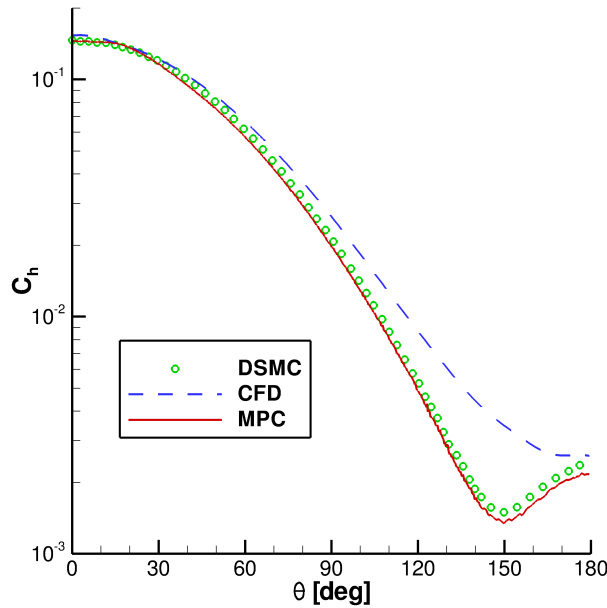


Figure 5.12: Comparison of heat transfer to the cylinder surface predicted by full DSMC, full CFD, and the MPC method for the **CM15K01<sub>VP</sub>** case.

transfer predictions shown in Chapter IV, the MPC method is able to reproduce the full DSMC results, especially in the wake region where the full CFD results over predict the heat transfer to the body by a factor of three compared to full DSMC predictions. It is interesting to note that the contribution of heat flux directly from vibrational energy is negligible compared to the total surface heat flux. This is due to the relatively small gradients of the partially activated vibrational energy mode at the surface and the small coefficient of conductivity. However, inclusion of vibrational excitation acts to significantly decrease the heat transfer associated with translational and rotational energy modes by a reduction in the post shock temperature and temperature gradients near the fore-body vehicle surface.

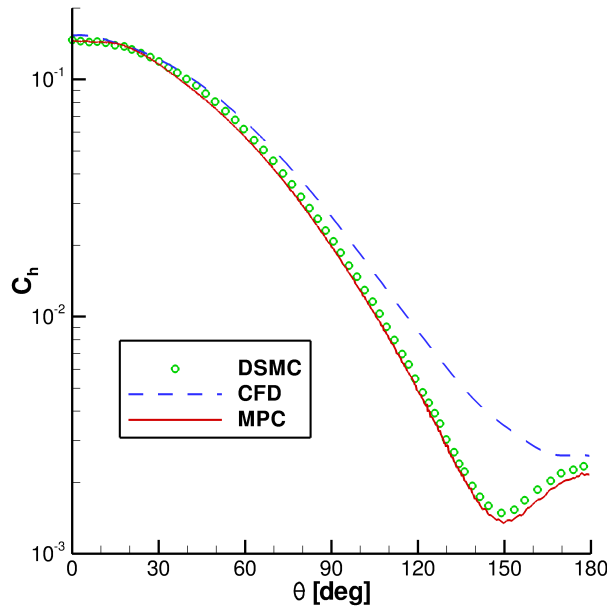


Figure 5.13: Comparison heat transfer to the cylinder surface predicted by full DSMC, full CFD, and the MPC method for the **CM15K01<sub>CB</sub>** case.

### Computational Performance

The MPC method reproduces full DSMC results by employing the DSMC module in rarefied regions and decreases the computational cost by limiting the DSMC method to *only* regions that are in collisional nonequilibrium, while continuum regions are computed using an implicit Navier-Stokes solver. By loosely coupling the simulation methods and studying steady-state flows, the time-step used by CFD can be over 100 times larger than the time-step required by the DSMC module to simulate Mach 15 flow over a two-dimensional cylinder. In addition, decoupling of the mesh densities allows the CFD mesh to be unconstrained by DSMC cell size restrictions, and the CFD module uses mesh densities that are up to 18 times larger in area than the DSMC cells for the two cases. This significantly decreases the computational time and memory usage required by the MPC method to reproduce full DSMC

results. The decreases in computational cost of the MPC method compared to full DSMC for the two cases are summarized in Table 5.1. To make a fair comparison, the number of sample time-steps after reaching steady-state are the same for both the full DSMC simulation and the corresponding MPC simulation. Here, the actual speedup is defined as the ratio of the time required to obtain the full DSMC results to the time required for the corresponding MPC simulation. The ideal speedup is defined as the ratio of the number of particles used in a full DSMC simulation to the number of particles in the corresponding MPC simulation. Since the computational cost of a DSMC simulation nearly scales linearly with the number of particles in the simulation, this should be the upper limit for computational speedup for that problem. Again, the MPC method actually outperforms the ideal speedup ratio because the unsteady portion of the MPC simulation is much less than that of the corresponding DSMC simulation. Similar to the computational requirements shown in Chapter IV, this is because the MPC method initializes its simulation with a full CFD prediction. The memory usage is defined as the ratio of the memory used by an MPC simulation to the memory used by the corresponding DSMC simulation. Here, the MPC method requires significantly less memory compared to the corresponding full DSMC simulation. In addition, the actual speedup for the cell based relaxation case significantly outperforms the variable probability case. This is, in part, due to a slight reduction in the size of the DSMC region, but mostly can be attributed to a decrease in the number of iterations required to reach steady state since the initial CFD solution that the MPC method starts with is in better agreement with the final MPC and full DSMC predictions.

Table 5.1: Computational performance and memory requirements for the MPC method.

Case	Actual Speedup	Ideal Speedup	Memory Usage
<b>CM15K01<sub>VP</sub></b>	3.37	3.07	22%
<b>CM15K01<sub>CB</sub></b>	3.96	3.16	27%

## 5.4 Summary and Conclusions from Effects of Vibrational Nonequilibrium

The MPC method has been extended to simulate partially rarefied, hypersonic flows that exhibit vibrationally excited energy modes that may not be in equilibrium with the other energy modes. An overview of the mathematical and numerical models necessary to describe the physical processes associated with a vibrationally excited gas have been provided. Comparison of physical relaxation models in each simulation module has been performed and changes to the MPC method to accommodate the inclusion of vibrational energy nonequilibrium have been implemented. The implementation of vibrational nonequilibrium models has been verified by comparing MPC simulation results to predictions from full DSMC simulations. In addition, the study of the effect of the consistency of vibrational relaxation models used in rarefied and continuum models on the agreement between full DSMC and the MPC method has been performed.

Three important conclusions can be drawn from the implementation and study of the effects of vibrational nonequilibrium in the MPC method.

1. An implementation of a separate vibrational energy equation within the continuum module can be coupled to a DSMC module within the MPC method.

For the case studied, the use of vibration-translation relaxation models in each module that remain consistent at the continuum limit provide a small improve-

ment between predictions made by the full DSMC and the MPC simulations. In addition, the MPC simulation with the cell-based vibration-translation relaxation model provides a larger speedup over the corresponding full DSMC simulation. In part, this is due to a slight decrease in the size of the region to which the DSMC module is applied, but mostly has been attributed to a decrease in the number of iterations that the MPC simulation requires to reach steady state.

2. Care must be taken to minimize the effect of the statistical scatter of sampling the discrete Boltzmann probability density function for vibrational energy at low temperatures on the physical accuracy and numerical efficiency of the MPC method. In regions of flow where the vibrational temperature is much less than the characteristic temperature of vibration, such as in the free stream, the probability of a particle having an excited vibrational state is very low and a prohibitive number of samples are required to resolve the correct vibrational temperature. Instead of assigning particle vibrational energies by sampling the discrete Boltzmann vibrational energy probability density function, average vibrational energies are assigned to each particle in the computational cell. The effect of this simplification is tested through comparison of MPC predictions with full DSMC results and has no noticeable effect on the agreement between simulation predictions.
3. The order of operations used in the scatter reduction techniques of the MPC method has a strong impact on the computation of boundary conditions provided by the DSMC module to the continuum module. Unlike the temperature associated with other energy modes, the relation between vibrational energy

and temperature is highly nonlinear and can amplify the statistical scatter associated with moderate to low vibrational temperatures to produce a random walk error. In order to reduce this effect, the subrelaxation procedure is applied to the average vibrational energies, rather than the computed vibrational temperature. Then, a vibrational temperature is computed using the subrelaxation-averaged vibrational energy.

## CHAPTER VI

# Extension of Computational Capabilities

The computational requirements of each separate flow module, even for two-dimensional flows, often become too demanding to maintain an acceptable level of physical and numerical accuracy while obtaining a solution in a reasonable amount of time on a serial processor. In addition, many partially rarefied, hypersonic flows of interest contain three dimensional effects that are important. Although most aeroshells are axi-symmetric, they often fly at an angle of attack to induce a positive lift-to-drag ratio which decreases the peak heat flux and acceleration. In addition, reaction control system (RCS) jets used to control aero-shells during re-entry are often located off axis, and accurate simulation of the jet interactions with the nearby flow are of interest to predict the correct heating on the adjacent vehicle surfaces. Other three-dimensional flows of interest occur around hypersonic cruise vehicles and high density jets expanding around space vehicles with complex three-dimensional geometries at near-vacuum conditions. An efficient parallel algorithm enables simulation of these flows that can not be computed using serial algorithms with reasonable processor memory requirements and/or wall clock times. Careful consideration must be taken to ensure that a parallel implementation of the MPC method maintains both a high level of physical accuracy and efficiency. In addition to reducing the

necessary wall clock time, these parallel operations also significantly reduce the required amount of memory for each single processor since only a small portion of the computational mesh and solution is stored on each processor.

With a modular implementation of a coupled hybrid method, such as the MPC method, where both DSMC and CFD separate data structures are maintained and an MPC data structure is used to minimize the number of modifications of each flow module, parallelization becomes an enabling feature for flow simulations that require large computational grids and expensive physical models. This chapter outlines the extension of the MPC method to simulate partially rarefied, hypersonic flows for use on distributed memory parallel computing clusters. First, an outline of the changes to the MPC method is described that ensures that the parallel implementation achieves a high level of numerical efficiency within the modular framework. This includes changes to the hybrid data structure and routines that take into account the existing parallel implementations in each flow module, minimize the number of code changes in each flow module, and maintain an acceptably low level for processor memory requirements. The parallel implementation is verified by applying the parallel MPC method to simulate a selection of flow cases that have been studied in Chapters IV and V. In addition, parallel performance measurements are shown and are compared to the parallel performance of the stand alone DSMC and CFD flow modules.

## 6.1 Modifications to the MPC Method

Both MONACO and LeMANS are parallelized as separate codes using the message passing interface (MPI). Due to the modular nature of the MPC method, all parallelized routines that apply to each module's data structure can be used without modification. Instead, separate functions are provided to perform dynamic domain

decomposition using load balance information consistent with the hybrid framework. First the graph, which is a generic representation of the geometrical mesh connectivity used by partitioning library, is split between parallel processors. Then, hybrid functions provide each module with this information so that each simulation method can perform its normal partitioning routine internal to each code and renumber its local data on each node to be consistent with its existing parallel routines. This procedure maintains the modular nature of the MPC method by reducing the number of modifications in each flow module while still achieving high levels of inter-processor computational load balance of the inhomogeneous simulation that is inherent within a hybrid DSMC-CFD method. Instead, new hybrid functions are developed to reorder the local hybrid data structure to be consistent with the local MONACO and LeMANS data structures and facilitate the dynamic domain decomposition required as the flow evolves and the sizes of the regions simulated with each flow module change.

As described in Chapter III, hybrid functions must access data from both the DSMC and CFD data structures at each time-step and are linked with a hybrid data structure. Algorithm 1 displays the information contained in this hybrid data structure for each cell. As described in Sec. 3.2.4, the cell index for each hybrid structure exactly coincides with the corresponding continuum cell. In addition, the hybrid data structure contains two particle indices, labeled as the integers  $\text{PiB}$  and  $\text{PiE}$ , which correspond to the beginning and ending particle indices for the corresponding DSMC cells, respectively. The particle cells that are contained within the continuum cell are always kept consecutively within the DSMC data structure to simplify the data structure and as a result of the procedures that perform the mesh refinement and DSMC mesh creation. Since the hybrid data structure requires many accesses

---

**Algorithm 1** HybridDataStructure

---

```

structure HCDATA
    ▷ HCdata goes 0 to NScells
    ▷ 1 to NScells contains data
    ▷ HCdata[0] is used as a buffer

5:   bool DSMC
    bool CFD
    bool BC

    int PiB           ▷ First (Beginning) Particle index)
10:  int PiE           ▷ Last (Ending) Particle index)
    int refine[2]      ▷ refinement in each direction
                        ▷ (PiE-PiB=refine[1]*refine[2])

    double Pmacro[NS+ND+NE][3]
15:           ▷ subrelaxation average of macroscopic variables
        ▷ at current and previous time-step and previous correction

end structure

```

---

to both corresponding continuum and particle data structures at each iteration, it is ideal to keep all information corresponding to a given cell on the same processor to reduce the hybrid inter-processor communication and complexity of the parallel implementation. Therefore, the hybrid partitioning procedures and parallel routines ensure that all information corresponding to a physical location in space is kept on the same processor. Schematically, this partitioning method will result in partition cuts along horizontal lines in the schematic of the serial (total) data structure which was shown in Fig. 3.11. Since the hybrid data structure and cells correspond one to one with the continuum data structure, many of the routines used to perform domain decomposition within the continuum module can be reused. However, the computational load for each cell in the MPC method is very different from the continuum computational load. Due to the loosely-coupled nature of the MPC method, switches between each flow module are performed relatively infrequently ( $\sim$  once every  $10^3$  iterations). In addition, the switch between flow modules often coincides with a

re-application of the breakdown parameter which results in a change in the sizes of the regions that are simulated with each flow module. Therefore, dynamic domain decomposition is performed before each module switch, and the mesh is partitioned to optimize the performance for the proceeding module simulation.

An outline of the cycle employed in the parallel implementation of the MPC method is as follows with additions from the serial routine in bold:

1. Load a grid-independent, full Navier-Stokes solution on a structured mesh. Use the continuum breakdown parameter (Eq. 3.8) to set up initial interface locations. Create overlap regions into the initial continuum domain. Create a DSMC grid by refining the CFD grid to meet local cell size restrictions using the initial continuum result and Eq. 3.11. Generate particles inside the DSMC domain and overlap regions. **Save and output the solution.**
2. **Repartition the computational mesh using DSMC computational load information**
3. In particle boundary cells, destroy all old particles and create new DSMC particles based on Navier-Stokes information in corresponding cells. Sample particle thermal velocities from the Chapman-Enskog velocity distribution function and particle internal energies from Boltzmann energy distribution functions. Cycle through the DSMC solver for one time-step. Update hybrid macroscopic quantities using the subrelaxation approach (Eq. 3.18). Repeat a prescribed number of times (typically  $1/\Phi + 10$  iterations).
4. Re-evaluate the breakdown parameter; if needed, move interfaces, create particles in new DSMC cells, and destroy particles in newly labeled pure continuum cells.

*IF* Interfaces have significantly changed (number of DSMC cells increases by more than a user specified percentage), save and output the solution, **repartition the computational mesh using DSMC computational load information** and go to step 2.

*ELSE* Save and output the solution, **repartition the computational mesh using CFD computational load information** and update the Navier-Stokes boundary cells with the subrelaxation averages and continue.

5. Cycle through the Navier-Stokes solver. Repeat until converged to a user specified tolerance.

6. Re-evaluate the breakdown parameter; if needed, move interfaces, create particles in new DSMC cells, and destroy particles in newly labeled pure continuum cells.

*IF* Interfaces have significantly changed or steady-state has not been reached, save and output the solution, **repartition the computational mesh using DSMC computational load information** and go to step 2.

*ELSE* Continue.

7. Remove overlap regions, delete particles in these regions, save and output the solution, and **repartition the computational mesh using DSMC computational load information**.

8. In particle boundary cells, destroy all old particles and create new DSMC particles based on Navier-Stokes information in the cells. Cycle through the DSMC solver. Repeat for a prescribed number of iterations and collect samples.

9. **Save and output the solution and repartition the computational mesh**

---

**using CFD computational load information**

10. Update the Navier-Stokes boundary cells and further converge continuum regions.

*IF* DSMC statistical scatter and Navier-Stokes residual are below user specifications, end.

*ELSE* Save and output the solution, **repartition the computational mesh using DSMC computational load information** and return to step 8.

---

**Algorithm 2** MPC Parallel Pre-processor

---

```

Initialize MONACO variables
Initialize LeMANS variables
Initialize MPC variables
Read and Process CFD Mesh
5: Load CFD solution
    AllocateHybridData()                                ▷ see Algorithm 4 in Ref. [11]

    if (!Restart) then perform serially
        SetupHybridDomains()                           ▷ see Algorithm 5-7 in Ref. [11]
    10: DetermineMeshRefinement()                     ▷ see Algorithm 8 in Ref. [11]
        CreateDSMCMesh()                            ▷ see Algorithm 9 in Ref. [11]

        GenerateParticles()                         ▷ see Algorithm 10, 12 in Ref. [11]
        WriteCompLoadFile()                        ▷ see Algorithm 6
    15: WriteGraphFile()
        Write DSMC and hybrid restart files

    end simulation
    else (Restart) then perform in parallel
    20: PartHybMesh()                               ▷ see Algorithm 4
        LoadHybridRestart()                         ▷ see Algorithm 5
        Load DSMC mesh and particles
    end if
    Begin main loop                                ▷ see Algorithm 2, line 17 in Ref. [11]

```

---

Identical to the serial implementation, Step 1 is performed in serial as a pre-processing routine and is shown in Algorithm 2. In addition to the serial hybrid routines, hybrid

routines that compute and write a graph file necessary for the partitioning library, METIS, and the computational load estimates for the DSMC module are called. After the pre-processor is run in serial, the parallel implementation of the MPC method begins at Step 2 which is shown in the else statement of Algorithm 2. In addition, Algorithm 5 details the portion of the code that is called during each dynamic domain decomposition procedure.

---

**Algorithm 3** Dynamic Domain Decomposition
 

---

```

.
.
.
5: saveNS()                                ▷ save NSdata
5: saveDSMC()                               ▷ save DSMCdata
      saveHyb()                            ▷ save HCdata
      WriteCompLoadFile()                  ▷ see Algorithm 6

      Free All NS, DSMC, HC data

10:
      Read and Process CFD Mesh

      PartMeshHyb()                         ▷ see Algorithm 4
      LoadHybridRestart()                   ▷ see Algorithm 5

15: Load DSMC mesh and particles necessary for each processor
.
.
.
```

---

Algorithm 4 details the implementation of the function, `PartMeshHyb()`, that uses the cell computational load information that is generated using `WriteCompLoadFile()` and the full graph of the continuum mesh as required by the METIS [100] partitioning library. The METIS library provides an array for domain decomposition that maintains uniform computational load across all processors while minimizing the amount of information (cell cuts) between inter processor boundaries. After this data structure is obtained, standard LeMANS routines are used to renumber cells local to each processor and establish the data structures necessary to perform inter

---

**Algorithm 4** PartMeshHyb()

---

```

function PARTMESHHYB(NSdata)

    p=NSdata.p
    weight[NSCells]

5:   if (p==0) then
        for all (Lines of file hybweight.dat) do
            sscanf(hybweight.dat,"cellid celload"
            weight[cellid]=celload
10:  end for

        Load Metis Graph File
        Call Metis
        Broadcast Information to all Processors
15: end if
        Renumber NSdata on Each Processor using LeMANS routines
end function

```

---

processor communication within the continuum routines. Included in these LeMANS routines is the creation of a continuum data structure, `NSdata.whereis[]`, that cross references cell global indices to local cell indices if a cell is located on the current processor, or the processor that contains the cell with the global index. For example on processor *proc*, `NSdata.whereis[gi]=i` while `NSdata.whereis[gi]=-proc` on all other processors other than processor *proc*. A nearly identical data structure exists within the DSMC data structure to cross reference a global DSMC cell index with the corresponding local cell index. These data structures are utilized within the hybrid routines to eliminate much of the renumbering of particle cell indices within the hybrid data structure during dynamic domain decomposition procedures.

After `PartMeshHyb()`, the MPC method calls on each processor the new hybrid function, `LoadHybRestart()`, which is detailed in Algorithm 5. First, the local hybrid data structure is populated from a restart file. Each line of the hybrid restart file corresponds to the entire hybrid data structure for a single cell with a global

index that is consistent with the continuum global indices, which is described in Algorithm 1. If the hybrid cell exists on that processor, the hybrid data is assigned to the index corresponding to the local continuum cell. If the hybrid cell does not exist on that processor, it is assigned to an empty buffer location and kept temporarily only to calculate the correct total number of DSMC cells. After the hybrid data is loaded on each processor, the data structure, `DSMCdata.whereis[]`, is initialized. To maintain consistency with MONACO’s internal cell loading routines, `DSMCdata.whereis[gi]=-proc` where *proc* is the processor on which the cell with global index *gi* is located. This cross reference list is used to correctly load the DSMC mesh structure on each processor and then routines internal to MONACO will renumber `DSMCdata.whereis[]` to match the definition of the corresponding continuum array described above. Since the variables PiB and PiE are not renumbered in the hybrid data structure at each dynamic domain decomposition and always correspond to the global cell index (which *is* the local cell index for a serial process), the `DSMCdata.whereis[]` array along with the hybrid data structure allows proper links between local continuum and local particle cells.

Since the domain decomposition routine is performed between each module switch, the computational load of each cell only requires comparison to the computational load of other cells using the current flow module and cross-module computational comparisons are unnecessary. In other words, the computational load of a continuum calculation of a cell does not have to be accurately modeled relative to the computational cost of the DSMC routines within the corresponding particle cells. Algorithm 6 details the implementation of the hybrid function, `WriteCompLoadFile()`, that estimates the computational load of each continuum (hybrid) level cell to be optimized for the proceeding simulation method. Schematics of the computational load

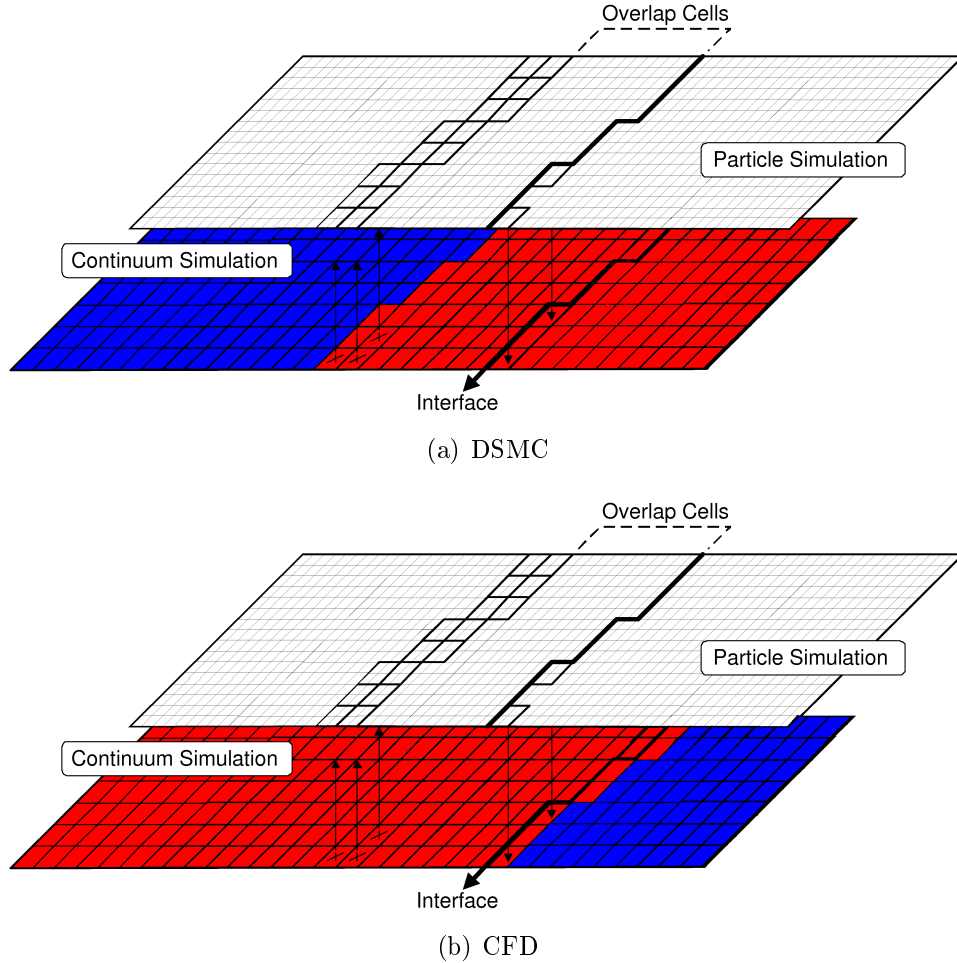


Figure 6.1: Schematic of cell load estimation supplied to METIS depending on the proceeding module call

estimates based on the proceeding module routine are shown in Fig. 6.1. Figure 6.1(a) shows how computational load estimates are computed when MONACO is the proceeding module call. Here, red cells have a computational load estimate proportional to the average number of particles in each continuum sized cell (sum of average number of particles in all DSMC cells), while blue cells are set to have zero computational load. In contrast, Fig. 6.1(b) shows a schematic of the computational load estimates when LeMANS is the proceeding module call in the MPC method. Now, red cells are located throughout the continuum and overlap region with a computational load estimate of unity, while blue cells (in pure DSMC regions) have a

computational load of zero.

---

**Algorithm 5** LoadHybRestart()

---

```

function LOADHYBRESTART(NSdata, HCdata, DSMCdata, totalDSMCcells)
    totalDSMCcells=0
    proc=NSdata.p                                ▷ Current processor
    5:   for all (Lines of file hybridrestart.dat) do
        fscanf(hybridrestart.dat,"globalid")
        if (NSdata.whereis[globalid]>0) then
            ▷ Check if cell is on current processor
        10:  i=NSdata.whereis[globalid]           ▷ Set local cell index
            else
                i=0                               ▷ Cell does not reside on partition
                ▷ use buffer to calculate correct number of DSMC cells
            end if
        15:  Load HCdata[i]                      ▷ Entire HCdata as described in Algorithm 1
            totalDSMCcells+=HCdata[i].refine[0]*HCdata[i].refine[1]
        end for

                ▷ Now set whereis so that DSMC data is properly loaded
    20:  DSMCdata.whereis[totalDSMCcells]          ▷ Initialization

        for all (Lines of file hybridrestart.dat) do
            fscanf(hybridrestart.dat,"globalid")
            i=0
        25:  Load HCdata[i]                      ▷ Entire HCdata as described in Algorithm 1
            for all p = HCdata[i].PiB to HCdata[i].PiE do
                ▷ cell is on another processor
                if NSdata.whereis[globalid]<=0 then
                    DSMCdata.whereis[p]=NSdata.whereis[globalid]
                30:  else                                ▷ cell is on this processor
                    DSMCdata.whereis[p]=-proc
                end if
            end for
        end for
    35: end function

```

---

---

**Algorithm 6** WriteCompLoadFile

---

```

function WRITECOMPLLOADFILE(NSdata, HCdata, DSMCdata, DSMCNext)

    CellLoad[NScells]
    p=NSData.p
    5:
        for all (NScells, i) do
            DSMC=HCdata[i].dsmc
            CFD=HCdata[i].cf
            BC=HCdata[i].bc
    10:
        if (DSMCNext) then
            LoadPerCell=0
            for all p = HCdata[i].PiB to HCdata[i].PiE do
                plocal=whereis[p]-1
    15:
                for all (Species, s) do
                    ObjPerCell=(int)(DSMCdata[plocal].avenobj+0.5)
                    LoadFactor=(int)(MIN(DSMC+BC,1))
                    LoadPerCell+=ObjPerCell*LoadFactor
                end for
            end for
    20:
            else (!DSMCNext)
                LoadPerCell=CFD+MAX(BC-CFD,0)
            end if
            gi=NSData[i].globalid
    25:
                fprintf(hybweight.p.dat,"gi LoadPerCell")
            end for
            call MPIWall
            if (p==0) then
                Concatenate multiple hybweight files to one
    30:   end if
        end function

```

---

## 6.2 Verification

Figure 6.2 illustrates that the parallel implementation of the MPC method is performed correctly. Here, the parallel MPC method is applied to case **M12K002**, which was described in Sec. 4.3, using 32 processors during the DSMC portion of the simulation. Both inter processor edges and the CFD-DSMC interface are shown. All partitions are clustered in the near wake region where the DSMC particles are located while the entire continuum region is appended to one partition. In addition, translational temperature contours are displayed and no jumps are visible across processor or rarefied-continuum interface locations for all macroscopic quantities which demonstrates that the correct information transfer routines in both flow libraries are still working as intended.

Figure 6.3 shows an example of the instantaneous number of particles located on each processor normalized by the average number of particles on each processor. The number of particles in a cell is approximately linearly related to the computational time required to apply the DSMC method to each cell. The partitioning routines maintain a high level of computational load balance, with less than a 2.5% variation between extrema and mean values.

## 6.3 Parallel Performance

Parallel performance studies are conducted using cases **M12K002** and **M15K01<sub>CB</sub>** that were described in Sec. 4.3 and 5.3, respectively. These two test cases are chosen to cover the wide range of applicable flow conditions relevant to the MPC method. Approximately 8 and 6.25 million particles are simulated in the DSMC regions at steady-state and the total continuum meshes consisted of 30,000 and 45,000 for cases **M15K01<sub>CB</sub>** and **M12K002**, respectively.

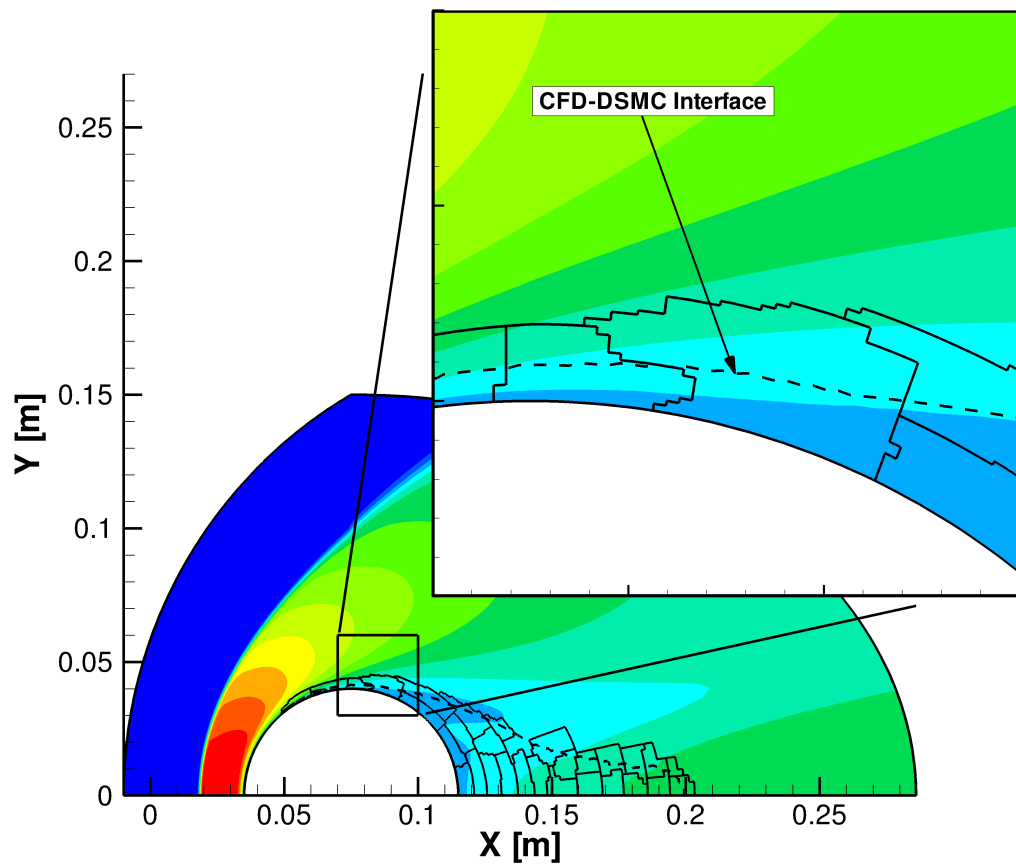


Figure 6.2: Temperature contours and processor domain boundaries for a DSMC module call during steady state

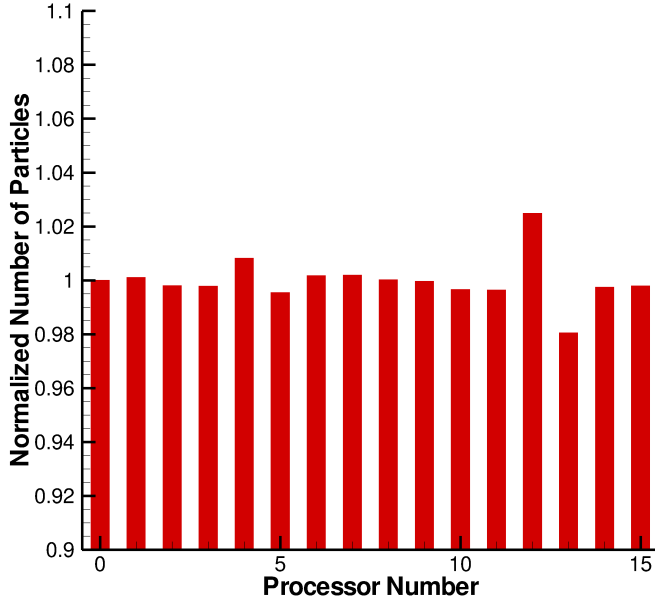
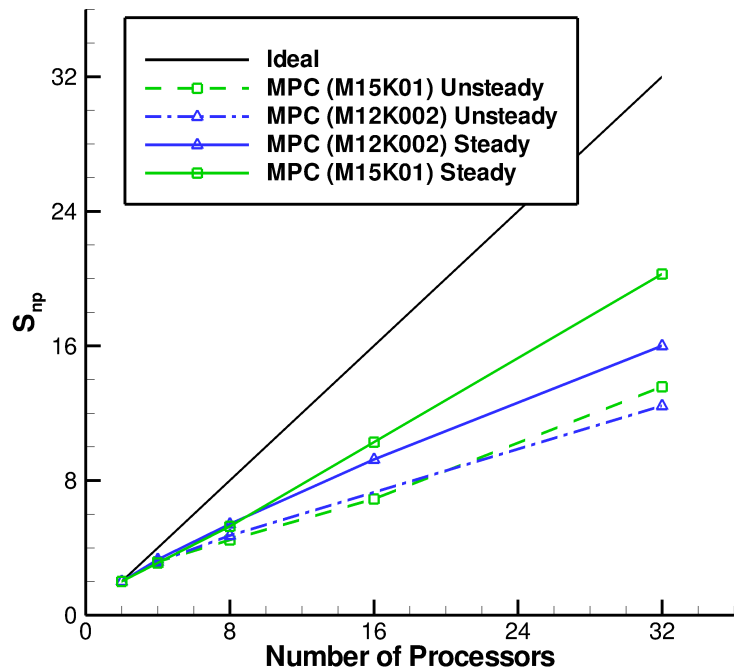
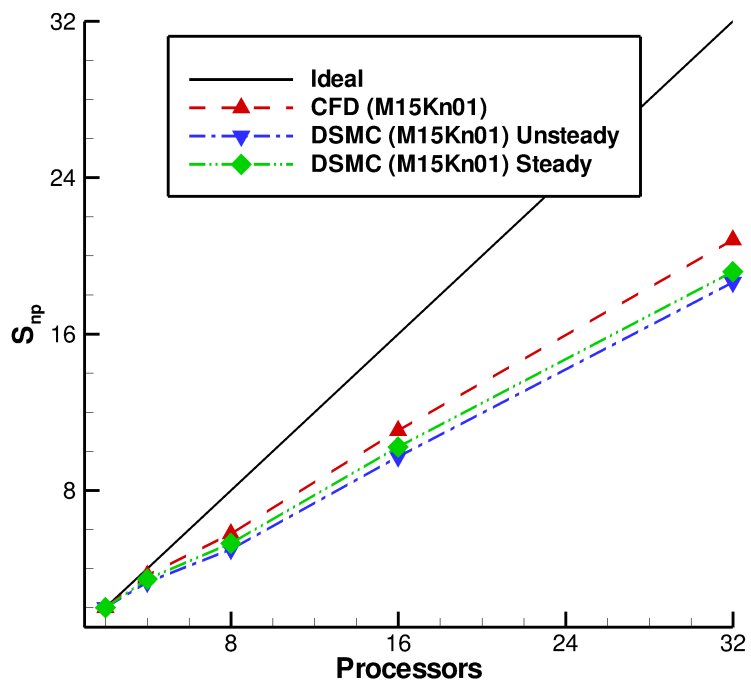


Figure 6.3: Normalized number of DSMC particles per processor for parallel implementation of the MPC method on 16 processors

Figure 6.4(a) shows a plot of the parallel speed up,  $S_{np}$ , for the two cases examined for both the unsteady portion and the steady state portion of the MPC simulations. For reference, the parallel speedup for the full DSMC and CFD simulation methods are shown in Fig. 6.4(b). These parallel performance test cases are performed on the RTJones cluster of the NASA Supercomputing (NAS) Division. One node corresponds to 2 quad-core Xeon (Harpertown) processors with a total of 8GB of memory available on each node. The nodes are connected with an InfiniBand interconnect and data storage is maintained on a Lustre file system. The parallel speedup is defined as the ratio of the estimated wall time for a serial simulation to the wall time of a simulation on  $np$  processors and is shown in Eq. 6.1 where  $T_s$  is the wall time for a serial calculation and  $T_{np}$  is the wall time for a simulation on  $np$



(a) MPC



(b) MONACO, LeMANS

Figure 6.4: Parallel speedup (fixed problem size)

processors.

$$S_{np} = \frac{T_s}{T_{np}} \quad (6.1)$$

Both cases show a higher speedup during the steady portion compared to the unsteady portion. This is due to increased variation in the total number of simulation particles during the unsteady portion of the computation which necessitates the overhead of a larger number of dynamic domain decomposition calls. At steady state, the total number of particles on each processor remains nearly constant. The speedup for all cases begins to deviate from the ideal speedup as the number of processors increase. Despite this deviation, near linear speedup is still experienced. In addition, the higher Knudsen number case achieves a higher speedup in nearly all tests due to the larger rarefied region which increases the total number of particles, and therefore total computational requirements to simulate the flow. When compared to the full CFD and full DSMC parallel speedups for the **M15K01<sub>CB</sub>** case, it is clear that the parallel implementation of the MPC method does not significantly increase the overhead of the existing parallel routines and similar speedups are obtained.

It should be noted that the two cases used for this study do not require a large computational expense and the time used for inter-processor communication begins to dominate when using very few processors. Approximately 8 and 6.25 million particles are simulated in the DSMC regions at steady-state and the total continuum meshes consisted of 30,000 and 45,000 for cases **M15K01<sub>CB</sub>** and **M12K002**, respectively. In addition, the main goal of the parallelization of the code is to simulate larger problems in about the same amount of time. Simulations that require larger computational requirements, such as three-dimensional simulations, will display a speedup curve that stays closer to the ideal curve longer and may not even be feasible to perform on one processor due to memory constraints. This effect can be

seen in Fig. 6.5 where the computational expense of case **M12K002** is expanded by increasing the number of DSMC simulation particles which is performed by decreasing the numerical weight of each DSMC simulator. Using this information, a scaled efficiency can be estimated which is defined in Eq. 6.2 where  $\eta_S(pn, p)$  is the scaled efficiency of doing  $pn$  computational work on  $p$  processors and  $t_{pn}$  is the wall time required to perform  $pn$  computational work on  $p$  processors.

$$\eta_S(n, p) = \frac{qt_{qn}}{pt_{pn}} \quad (6.2)$$

For these cases, the wall times are normalized with the wall time required for an 8 processor (1 full node) computational case, such that  $q = 8$ . Doubling and quadrupling the computational load of the DSMC module and the available computational resources require less than 7% and 17% more wall time, respectively. This parallel scaling is a more relevant metric quantity and the results show that future extension of the MPC method for simulation of complicated three-dimensional flows that require large computational resources can take advantage of this parallel implementation.

Additional parallel simulations are performed to test the scaling over a larger number of processors (greater than 100). As demonstrated in Fig. 6.5, efficient simulation over at larger number of processors requires test cases that involve a large total computational cost. This is necessary to ensure that the time needed for inter-processor communication remains small compared to the time required for each processor to perform its calculations. Simulation of a planar shock wave is chosen to test the parallel scaling over a large number of processors. A baseline simulation is constructed with 1.2 million ( $1,200 \times 1,000$ ) continuum cells with a constant cell size of half of the free stream mean free path. The DSMC mesh used within the

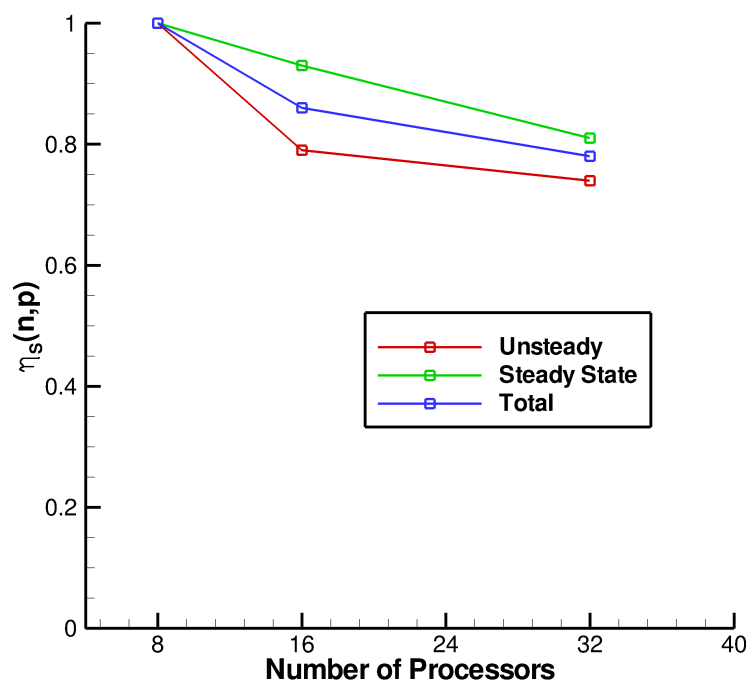


Figure 6.5: Scaled efficiency of the MPC method (problem size scaled with number of processors)

MPC method is created by constantly refining the continuum mesh by a factor of two in each direction which results in 4.8 million DSMC cells. The DSMC region within the shock interior is sufficiently large to require nearly 190 million particles. The pre-shock flow conditions were set to match those of case **CM12K01** described in Sec. 4.3.1. Although still two-dimensional, the computational cost of this test case is comparable to the estimated computational cost of an MPC simulation of a simple three-dimensional case. The parallel performance is measured on the Pleiades supercomputer within the NAS Division. A single node contains two hexa-core Xeon (Westmere) processors with a total of 24GB of RAM available on each node. Identical interconnect and file storage systems to the RTJones system described above are used.

The parallel speedup, where the size of the problem remains constant as the number of processors change and is defined in Eq. 6.1, of the MPC method is shown in Fig. 6.6. Here, the serial wall time is estimated from the simulation on the smallest number of processors ( $np = 60$ ). It is clear that the MPC method can slightly exceed the ideal speedup when the number of processors is increased from 60 to 120, however the speedup remains less than ideal as the number of processors is further increased. As with the previous test case, this is because the time required for inter-processor communication begins to dominate the total simulation time when the simulation is applied to too many processors. The scaled efficiency, as defined by Eq. 6.2, is also measured where the computational size of the problem is scaled with the number of processors and is shown in Fig. 6.6. Here, the total number of continuum and rarefied cells and the number of DSMC simulators is scaled from the baseline simulation procedure with the number of processors (halved, doubled, and tripled for 60, 240, and 360 processors, respectively). Now, the scaled efficiency is normalized

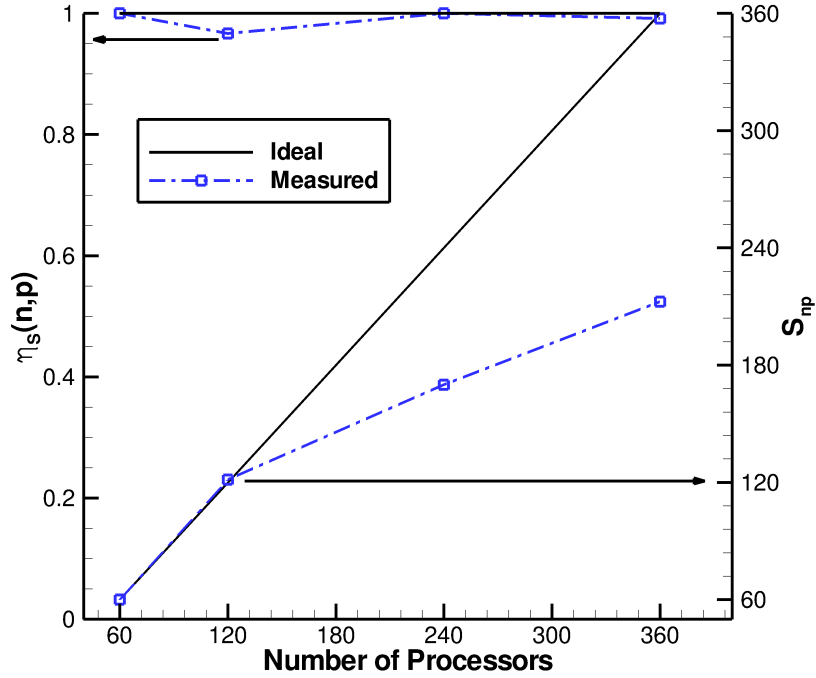


Figure 6.6: Parallel speedup and scaled efficiency of the MPC method when applied to a problem with comparable computational cost of a three-dimensional simulation

by the wall time required by a 60 processor (5 nodes) simulation and maintains near ideal scaled efficiency up to 360 processors (greater than 500 million simulators).

## 6.4 Three-Dimensional Implementation

Although the MPC method has not yet been fully implemented to simulate three-dimensional flows, the parallelization techniques and the modular implementation are expected to be advantageous for this future extension. The algorithms adopted in this parallel implementation have been selected to minimize each processor's memory requirement by eliminating the need to load the entire DSMC mesh on each processor. Instead, only the portion that is applicable to that processor is loaded. In addition, the measurement of the parallel scaling parameters shown in this chapter

demonstrate that application of more processors to larger computational problems, which is necessary for simulation of three-dimensional flows, can be performed in an efficient manner to maintain an acceptable level of wall clock time.

In addition, many of the hybrid routines naturally loop over all available dimensions for the necessary sampling of dimensional quantities such as velocity components, shear stress tensor, and heat flux vector so that very few modifications of the hybrid routines will be necessary. One major consideration is how MONACO treats three-dimensional flows which is not in a modular fashion and requires large changes to the DSMC data structures. These changes either have to be taken into account in the hybrid data structure, or changes to the DSMC data structure must be made to increase its modularity as the number of simulation dimensions increases from two to three.

Thus, although the MPC method is only presently capable of simulating two-dimensional or axi-symmetric flows, the parallel implementation adopted in this dissertation and the modular nature of the hybrid method will be highly beneficial to extend the MPC method for simulation of full three-dimensional flows. The parallel implementation described in this dissertation will enable the next extension by reducing the computational size of problems applied to each processor.

## **6.5 Summary and Conclusions from Extension of Computational Capabilities**

The computational capabilities of the MPC code have been extended by parallelizing the method to be capable of simulation of flows using distributed memory computing clusters. An overview of the parallel implementation of the MPC method has been described including the addition of hybrid routines and modifications to

the hybrid data structures that take advantage of and maintain the high level of modularity that exists in the MPC method. The parallel implementation has been verified to produce simulation results that are independent of the parallel partition lines and maintain uniform load balance of the inhomogeneous data structure and simulation requirements. Parallel scaling parameters for two simple cases have been examined. Although ideal scaling is only achieved at small numbers of processors, the parallel speedup remains linear and is comparable to parallel scaling performance experienced by each separate flow module applied to a similar flow. Scaled efficiency measurements to test application of larger computational resources to larger computational problems maintained high levels of efficiency. The parallel scaling of the MPC method is tested over a large number ( $\sim 100$ ) processors. These scaling measurements demonstrate that for cases that have sufficient computational cost, which is the case for three-dimensional simulations, the MPC method can maintain high levels of parallel efficiency up to 360 processors. The results demonstrate that the parallel implementation presented in this dissertation is ideally suited for future extension of the MPC method to simulate full three-dimensional flows.

## CHAPTER VII

# Conclusion

This chapter contains a summary of the dissertation and a list of the contributions made to the field. The chapter is concluded with recommendations for future research that will further extend the capabilities of hybrid particle-continuum simulation of nonequilibrium, hypersonic flows.

### 7.1 Summary

This work presents an extension of the Modular Particle-Continuum (MPC) method for simulation of partially-rarefied, hypersonic flows. The overall goal in the development of the MPC method is to reproduce full DSMC results to within 5% at a reduced computational cost for hypersonic flows of interest. These flows require mathematical models to describe important physical processes that readily occur throughout the flow and have an effect on the output quantities of interest. This dissertation has expanded on the work of Schwartzenruber to extend the MPC method to simulate hypersonic flows that exhibit small regions of collisional nonequilibrium and may exhibit thermal nonequilibrium between internal (rotational and/or vibrational) energy modes and the translational mode on distributed memory computing architectures.

Chapter I introduced the thermo-chemical nature of partially rarefied flows over hypersonic vehicles. The chapter cited many sources that provided examples of flows that may require a hybrid particle-continuum method to simulate flow. This is because these flows can be sufficiently described with a macroscopic, or continuum, method over most of the flow, but require a microscopic, or kinetic, description in localized regions. Hybrid methods that achieve the physical accuracy of kinetic methods in rarefied regions, while maintaining the numerical efficiency of continuum methods elsewhere, will become vital tools to analyze future advancements in technology for entry flows. An overview of some causes of collisional, or translational, nonequilibrium was described. In addition to translational nonequilibrium, which occurs when flow length scales are small and/or the mean free path is large, nonequilibrium effects may be present for separate internal energy modes and/or the chemical composition of the flow.

Chapter II detailed the various overall mathematical descriptions available for gas flows, which range from fully kinetic to entirely continuum. These descriptions started with the fundamental Boltzmann equation. Simplification of the flow description was introduced to develop the continuum Navier-Stokes and Euler equations. The validity of each simplifying assumption has been discussed. The chapter also described numerical procedures used for each description of the flow. An outline of the direct simulation Monte Carlo (DSMC) method was provided. Particle movement and collision routines were described and numerical limitations of the simulation method were outlined. Although the DSMC method is physically accurate for any degree of rarefaction, its computational expense significantly increases as the Knudsen number decreases. In contrast, numerical solutions of the Navier-Stokes equations with modern CFD techniques are numerically efficient, but the continuum

approximation to fully define the mathematical description breaks down when the Knudsen number is large. Finally, a review of previous hybrid numerical techniques that have been developed over the past two decades was presented. These various hybrid methods have coupled different descriptions for each flow (deterministic Boltzmann vs DSMC, Euler vs Navier-Stokes) using flux- or state-based coupling procedures to describe various flows of interest that contain a mixture of rarefied and continuum regions.

Chapter III detailed the hybrid, Modular Particle-Continuum (MPC) method that is used in this dissertation. First, descriptions of the numerical continuum, LeMANS, and rarefied, MONACO, flow modules were provided. Next, the existing capabilities of the MPC method, which include calculation of the interface location, geometric mesh construction, and the transfer of information between each flow module, have been outlined. Then, an overview of each extension of the MPC method that are a result of this dissertation were provided, which consisted of inclusion of rotational and vibrational nonequilibrium models in each flow module and parallelization of the numerical method to enable future extension of the method to simulate full three-dimensional flows.

Chapter IV provided a detailed description of inclusion of rotational nonequilibrium models in the MPC method. The chapter began with a summary of the mathematical description of rotational relaxation processes and the implementation of these descriptions in each flow module. Next, an outline of the changes required in the MPC method for inclusion of rotational relaxation were described. These include a study of an additional breakdown parameter to ensure that the continuum module is only applied to regions where the flow is near both collisional equilibrium *and* the rotational energy probability density function can be described with the Boltzmann

probability density function. Finally, the accuracy of the method was assessed by comparison of predictions made by the MPC method to those made with full DSMC and full CFD simulations and all three predictions were compared to available experimental measurements. The MPC predictions maintained excellent agreement with full DSMC simulation results for macroscopic quantities and velocity and rotational energy distribution functions. This excellent agreement has demonstrated that the MPC method can reproduce full DSMC simulation results throughout the entire flow field. Computational performance of the MPC method, compared to full DSMC, was discussed for each simulation. It was shown that the speedup relative to full DSMC simulation time ranged from 1.67 for rarefied flows to over 28 for near continuum flows. In addition, comparison with previous simulation requirements of the MPC method without rotational nonequilibrium capabilities in the continuum flow module demonstrated that inclusion of the capability resulted in an overall speedup of the MPC method.

Chapter V outlined the necessary changes in the MPC method for inclusion of vibrational nonequilibrium models. First, the mathematical description of vibrational relaxation processes was outlined. Then, the chapter described the implementation of vibrational nonequilibrium models in the two flow modules. Available vibration-translational energy relaxation models were compared for a zero dimensional relaxation case. Next, a detailed description of the required changes to the MPC routines to take into account the transfer of vibrational energy was provided. These changes include careful consideration of the information transfer procedure to reduce the effect of statistical scatter associated with the large quantum size of vibrational energy relative to the mean flow energy on the physical accuracy and numerical efficiency of the MPC algorithm. Finally, verification of the implementation of vibrational

nonequilibrium models was performed through comparison with fully kinetic and continuum simulation methods. It was shown that maintaining consistent relaxation models in both flow modules slightly increased the agreement between MPC and full DSMC simulation results with a small reduction in the numerical cost.

Chapter VI outlined the extension of the MPC simulation capabilities to take advantage of available distributed memory systems. This capability is necessary to simulate three-dimensional flows due to the large computational resources requirements. First, modifications to the MPC method were outlined and characterization of computational load parameters required for efficient distribution of the flow domain across parallel processors have been described. A complete description of the algorithms necessary to parallelize the MPC method within the provided modular framework have been provided. The parallel implementation made use of existing routines to avoid modifications to the separate flow module libraries to maintain the highly modular structure of the hybrid method. In addition, verification of the implementation of the parallel routines was performed. The results demonstrated that the routines maintain effective distribution of the computational load for parallel computation on distributed memory computing architectures. The parallel performance of the MPC method was described and compared with the performance of each separate flow module. Although far from ideal for the small test cases, the parallel implementation maintained linear speedup scaling even as the computational load per processor became negligible compared to the inter-processor communication and displayed similar parallel speedup characteristics as each separate flow module. Scaled efficiency measurements, where the problem size scales with the number of processors, demonstrated that the parallel implementation of the MPC method is well suited to simulate larger computational problems, which is necessary for future

simulation of three-dimensional flows over complex vehicle geometries that are in full thermo-chemical nonequilibrium.

## 7.2 Contributions

Over the past two decades, many researchers have proposed hybrid particle-continuum methods with two way coupling to simulate partially rarefied, hypersonic flows. However, almost all previous studies have used the simplified, perfect gas physics models within the continuum module. This dissertation uses the Modular Particle-Continuum, first developed by Schwartzenruber [11], and extends this method to include physical models that are important for hypersonic, nonequilibrium flows, such as rotational and/or vibrational energy nonequilibrium, and increases its computational capabilities to perform numerically expensive simulations on distributed memory computing systems. This dissertation adds several distinct contributions to extend the state of the art capabilities of hybrid particle-continuum simulation methods. These contributions are described in Refs. [101, 75, 6, 102, 103, 84, 48] and summarized in this section.

1. Increase of the physical accuracy of the MPC method
  - (a) This dissertation clearly demonstrates that inclusion of a separate rotational energy equation within the continuum module is possible and enables *all* macroscopic results predicted by the MPC method to be in agreement with DSMC results over the entire flow field. Previously, discrepancies in predicted rotational temperature contours existed between the MPC method and full DSMC in expansion regions of the flow. This is because the continuum module did not contain sufficient accuracy to

describe the thermal nonequilibrium associated with a nearly frozen rotational energy mode. In addition, this dissertation has introduced a new rotational nonequilibrium cut off parameter to ensure that strong rotational energy relaxation processes are simulated with the DSMC module in order to avoid introducing physical inconsistencies.

- (b) For the first time, this dissertation provides detailed comparison of velocity *and* rotational energy probability density functions predicted by the MPC method, full DSMC, and full CFD. The excellent agreement between MPC and full DSMC predictions demonstrates that the form of the breakdown parameter and the breakdown cutoff value used in this dissertation are sufficient to ensure that only regions where the continuum approximation is valid are simulated with the CFD module. In addition, the agreement verifies that the coupling procedures used to assign particle velocities and rotational energy are effective.
- (c) This dissertation demonstrates that inclusion of a separate vibrational energy equation within the continuum module and excited vibrational energy levels in the particle module allows the MPC method to simulate a vibrational energy mode that may not be in equilibrium with the translational energy mode. Care must be taken to minimize the effect of the statistical scatter associated with low vibrational temperatures on the physical accuracy and numerical efficiency of the MPC method. This dissertation has provided modified coupling routines to assign vibrational energies to DSMC simulation particles that allow predictions made by the MPC method to maintain high levels of agreement with full DSMC simulation results.

(d) Unique to this dissertation, a comparison of the effect of vibrational relaxation rates used in the DSMC module on agreement between MPC and full DSMC predictions has been made. For the cases studied, the use of vibrational relaxation rates in each module that remain consistent at the continuum limit provided a small improvement in agreement of predictions made by the full DSMC and the MPC simulations. In addition, the MPC simulation with more consistent relaxation rates provided a larger speedup over the corresponding full DSMC simulation. In part, this is due to a slight decrease in the size of the DSMC region, but is mostly attributed to a decrease in the number of iterations that the MPC simulation requires to reach steady state.

## 2. Increase of the computational capabilities of the MPC method

(a) With the inclusion of rotational nonequilibrium modeling capabilities, the computational cost of the MPC method has been reduced. The computational savings from reduction in the size of the DSMC region and the number of iterations required to reach steady-state has outweighed the overhead of solving an additional conservation equation in the continuum method that has resulted in a reduction of computational resources required by the MPC method of 5% for rarefied flows to 62% for near continuum blunt body flows.

(b) This dissertation presents a novel way to perform the parallel implementation within the modular framework that allows each flow solver to use its existing, unmodified parallel routines. In addition, new hybrid routines maintain a high level of computational load balance across all processors

as the size of each region (and the computational load of each flow module) changes significantly. Although far from ideal, this dissertation has demonstrated that the parallel implementation presented herein maintains linear scaling even when the size of computational work performed by each processor becomes very small. In addition, application of the parallel implementation to larger problems that scale with the available resources results in less than a 5% increase in wall clock time for up to 240 processors. This parallel implementation will enable future extension of the MPC method to simulate full three-dimensional flows.

### 7.3 Future Work

Extensions of the MPC method that are a result of this dissertation provide a solid foundation on which to further investigate partially rarefied, hypersonic flows and extend the computational and physical capabilities of the MPC method. These include additional extensions of the physical models within the MPC method, such as extension to simulate three-dimensional flows and inclusion of multi-species with finite rate chemistry. Extensions of the numerical capabilities include additional generalization of the mesh structures used in each of the flow modules and further study of the prediction of continuum breakdown to demarcate the regions simulated with each flow module. As demonstrated in previous works and this dissertation, application of the MPC method is ideal to study the effect of highly localized nonequilibrium regions in flows for which the application of the DSMC method would be computationally prohibitive.

### 7.3.1 Extension for Simulation of Three-Dimensional Flows

Many partially rarefied, hypersonic flows that are of interest are inherently three-dimensional in nature. Even for vehicles, such as capsules, that are geometrically axi-symmetric, they often fly at an angle of attack or use off axis thrusters that create three-dimensional flows. Furthermore, the local flow conditions around these jets can create a local maximum in surface heat transfer to the vehicle that drives the design decision of material selection for the thermal protection system. In addition, the computational cost of three-dimensional DSMC simulations may require a prohibitive number of cells and enormous computational resources to maintain sufficient resolution of the collision length scales (cells refined to the mean free path,  $\lambda$ , in each direction) especially for flows that involve large variations of  $\lambda$  across one flow field. Because of this, these flows may demonstrate the largest savings of numerical cost for a hybrid particle-continuum method over full DSMC simulations. The modular nature of the parallel implementation of the MPC method that was described in Chapter VI will enable future extension of the MPC method to be capable of full three-dimensional simulations.

### 7.3.2 Chemistry

As seen with the inclusion of rotational and vibrational energy nonequilibrium within the MPC method, the use of additional physical models within a hybrid particle-continuum code may require extra considerations to maintain a high level of physical accuracy. Although both flow modules already contain numerical routines to model the finite-rate chemical reaction processes, they may or may not agree at the continuum limit. In addition, very few studies of the effect of dissociation [76, 104] and ionization on continuum breakdown have been performed. Among

other unknown difficulties, the mitigation of the statistical scatter associated with trace species may be necessary. The use of separate numerical particle weights for trace species may reduce the effect of statistical scatter. In addition, many of the chemistry models available in either simulation method are phenomenological and were developed by extrapolating experimental measurements that contained large uncertainty. Further development of new thermo-chemistry models in each simulation technique that provide a better description of the important physical process will also increase the physical accuracy and predictive capabilities of the MPC method.

### **7.3.3 Mesh Type and Refinement**

The mesh refinement procedure used within the MPC method has been successful at coupling continuum and particle simulations where the highest refinement level is required within the DSMC module. However, for some flows, the refinement level required to resolve the viscous thermal boundary level is higher than the corresponding DSMC requirements. Currently, this leads to an over refinement of the DSMC mesh in these regions. Though this does not affect the physical accuracy of the simulation, it increases the numerical cost of the DSMC module in these regions, which directly increases the numerical cost of the entire MPC simulation. Instead, if both simulation methods are allowed to use computational meshes that are completely optimized for their respective needs, the numerical cost of each simulation module will be minimized. These changes will result in slightly more complicated hybrid data structures and routines with more sophisticated averaging and particle generation algorithms since cells may not occupy the same physical space. However, results from previous work and those contained in this dissertation demonstrate that the overall numerical cost of the hybrid procedures are small compared to the cost

associated with each flow module, so the changes are expected to result in an overall reduction of numerical cost of many hybrid particle-continuum simulations.

### 7.3.4 Continuum Breakdown Parameter

Many of the different switching parameter values that are used to predict the onset of continuum breakdown, including the gradient-length Knudsen number used in the MPC method, have been found by comparison of predictions of fully continuum and kinetic simulation techniques. However, in all flows of interest for application of hybrid particle-continuum methods, the continuum regions are dependent on accurate prediction of nearby rarefied regions. Therefore, full simulations of these flows with a continuum method can shift the results in regions that are truly continuum. Results shown in Sec. 4.3.2 have demonstrated that a relaxed cutoff parameter can allow MPC simulations to maintain excellent agreement with full DSMC results. Additional study of the rarefied-continuum breakdown and switching parameter using a hybrid particle-continuum simulation technique may result in a more appropriate switching parameter that reduces the computational cost of hybrid techniques while maintaining the same level of physical accuracy.

### 7.3.5 Investigation of Rarefied Effects in Near-Equilibrium Hypersonic Flows

As first stated in Chapter I, many flows of interest only contain extremely small localized regions of flow that are in collisional nonequilibrium. Accurate simulation of these flows with full DSMC is often prohibitively expensive due to the large numerical cost associated with simulation of the highly continuum regions. However, based on the success of reproducing full DSMC simulations with the MPC method that has been demonstrated by previous work and this dissertation, the MPC method can

be used as a tool to explore the effect of these highly localized regions that exhibit collisional nonequilibrium without a large increase in the numerical complexity and cost. One example of these types of flows is a high density propulsive decelerator jet expanding in a near equilibrium flow [105]. The collision length scales within the jet can be over six orders of magnitude smaller than the length scales of the outer flow. This large variation in collision length scales coupled with a large transient time would require an enormous computational expense to study just a single flow condition with the DSMC method. Rather, the MPC method can significantly reduce the computational expense to enable a full study of various flow configurations.

## **APPENDICES**

## APPENDIX A

### Species Data

#### A.1 Variable Hard Sphere Coefficients

Table A.1 lists the coefficients used in the Variable Hard Sphere (VHS) collision models. These coefficients are used to calculate collision probabilities in Bird's No Time Counter (NTC) [10] along with the temperature viscosity relation, shown in Eq. 3.1.

Table A.1: Species data for VHS collision model

Species	$\omega$	$d_{ref}$ [m <sup>2</sup> ]	$T_{ref}$ [K]
N <sub>2</sub>	0.75	$4.17 \times 10^{-10}$	273.
O <sub>2</sub>	0.75	$4.07 \times 10^{-10}$	273.

#### A.2 Rotational Relaxation Coefficients

Table A.2 lists the coefficients used in the rotational relaxation models for each species for the rotational collision number, shown in Eq. 4.7, and derived by Parker [89].

Table A.2: Species data for rotational relaxation model

Species	$Z_s^\infty$	$T_s^* [\text{K}]$
N <sub>2</sub>	18.1	91.5
O <sub>2</sub>	14.4	90.0

### A.3 Vibrational Relaxation Coefficients

Table A.3 lists the coefficients used in the vibrational relaxation models. Equations A.1 and A.2 list the correlations proposed by Millikan and White [94] to calculate the coefficients needed for the Landau-Teller form [99] of the vibrational relaxation time that is shown in this dissertation as Eq. 5.16.

$$A_{\text{MW}} = 1.16 \times 10^{-3} \mu^{1/2} \theta_{\text{VIB}}^{4/3} \quad (\text{A.1})$$

$$B_{\text{MW}} = 0.015 \mu^{1/2} A_{\text{MW}} \quad (\text{A.2})$$

Figure A.1 shows the variation of vibrational relaxation time and average probability as a function of temperature for diatomic nitrogen using the provided constants. Park's high temperature correction has successfully increased the vibration-translation relaxation time to ensure that the average probability of a vibrationally inelastic collision remains below unity.

Table A.3: Species data for vibrational relaxation models

Species	$\theta_{\text{VIB}} [\text{K}]$	$A_{\text{MW}}$	$B_{\text{MW}}$	$\sigma_{\text{PARK}} [\text{m}^2]$
N <sub>2</sub>	3395.	221.	12.3	$5.81 \times 10^{-21}$
O <sub>2</sub>	2239.	136.	8.1	$5.81 \times 10^{-21}$

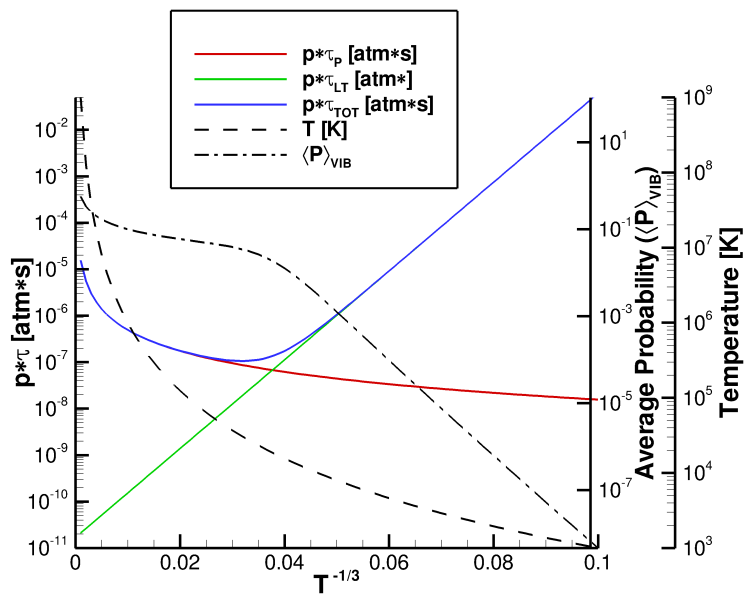


Figure A.1: Variation in vibrational relaxation time for  $\text{N}_2$

## APPENDIX B

### Estimation of a Probability Density Function

This appendix contains a detailed description of the procedure used to estimate the probability density function from data sampled in DSMC simulations. The technique used to produce probability density functions in this dissertation is an extension of the typically used histogram method that has constant bin sizes.

An estimation,  $\hat{f}$ , of the probability density function,  $f$ , using the histogram technique with constant bin widths can be found using Eq. B.1 where  $n$  is the total number of samples, and  $h$  is the bin width.

$$\hat{f}(x)dx = \frac{1}{nh} (\text{Number of } X_i \text{ in same bin as } x) dx \quad (\text{B.1})$$

However, a constant bin size must be specified across the entire range of interest of the probability density function. This poses difficulties for probability density functions that have a large range in probabilities and resolution of high probability peaks and low probability tails of the probability density function are equally important. For example, if a small bin size is selected in order to resolve the high probability peaks for the probability density function, the estimation of the tails requires a large number of samples to reduce the statistical scatter associated with the limited number of samples in this region. Conversely, if large bins are utilized in order to reduce the

statistical scatter of the low probability tails of the probability density function, the important peaks may be undersolved.

Instead, this work uses variable bin sizes using Eq. B.2 where now the width of the bin,  $h_i$  varies throughout the parameter space.

$$\hat{f}(x)dx = \frac{1}{nh_i} (\text{Number of } X_i \text{ in same bin as } x) dx \quad (\text{B.2})$$

Now a selection of the bin sizes must be specified. This is performed using an automated process through use of the sampled data that the probability density function is being estimated from. Here, the bin width size is selected such that an equal number of samples exist in each bin which is a way of maintaining nearly constant statistical scatter associated with a final sample size in each bin across the entire range of interest. The width of the  $i$ th bin is calculated using Eq. B.3 where  $X_k$  is the  $k$ th sample from the ordered data and  $N_h$  is the user specified number of samples in each bin.

$$h_i = \left( \frac{X_{i \times N_h} - X_{i \times N_h - 1}}{2} - \frac{X_{(i-1) \times N_h} - X_{(i-1) \times N_h - 1}}{2} \right) \quad (\text{B.3})$$

An example of an estimation of a sampled probability density function for rotational energy using the extended histogram technique with variable bin widths described above is shown in Fig. B.1. Each symbol is the average probability of the bin that is centered at that location in rotational energy space. The probability density function varies by over three orders of magnitude over the range of interest. Here, the bin widths successfully adaptively shrink to resolve the peak of the probability density function, and also grow to maintain a constant number of samples in the low probability tail to reduce the effect of statistical scatter associated with a finite number of samples.

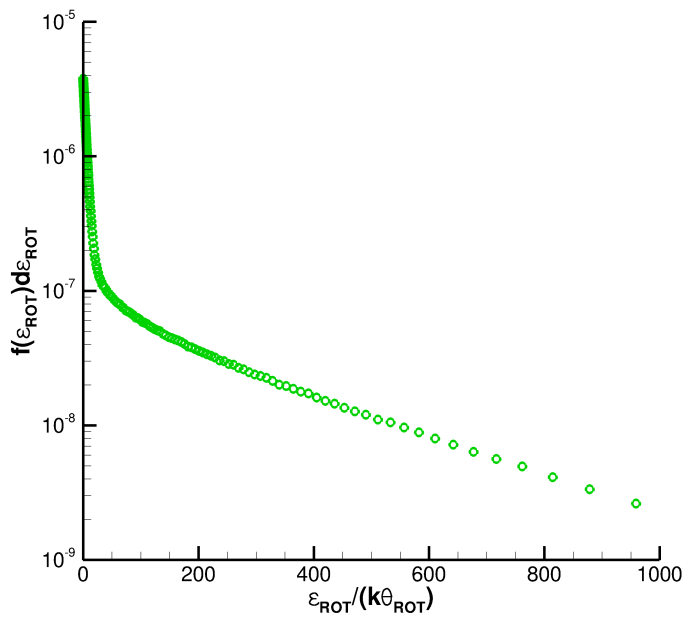


Figure B.1: Example of the variable bin width histogram technique to construct a rotational energy probability density function from data sampled in the shock interior from the DSMC method

## **BIBLIOGRAPHY**

## BIBLIOGRAPHY

- [1] Putnam, Z. R., Bairstow, S. H., Braun, R. D., and Barton, G. H., "Improving Lunar Return Entry Range Capability Using Enhanced Skip Trajectory Guidance," *Journal of Spacecraft and Rockets*, Vol. 45, No. 2, March 2008, pp. 309–315.
- [2] Wright, M. J., Prabhu, D. K., and Martinez, E. R., "Analysis of Apollo Command Module Afterbody Heating Part I: AS-202," *Journal of Thermophysics and Heat Transfer*, Vol. 20, 2006, pp. 16–30.
- [3] Holman, T. D. and Boyd, I. D., "Effects of Continuum Breakdown on the Surface Properties of a Hypersonic Sphere," *Journal of Thermophysics and Heat Transfer*, Vol. 23, No. 4, 2009, pp. 660–673.
- [4] Schwartzentruber, T. E., Scalabrin, L. C., and Boyd, I. D., "Modular implementation of a hybrid DSMC-NS algorithm for hypersonic non-equilibrium flows," *45th AIAA Aerospace Sciences Meeting and Exhibit*, AIAA 2007-613, 2007.
- [5] Schwartzentruber, T. E., Scalabrin, L. C., and Boyd, I. D., "Multiscale Particle-Continuum Simulations of Low Knudsen Number Hypersonic Flow Over a Planetary Probe," *Journal of Spacecraft and Rockets*, Vol. 45, No. 6, 2008, pp. 1196–1206.
- [6] Deschenes, T. R., Boyd, I. D., and Schwartzentruber, T. E., "Simulation of Near Continuum, Hypersonic Flow Using a Modular Particle-Continuum Method," Vol. AIAA 2009-, AIAA 2009-4308, 2009.
- [7] Cianciolo, A. M. D., Davis, J. L., Komar, D. R., Munk, M. M., Samareh, J. A., Williams-byrd, J. A., Zang, T. A., Powell, R. W., Shidner, J. D., Stanley, D. O., Wilhite, A. W., Kinney, D. J., McGuire, M. K., Arnold, J. O., Howard, A. R., Sostaric, R. R., Studak, J. W., Zumwalt, C. H., Llama, E. G., Casoliva, J., Ivanov, M. C., Clark, I., and Sengupta, A., "Entry, Descent, and Landing Systems Analysis Study: Phase 1 Report," 2010.
- [8] Clark, I. G., Hutchings, A. L., Tanner, C. L., and Braun, R. D., "Supersonic Inflatable Aerodynamic Decelerators for Use on Future Robotic Missions to Mars," *Journal of Spacecraft and Rockets*, Vol. 46, No. 2, March 2009, pp. 340–352.

- [9] Korzun, A. M., Braun, R. D., and Cruz, J. R., "Survey of Supersonic Retro-propulsion Technology for Mars Entry, Descent, and Landing," *Journal of Spacecraft and Rockets*, Vol. 46, No. 5, Sept. 2009, pp. 929–937.
- [10] Bird, G. A., *Molecular Gas Dynamics and the Direct Simulation of Gas Flows*, Clarendon Press, 1994.
- [11] Schwartzenruber, T. E., *A Modular Particle-Continuum Numerical Algorithm for Hypersonic Non-Equilibrium Flows*, Ph.d., University of Michigan, 2007.
- [12] Bhatnagar, P. L., Gross E. P., and Krook, M., "A Model for Collision Processes in Gases," *Physical Review*, Vol. 94, No. 3, 1954, pp. 511–525.
- [13] Holway, L. H., "Kinetic Theory of Shock Structure Using an Ellipsoidal Distribution Function," *Proceedings of the Fourth International Symposium on Rarefied Gas Dynamics*, AIP Conference Proceedings, 1966, pp. 193–215.
- [14] Vincenti, W. G. and Kruger Jr., C. H., *Introduction to Physical Gas Dynamics*, Krieger Publishing Company, 1965.
- [15] Wang Chang, C. S. and Uhlenbeck, G. E., "Transport Phenomena in Polyatomic Gases," Tech. Rep. CM-681, University of Michigan, July 1951.
- [16] Kogan, M. N., *Rarefied Gas Dynamics*, Plenum Press, 1969.
- [17] Hirschfelder, J. O., Curtiss, C. F., and Bird, R. B., *Molecular Theory of Gases and Liquids*, John Wiley & Sons, 1954.
- [18] Wright, M., Loomis, M., and Papadopoulos, P., "Aero thermal Analysis of the Project Fire II Afterbody Flow," *Journal of Thermophysics and Heat Transfer*, Vol. 17, No. 2, 2003, pp. 240–249.
- [19] Burnett, D., "The Distribution of Velocities in a Slightly Non-Uniform Gas," *Proc. London Math. Soc.*, Vol. 39, No. 1, 1935, pp. 385–430.
- [20] Chapman, S. and Cowling, T. G., *The Mathematical Theory of Non-Uniform Gases*, Cambridge University Press, 1970.
- [21] Guo, K. L., Liaw, G. S., and Chou, L. C., "Numerical predictions of the transitional flow over an elliptic cylinder by the Burnett equations and the DSMC method," AIAA-1999-3457, 1999.
- [22] Kolobov, V. I., Arslanbekov, R. R., and Frolova, A. A., "Boltzmann Solver with Adaptive Mesh in Velocity Space," *Proceedings of the 27th International Symposium on Rarefied Gas Dynamics*, AIP Conference Proceedings, 2010.
- [23] Agarwal, R. and Tcherimmissine, F., "Computation of Hypersonic Shock Wave Flows of Diatomic Gases and Gas Mixtures Using the Generalized Boltzmann Equation," AIAA-2010-813, 2010.

- [24] Wilson, C., Agarwal, R., and Tcherimmissine, F., "Computation of Hypersonic Flow of a Diatomic Gas in Rotational Nonequilibrium Past 3-D Blunt Bodies Using the Generalized Boltzmann Equation," AIAA-2009-3836, 2009.
- [25] Wagner, W., "A convergence proof for Bird's direct simulation Monte Carlo method for the Boltzmann equation," *Journal of Statistical Physics*, Vol. 66, No. 3, 1992, pp. 1011–1044.
- [26] Eymard, R., Gallouet, T. R., and Herbin, R., *Handbook of Numerical Analysis*, Vol. 7, chap. The Finite, Elsevier, 2000, pp. 713–1020.
- [27] Bassi, F. and Rebay, S., "A High-Order Accurate Discontinuous Finite Element Method for the Numerical Solution of the Compressible Navier-Stokes Equations," *Journal of Computational Physics*, Vol. 131, No. 2, March 1997, pp. 267–279.
- [28] Scalabrin, L. C., *Numerical Simulation of Weakly Ionized Hypersonic Flow Over Reentry Capsules*, Ph.D. thesis, University of Michigan, 2007.
- [29] Gnoffo, P. A. and White, J. A., "Computational Aerothermodynamic Simulation Issues on Unstructured Grids," AIAA 2004-2371, 2004.
- [30] Holman, T. D. and Boyd, I. D., "Numerical Investigation of the Effects of Continuum Breakdown on Hypersonic Vehicle Surface Properties," AIAA 2008-3928, 2008.
- [31] Lofthouse, A. J., Scalabrin, L. C., and Boyd, I. D., "Velocity slip and temperature jump in hypersonic aerothermodynamics," *Journal of Thermophysics and Heat Transfer*, Vol. 22, No. 1, 2008, pp. 38–49.
- [32] Kolobov, V. I., Bayyuk, S. A., Arslanbekov, R. R., Aristove, V. V., Frolova, A. A., and Zabelok, S. A., "Construction of a Unified Continuum/Kinetic Solver for Aerodynamic Problems," *Journal of Spacecraft and Rockets*, Vol. 42, No. 4, 2005, pp. 598–606.
- [33] Josyula, E., Arslanbekov, R. R., Kolobov, V. I., and Gimelshein, S. F., "Evaluation of Kinetic/Continuum Solver for Hypersonic Nozzle-Plume Flow," *Journal of Spacecraft and Rockets*, Vol. 45, No. 4, July 2008, pp. 665–676.
- [34] Burt, J. M., Josyula, E., Deschenes, T. R., and Boyd, I. D., "Evaluation of a Hybrid Boltzmann-Continuum Method for High Speed Nonequilibrium Flows," *Journal of Thermophysics and Heat Transfer*.
- [35] Le Tallec, P. and Mallinger, F., "Coupling Boltzmann and Navier-Stokes Equations by Half Fluxes," *Journal of Computational Physics*, Vol. 136, 1997, pp. 51–67.
- [36] Bartel, T. J., Sterk, T. M., Payne, J. L., and Preppernau, B., "DSMC Simulation of Nozzle Expansion Flows," *AIAA Paper 1994-2047*, 1994.

- [37] Breuer, K. S., Piekos, E. S., and Gonzales, D. A., “DSMC Simulations of Continuum Flows,” AIAA 1995-2088, 1995.
- [38] Titov, E. V., Zeifman, M. I., and Levin, D. A., “Application of the Kinetic and Continuum Techniques to the Multi-Scale Flows in MEMS Devices,” AIAA 2005-1399, 2005.
- [39] Pullin, D. I., “Direct simulation methods for compressible inviscid ideal-gas flow,” *Journal of Computational Physics*, Vol. 34, No. 2, Feb. 1980, pp. 231–244.
- [40] Macrossan, M. N., Metchnik, M. V., and Pinto, P. A., “Hypersonic flow over a wedge with a particle flux method,” *Proceedings of the 24th International Symposium on Rarefied Gas Dynamics*, 2005, pp. 650–656.
- [41] Burt, J. M. and Boyd, I. D., “A low diffusion particle method for simulating compressible inviscid flows,” *Journal of Computational Physics*, Vol. 227, No. 9, April 2008, pp. 4653–4670.
- [42] Burt, J. M. and Boyd, I. D., “Rotational and Vibrational Nonequilibrium in a Low Diffusion Particle Method for Continuum Flow Simulation,” AIAA 2009-3743, 2009.
- [43] Burt, J. M. and Boyd, I. D., “A Hybrid Particle Scheme for Simulating Multi-scale Gas Flows with Internal Energy Nonequilibrium,” AIAA 2010-820, 2010.
- [44] Burt, J. M. and Boyd, I. D., “A hybrid particle approach for continuum and rarefied flow simulation,” *Journal of Computational Physics*, Vol. 228, No. 2, Feb. 2009, pp. 460–475.
- [45] Burt, J. M. and Boyd, I. D., “All-Particle Multiscale Computation of Hypersonic Rarefied Flow for Mars Entry,” AIAA 2010-822, 2010.
- [46] Jun, E., Burt, J. M., and Boyd, I. D., “All-Particle Multiscale Computation of Hypersonic Rarefied Flow,” *International Symposium on Rarefied Gas Dynamics*, 2010.
- [47] Wijesinghe, H. S. and G., H. N., “A discussion of Hybrid Atomistic-Continuum Methods for Multiscale Hydrodynamics,” *International Journal for Multiscale Computational Engineering*, Vol. 2, 2004.
- [48] Boyd, I. D. and Deschenes, T. R., “Hybrid Particle-Continuum Numerical Methods for Aerospace Applications,” NATO RTO-EN-AVT-194, 2011.
- [49] Wadsworth, D. C. and Erwin, D. A., “One-Dimensional Hybrid Continuum/Particle Simulation Approach for Rarefied Hypersonic Flows,” AIAA 1990-1690, 1990.

- [50] Wadsworth, D. C. and Erwin, D. A., "Two-dimensional hybrid continuum/particle simulation approach for rarefied flows," 1992.
- [51] Hash, D. B. and Hassan, H. A., "Assessment of Schemes for Coupling Monte Carlo and Navier-Stokes Solution Methods," *Journal of Thermophysics and Heat Transfer*, Vol. 10, No. 2, 1996, pp. 242–249.
- [52] Hash, D. B., *A Hybrid Direct Simulation Monte Carlo / Navier-Stokes Flow Solver*, Ph.D. thesis, North Carolina State University, 1996.
- [53] Hash, D. B. and Hassan, H. A., "Two-Dimensional Coupling Issues of Hybrid DSMC/Navier-Stokes Solvers," AIAA 1997-2507, 1997.
- [54] Garcia, A. L., Bell, J. B., Crutchfield, W. Y., and Alder, B. J., "Adaptive Mesh and Algorithm Refinement Using Direct Simulation Monte Carlo," *Journal of Computational Physics*, Vol. 154, No. 1, Sept. 1999, pp. 134–155.
- [55] Wijesinghe, H. S., Hornung, R. D., Garcia, a. L., and Hadjiconstantinou, N. G., "Three-dimensional Hybrid Continuum-Atomistic Simulations For Multiscale Hydrodynamics," *Journal of Fluids Engineering*, Vol. 126, No. 5, 2004, pp. 768.
- [56] Roveda, R., B., G. D., and Varghese, P. L., "Hybrid Euler/Particle Approach for Continuum/Rarefied Flows," *Journal of Spacecraft and Rockets*, Vol. 35, No. 3, 1998, pp. 258–265.
- [57] Roveda, R., B., G. D., and Varghese, P. L., "Hybrid Euler/Direct Simulation Monte Carlo of Unsteady Slit Flow," *Journal of Spacecraft and Rockets*, Vol. 37, No. 6, 2000, pp. 753–760.
- [58] Nadiga, B. T. and Pullin, D. I., "A Method for Near-Equilibrium Discrete-Velocity Gas Flows," *Journal of Computational Physics*, Vol. 112, No. 1, 1994, pp. 162–172.
- [59] Sun, Q., "A Direct Simulation Method for Subsonic, Microscale Gas Flows," *Journal of Computational Physics*, Vol. 179, No. 2, July 2002, pp. 400–425.
- [60] Wang, W. L. and Boyd, I. D., "Hybrid DSMC-CFD Simulations of Hypersonic Flow Over Sharp and Blunted Bodies," AIAA 2003-3644, 2003.
- [61] Wang, W.-l., *A Hybrid Particle/Continuum Approach for Nonequilibrium Hypersonic Flows*, Ph.D. thesis, University of Michigan, 2004.
- [62] Wang, W.-l. and Boyd, I. D., "A New Energy Flux Model in the DSMC-IP Method for Nonequilibrium Flows," AIAA 2003-3774, 2003.
- [63] Lian, Y. Y., Wu, J. S., Cheng, G., and Koomullil, R., "Development of a parallel hybrid method for the DSMC and NS solver." 2005.

- [64] Wu, J.-S., Lian, Y.-Y., Cheng, G., Koomullil, R. P., and Tseng, K.-C., "Development and verification of a coupled DSMC-NS scheme using unstructured mesh," *Journal of Computational Physics*, Vol. 219, No. 2, Dec. 2006, pp. 579–607.
- [65] Lian, Y.-Y., Tseng, K.-C., Chen, Y.-S., Wu, M.-Z., Wu, J.-S., and Cheng, G., "An Improved Parallelized Hybrid DSMC-NS Algorithm," *AIP Conf. Proc.*, Vol. 1084, No. 1, Dec. 2008, pp. 341–346.
- [66] Schwartzenruber, T. E., Scalabrin, L. C., and Boyd, I. D., "Hybrid particle-continuum simulations of nonequilibrium hypersonic blunt-body flowfields," *Journal of Thermophysics and Heat Transfer*, Vol. 22, No. 1, 2008, pp. 29–37.
- [67] Schwartzenruber, T. E., Scalabrin, L. C., and Boyd, I. D., "A modular particle-continuum numerical method for hypersonic non-equilibrium gas flows," *Journal of Computational Physics*, Vol. 225, No. 1, July 2007, pp. 1159–1174.
- [68] Garcia, A. L. and Alder, B. J., "Generation of the Chapman-Enskog Distribution," *Journal of Computational Physics*, Vol. 140, No. 1, Feb. 1998, pp. 66–70.
- [69] Sun, Q. and Boyd, I. D., "Evaluation of Macroscopic Properties in the Direct Simulation Method," *Journal of Thermophysics and Heat Transfer*, Vol. 19, No. 3, 2005, pp. 329–335.
- [70] Schwartzenruber, T. E. and Boyd, I. D., "A hybrid particle-continuum method applied to shock waves," *Journal of Computational Physics*, Vol. 215, No. 2, July 2006, pp. 402–416.
- [71] Schwartzenruber, T. E., Scalabrin, L. C., and Boyd, I. D., "Hybrid Particle-Continuum Simulations of Hypersonic Flow over a Hollow-Cylinder-Flare Geometry," *AIAA Journal*, Vol. 46, No. 8, Aug. 2008, pp. 2086–2095.
- [72] Dietrich, S., "Scalar and Parallel Optimized Implementation of the Direct Simulation Monte Carlo Method," *Journal of Computational Physics*, Vol. 126, No. 2, July 1996, pp. 328–342.
- [73] Boyd, I. D., "Analysis of rotational nonequilibrium in standing shock waves of nitrogen," *AIAA Journal*, Vol. 28, No. 11, 1990, pp. 1997–1999.
- [74] Vijayakumar, P., Sun, Q., and Boyd, I. D., "Vibrational-translational energy exchange models for the direct simulation Monte Carlo method," *Phys. Fluids*, Vol. 11, No. 8, Aug. 1999, pp. 2117–2126.
- [75] Deschenes, T. R., Holman, T. D., Boyd, I. D., and Schwartzenruber, T. E., "Analysis of Internal Energy Transfer Within a Modular Particle-Continuum Method," AIAA 2009-1213, 2009.

- [76] Holman, T. D., *Numerical Investigation of the Effects of Continuum Breakdown on Hypersonic Vehicle Surface Properties by*, Ph.D. thesis, Univiersity of Michigan, 2010.
- [77] Maccormack, R. W. and Candler, G. V., “The solution of the Navier-Stokes equations using Gauss-Seidel line relaxation,” *Computers & Fluids*, Vol. 17, No. 1, 1989, pp. 135–150.
- [78] Scalabrin, L. C. and Boyd, I. D., “Development of an Unstructured Navier-Stokes Solver for Hypersonic Nonequilibrium Aerothermodynamics,” .
- [79] Druguet, M.-c., Candler, G. V., and Nompelis, I., “Effects of Numerics on Navier-Stokes Computations of Hypersonic Double-Cone Flows,” *AIAA Journal*, Vol. 43, No. 3, March 2005, pp. 616–623.
- [80] Boyd, I. D., Chen, G., and Candler, G. V., “Predicting failure of the continuum fluid equations in transitional hypersonic flows,” *Phys. Fluids*, Vol. 7, No. 1, Jan. 1995, pp. 210–219.
- [81] Wang, W.-L. and Boyd, I. D., “Predicting continuum breakdown in hypersonic viscous flows,” *Phys. Fluids*, Vol. 15, No. 1, Jan. 2003, pp. 91–100.
- [82] Blazek, J., *Computational Fluid Dynamics: Principles and Applications*, Elsevier, Oxford, UK, 2005.
- [83] Schwartzentruber, T. E., Scalabrin, L. C., and Boyd, I. D., “Investigation of Continuum Breakdown in Hypersonic Flows using a Hybrid Particle-Continuum Algorithm,” AIAA 2008-4108, 2008.
- [84] Deschenes, T. R., Holman, T. D., and Boyd, I. D., “Effects of Rotational Energy Relaxation in a Modular Particle-Continuum Method,” *Journal of Thermophysics and Heat Transfer*, accepted, 2011.
- [85] Gnoffo, P. A., “Planetary-Entry Gas Dynamics,” *Annual Review of Fluid Mechanics*, Vol. 31, Jan. 1999, pp. 459–494.
- [86] Candler, G. V., Barnhardt, M. D., Drayna, T. W., Nompelis, I., Peterson, D. M., and Subbareddy, P., “Unstructured Grid Approaches for Accurate Aero-heating Simulations,” *18th Annual AIAA COmputational Fluid Dynamics Conference*, No. June, AIAA 2007-3959, 2007.
- [87] Sun, Q., Boyd, I. D., and Candler, G. V., “A hybrid continuum/particle approach for modeling subsonic, rarefied gas flows,” *Journal of Computational Physics*, Vol. 194, No. 1, Feb. 2004, pp. 256–277.
- [88] Incropera, F. P., *Introduction to Molecular Structure and Thermodyanmics*, John Wiley & Sons, 1974.

- [89] Parker, J. G., "Rotational and Vibrational Relaxation in Diatomic Gases," *Physics of Fluids*, Vol. 2, No. 4, July 1959, pp. 449–462.
- [90] Lumpkin III, F. E., Haas, B. L., and Boyd, I. D., "Resolution of differences between collision number definitions in particle and continuum simulations," *Physics of Fluids A*, Vol. 3, No. 9, Sept. 1991, pp. 2282–2284.
- [91] Larsen, P. S. and Borgnakke, C., "Statistical Collision Model for Simulating Polyatomic Gas with Restricted Energy Exchange," *Soviet Powder Metallurgy and Metal Ceramics (English translation of Poroshkovaya Metallurgiya)*, 1974, pp. 9–45.
- [92] Allegre, J., Bisch D., and Lengrand, J. C., "Experimental Rarefied Heat Transfer at Hypersonic Conditions over 70-Degree Blunted Cone," *Journal of Spacecraft and Rockets*, Vol. 34, No. 6, 1997, pp. 724–728.
- [93] Boyd, I. D., "Analysis of vibrational-translational energy transfer using the direct simulation Monte Carlo method," *Phys. Fluids A*, Vol. 3, No. 7, July 1991, pp. 1785–1791.
- [94] Millikan, R. C. and White, D. R., "Systematics of Vibrational Relaxation," *The Journal of Chemical Physics*, Vol. 39, No. 12, Dec. 1963, pp. 3209–3213.
- [95] Park, C., *Nonequilibrium Hypersonic Aerothermodynamics*, John Wiley & Sons, 1990.
- [96] Gimelshein, N. E., Gimelshein, S. F., and Levin, D. A., "Vibrational Relaxation Rates in the Direct Simulation Monte Carlo Method," *Physics of Fluids*, Vol. 14, No. 12, 2002.
- [97] Farbar, E. D., "Testing of Vibrational Relaxation Model in MONACO," April 2007.
- [98] Lofthouse, A. J., Scalabrin, L. C., and Boyd, I. D., "Hypersonic aerothermodynamics analysis across nonequilibrium regimes using continuum and particle methods," AIAA 2007-3903, 2007.
- [99] Landau, L. and Teller, E., "On the Theory of Sound Dispersion," *Physikalische Zeitschrift der Sowjetunion*, Vol. 10, No. 34, 1936.
- [100] Karypis, G. and Kumar, V., "METIS: A Software Package for Partitioning Unstructured Graphs, Partitioning Meshes, and Computing Fill-Reducing Orderings of Sparse Matrices," *University of Minnesota, MN*, 1998.
- [101] Deschenes, T. R., Boyd, I. D., and Schwartzentruber, T. E., "Incorporating Vibrational Excitation in a Hybrid Particle-Continuum Method," AIAA 2008-4106, 2008.

- [102] Deschenes, T. R. and Boyd, I. D., "Parallelization of Modular Particle-Continuum Method for Hypersonic, Near Equilibrium Flows," AIAA 2010-808, 2010.
- [103] Deschenes, T. R. and Boyd, I. D., "Application of a Modular Particle-Continuum Method to Partially Rarefied, Hypersonic Flow," *International Symposium on Rarefied Gas Dynamics*, 2010.
- [104] Holman, T. D. and Boyd, I. D., "Effects of Continuum Breakdown on Hypersonic Aerothermodynamics for Reacting Flow," *Physics of Fluids*, Vol. Accepted, 2011.
- [105] Alkandry, H., Boyd, I. D., Reed, E. M., Codoni, J. R., and McDaniel, J. C., "Interactions of Single-Nozzle Sonic Propulsive Deceleration Jets on Mars Entry Aeroshells," AIAA 2010-4888, 2010.

## ABSTRACT

### EXTENSION OF A MODULAR PARTICLE-CONTINUUM METHOD FOR NONEQUILIBRIUM, HYPERSONIC FLOWS

by

Timothy R. Deschenes

Chairperson: Iain D. Boyd

As a hypersonic vehicle travels through the atmosphere, it crosses many flow regimes, from rarefied to continuum. Even in mostly continuum flow, there may be local flow features, such as shocks, boundary layers, or wakes, that display collisional nonequilibrium effects. In these regions, the molecular nature of the gas must be taken into account to accurately simulate the flow. While numerically efficient, application of continuum methods to simulate the entire flow field introduces physical inaccuracies throughout the simulation domain. Conversely, while physically accurate, simulation of the entire flow field with a kinetic method, such as the direct simulation Monte Carlo (DSMC), is computationally expensive. Instead, a hybrid method may be used that uses the DSMC method only in regions that exhibit rarefied effects, while employing the continuum description to simulate the rest of the flow field.

This dissertation extends a modular particle-continuum (MPC), hybrid method to include consistent physical models for internal energy relaxation in both flow modules. The MPC method uses a breakdown parameter to determine the interface location between flow modules, while state-based coupling procedures are used to transfer information between each module. The capabilities of the MPC method are expanded by parallelizing the method for distributed memory systems in order to decrease processor memory and wall clock time requirements. Comparison with full DSMC simulations are performed to verify each extension of the MPC method and compare computational requirements over full DSMC.

The MPC method is tested for hypersonic flow of nitrogen over various blunt body configurations and Knudsen numbers and is shown to reproduce full DSMC results with a high degree of accuracy for macroscopic flow quantities, surface properties, velocity, and energy probability density functions. Careful consideration of the changes to the evaluation of the breakdown parameter and coupling procedures due to the inclusion of internal energy relaxation models is described. Dynamic domain decomposition routines that take into account the inhomogeneous nature of the MPC method are developed and tested. The computational speedup achieved by the MPC method over full DSMC ranges from 1.67 to over 28 and varies with the reduction in number of simulation particles.